İSTANBUL TECHNICAL UNIVERSITY ★ INSTITUTE OF SCIENCE AND TECHNOLOGY

OPTICAL DESIGN AND DEVELOPMENT OF A MICROMIRROR BASED HIGH ACCURACY CONFOCAL MICROSCOPE

Ph.D. Thesis by

Karun Alper TİFTİKCİ, M.Sc.

Department : **Mechanical Engineering**

Programme : **Robotics**

March 2008

İSTANBUL TECHNICAL UNIVERSITY ★ INSTITUTE OF SCIENCE AND TECHNOLOGY

OPTICAL DESIGN AND DEVELOPMENT OF A MICROMIRROR BASED HIGH ACCURACY CONFOCAL MICROSCOPE

Ph.D. Thesis by

Karun Alper TİFTİKCİ, M.Sc.

(503942034)

Date of Submission : 14 September 2007

Date of defence examination : 24 March 2008

Supervisor : Prof. Dr. A. Talha DİNİBÜTÜN (DOU)

Members of the Examining Committee Prof. Dr. Okyay KAYNAK (BU)

Prof. Dr. Ahmet KUZUCU (İTU)

Prof. Dr. Can ÖZSOY (İTU)

Assoc. Prof. Dr. F. Önder SÖNMEZ (BU)

March 2008

İSTANBUL TEKNİK ÜNİVERSİTESİ ★ FEN BİLİMLERİ ENSTİTÜSÜ

YÜKSEK DOĞRULUKLU MİKROAYNA DİZİNLİ KONFOKAL MİKROSKOBUN OPTİK DİZAYNI VE GELİŞTİRİLMESİ

DOKTORA TEZİ

Y.Müh. Karun Alper TİFTİKCİ

(503942034)

Tezin Enstitüye Verildiği Tarih : 14 Eylül 2007

Tezin Savunulduğu Tarih : 24 Mart 2008

Tez Danışmanı : Prof. Dr. A. Talha DİNİBÜTÜN (DOÜ)

Diğer Jüri Üyeleri Prof. Dr. Okyay KAYNAK (BÜ)

Prof. Dr. Ahmet KUZUCU (İTÜ)

Prof. Dr. Can ÖZSOY (İTÜ)

Doç. Dr. F. Önder SÖNMEZ (BÜ)

Mart 2008

FOREWORD

Many people have contributed to the completion of this dissertation, both directly, by providing me with useful comments, thoughts and suggestions, as well as indirectly, by creating a stimulating and pleasant working environment. A number of people deserve special attention here, though. First of all I would like to thank Prof. Dr. A. Talha DINIBUTUN for his fascinating supervision over the whole Ph.D. period in all aspects. I would also like to express my appreciation to his management skills and character, which led to a friendly and almost stress-free working environment independent of the work load.

I would also like to thank Dr. Chris Velzel, for his daily supervision and especially for his guidance by his industry experience during Ph.D. study. For any mind boggling issue, he always had a real life example ready in mind. Especialy during the first years of this project, Klaas Struik has been contributing to this project first by supplying the application and then sparing the time to solve mechanical problems, finding creative solutions for problems, and giving ideas voluntarily. I would also like to express my gratitude to Dr. Maarten Jansen, my best friend and good scientist, for his helps in many aspects such as programming MATLAB, which is not my strongest points, for letting me use and manipulate his old codes, Dr. Suzanne Cosijns-Jansen her important advices on experimental set-up and most of all for their friendship. Charlotte Groothuis deserve many thanks. For almost a year she did a loads of work with ZEMAX software. I would also like to thank Family Pieter and Trudy Cosijns for their warmly support during my stay in Holland and accepted me as a member of their family. I would also like to express my pleasure of working in the same group with Dr. Guido Gubbels and many thanks also his lovely wife Astrid for her support during first year of my wife's in Holland. Also I would like to thank to my brother Harun Resit TIFTIKCI, although his busy work and private life who tried to help me while I was fay a away in Netherland playing a key role between Institute of Science and Technology at İ.T.Ü and me.

Especially during the last years of this study, I couldn't spare enough time to my family, which they deserve. I would like to thank them for their being patient, understanding, supporting. Last but not the least, special thanks go to my cook, composer, best friend and soul mate who are one and the same person with my beloved wife BUKET.

This thesis is dedicated to my parents, Sevim and Haydar TİFTİKCİ

March 2008 Karun Alper TİFTİKCİ

TABLE OF CONTENTS

ABBREVATIONS **v**
LIST OF TABLES **vi**
LIST OF FIGURES **vii**
LIST OF SYMBOLES **x**
SUMMARY **xii**
ÖZET **xiii**

1. INTRODUCTION **1**
1.1. Micro system technology 1
1.2. Nanotechnology 3
1.3. Technology needs measurement 4
1.4. Characterization of engineering surfaces 5
1.5. Optical methods for surface characterization 7
1.5.1. State of the art review 9
1.6. Comparison of measurement techniques 14
1.6.1. Comparison of optical measurement techniques 14
1.6.2. Comparison with mechanical stylus measuring techniques 16
1.7. Classification of measuring instruments 17
1.8. Objectives and outline of the thesis 18
1.8.1. Research objectives 19
1.8.2. Outline of the thesis 20

2. CONFOCAL SCANNING MICROSCOPY IN SURFACE CHARACTERIZATION **21**
2.1. A short history of confocal microscopy 21
2.2. Conventional microscopy versus scanning microscopy 22
2.3. Depth response of the confocal microscope 24
2.3.1. The influence of finite pinhole size 26
2.4. Influence of aberrations on the depth response 28
2.4.1. Chromatic aberrations 29
2.4.2. Spherical aberration and astigmatism 31
2.4.3. Coma 34
2.4.4. Field curvature and distortion 35
2.5. Depth resolution 35
2.6. Lateral resolution 37
2.7. Practical aspects of confocal microscopy 38
2.8. Summary 41

3. MICROMIRROR BASED CONFOCAL MICROSCOPE **42**
3.1. Toward a new type of confocal microscope 42

3.2. Analysis of the Microscan system's components 44
3.2.1. The DMD and its properties 45
3.2.2. Microscope objectives 50
3.2.3. The image detector 51
3.2.4. Results of system analysis 52
3.3. Establishment of the optical set-up 53
3.3.1. A basic approach for the optical set up 53
3.4. Ray tracing analysis 58
3.5. Tolerance budget and worst-case design 63
3.5.1. Establishing Tolerances 65
3.6. Summary 66

4. EXPERIMENTAL SET-UPS and MEASUREMENTS 67
4.1. Introduction 67
4.2. Comparison of real pinholes with DMD pixels 68
4.3. A semi-confocal microscope 71
4.4. DMD based experimental set-ups 72
4.4.1. Illumination of the DMD 77
4.5. Measurement procedure 79
4.5.1. Virtual pinhole patterns 79
4.5.2. Matching between the DMD and the CCD 81
4.5.3. Lateral scanning 84
4.5.4. Axial scanning 86
4.5.5. Surface topography determination 87
4.5.6. Software 88
4.6. Verification measurements 90
4.6.1. Measurement without lateral scanning 99
4.7. Summary 100

5. CONCLUSIONS and FUTURE WORK 101
5.1. Conclusions 101
5.2. Future work 103

REFERENCES 105

CURRICULUM VITAE 111

ABBREVATIONS

MST	:	Complementary metal-oxide-semiconductor
CMOS	:	Micro electro mechanical systems
OM	:	Opto-mechanical devices
MEOMS	:	Micro electro opto mechanical devices
DMD	:	Digital micromirror device
DLP	:	Digital light processing
SI	:	International system of units
AFM	:	Atomic force microscope
CCD	:	Charge couple device
PSD	:	Point spread function
SPM	:	Scanning phase microscope
SEM	:	Scanning electron microscope
TSROM	:	Tandem scanning optical microscope
RSOM	:	Real time scanning microscope
FWHM	:	Full width half maximum
LSA	:	Lateral spherical aberrations
TSA	:	Transverse spherical aberrations
RMS	:	Root mean square
PSF	:	Point spread function
PWM	:	Pulse width modulation
TSA	:	Transverse spherical aberrations
SVGA	:	Super video graphic adapter
XGA	:	Extra graphic adapter
SXGA	:	Super extra graphc adapter
SNR	:	Signal to noise ratio
NA	:	Numerical aperture
FOV	:	Field of view
f	:	Focal distance
MO	:	Microscope objective
SA	:	Spherical aberrations
FOV	:	Field of view

LIST OF TABLES

		Page No
Table 1.1	Comparison of optical measurement techniques.	14
Table 1.2	Developed system specifications	20
Table 2.1	Numerical values of Figure 2.5. The system is focused for green light	30
Table 2.2	Numerical values of Figure 2.8.	41
Table 3.1	DMDs specifications list	46
Table 3.2	Selection of the proper DMD type	53
Table 3.3	Selected system components and their specifications	53
Table 3.4	System specification summary	58
Table 3.5	DoF and Vertical Resolution relation table	58
Table 3.6	Microscan system lens data	59
Table 3.7	Simulation field table	60
Table 4.1	Comparison of mechanical stylus and Microscan. The results are the averages of the six repeated measurements.	96

LIST OF FIGURES

		Page No
Figure 1.1 :	Classification of Micro System Technology.	1
Figure 1.2 :	Digital Micromirror Device (DMD^{TM}) as MEMS. Each pixel has a size of $16\,\mu m \times 16\,\mu m$ and the distance between two DMD mirror is $1\,\mu m$. Mirrors can rotate $\pm 10°$ around the diagonal axis.	2
Figure 1.3 :	Taniguchi's approach, future trend in nanotechnology. Adapted from [1].	3
Figure 1.4 :	Layer of engineering surfaces	6
Figure 1.5 :	Worldwide number of patent applications in the field of optical metrology. From [2] according to Market engineering research for the total European industrial vision system market, 2000, Frost & Sullivan Report, Frost & Sullivan.	8
Figure 1.6 :	Principle of the auto-focus sensor. Adapted from [3]	9
Figure 1.7 :	Principle of the triangulation sensor. Adapted from [2]. . . .	10
Figure 1.8 :	Principle of the Fringe projection. Adapted from [3]	11
Figure 1.9 :	Principle of the Mirau interferometer	12
Figure 1.10	Principle of confocal microscopy	13
Figure 1.11	Stedman Diagram. *Amplitude-wavelength* plot of the working range of $3D$ surface measurements instruments	17
Figure 2.1 :	The idea of a conventional microscope	22
Figure 2.2 :	The idea of a *Type-I* scanning microscope	23
Figure 2.3 :	The idea of a confocal scanning microscope	24
Figure 2.4 :	The principle of confocal microscope	25
Figure 2.5 :	Zemax simulation result of the developed system for the axial chromatic aberration. Microscope objective is simulated with paraxial lens. During simulation green light is selected as main focusing wavelength	30
Figure 2.6 :	Theoretical intensity curve response of z scanning for confocal microspe for microscope objective $20\times$ with NA 0.45 and for $\lambda = 0.486133\,\mu m$ (blue) and $\lambda = 0.656273\,\mu m$ (red). Demonstration of the effect of chromatic aberration in confocal microscopy	31
Figure 2.7 :	Spherical aberration	34
Figure 2.8 :	Types confocal applications	38
Figure 2.9 :	New generation Nipkow disk based confocal microscope. Developed by Corle and Xiao [4].	40
Figure 3.1 :	Illustration of DMD based confocal system (Microscan) by comparing to with the classical confocal microscope	44
Figure 3.2 :	Image of a DMD chip and the detail of the group of DMD pixels	45
Figure 3.3 :	The idea of using a DMD unit as an optical switch	47

Figure 3.4 : The idea of the grayscale operation 48
Figure 3.5 : DMD resolution vs chip diagonal 48
Figure 3.6 : Optical efficiency of DMD based systems 49
Figure 3.7 : Basic limitations for the matching between the Microscan components 54
Figure 3.8 : 2D scheme of the developed system. 55
Figure 3.9 : Matching approach on DMD and CCD 55
Figure 3.10 2D scheme of the developed system where M.O. is used for microscope objective 57
Figure 3.11 First simulation schema 59
Figure 3.12 Selected simulation points on the DMD 60
Figure 3.13 Spot diagram on the object, the system is focusing for center DMD. 60
Figure 3.14 Spot diagram on the object, the system is focusing for outer DMD. 61
Figure 3.15 Spot diagram on the CCD, system is focusing for center DMD mirror 61
Figure 3.16 Spot diagram on the CCD, system is focusing for outer DMD mirror 62
Figure 3.17 Depth response of the developed system for the ideal objective application 63
Figure 3.18 Screen shot for Zemax tolerancing 63
Figure 3.19 Error sources in the system 65
Figure 4.1 : Comparison of pinhole vs DMD by means of intensity curves and contrast efficiency 68
Figure 4.2 : Experimental set-ups for comparison of DMD pixel with real pinhole 69
Figure 4.3 : Result of experimental comparison of pinhole vs DMD by the means of intensity curves and contrast efficiency 70
Figure 4.4 : Experimental set-up with dummy. Dummies can be realized with pinholes of different size and shapes. 72
Figure 4.5 : The very first build experimental set-up 73
Figure 4.6 : Depth response curves of the first experimental set-up 74
Figure 4.7 : 2nd set-up 75
Figure 4.8 : PSF functions 76
Figure 4.9 : Comparison of Gauss evaluation and direct measurement result. 77
Figure 4.10 Illumination principle of Microscan 78
Figure 4.11 The proper illumination optics for DMD 79
Figure 4.12 Flow chart for scanning 80
Figure 4.13 Idea of the confocal image forming 81
Figure 4.14 Real output for DMD scanning 82
Figure 4.15 Realization of the matching between the DMD and the CCD chip 83
Figure 4.16 The DMD and the CCD matching during a measurement . . . 84
Figure 4.17 Lateral scanning idea 85
Figure 4.18 Measurement principle on a tilted object 86
Figure 4.19 Measurement flow-chart 88
Figure 4.20 Measurement result of Sine standard 91

Figure 4.21 Measurement results of Sine standard 92
Figure 4.22 Measurement result of depth standard 93
Figure 4.23 Evaluation of depth measurement result 93
Figure 4.24 Measurement result of glass U groove standard 94
Figure 4.25 Cross-section of glass U groove standard 94
Figure 4.26 Measurement result of a metal V groove standard 95
Figure 4.27 Evaluation of the metal groove standard 95
Figure 4.28 Measurement on a PTB-Halle roughness standard 96
Figure 4.29 Evaluation of the roughness measurement result 97
Figure 4.30 Measurement on a Vicker's indent 97
Figure 4.31 Evaluation of the measurement on a Vicker's indent 98
Figure 4.32 Measurement result of an AFM standard 99
Figure 4.33 Evaluation of the AFM measurement data 99
Figure 4.34 Semi-confocal measurement result of depth standard 100

LIST OF SYMBOLES

$\delta \mathbf{z}$	:	z movement, axial position in length unit
$\delta \mathbf{x}$	:	z movement in length unit
$\mathbf{I}$	:	Axial intensity in arbitrary unit
$\mathbf{u}, \theta$	:	, Microscope acceptance angle
$\mathbf{FWHM_{i,d}}$	:	full width half maximum value for specular and diffuse surfaces
ω	:	Spot size at z distance
ω_0	:	Spot size at $z = 0$ distance, beam waist
λ	:	Wavelength
$\mathbf{r_i}$	:	illumination pinhole radius
$\mathbf{r_d}$	:	detection pinhole radius
$\mathbf{r_i}$	:	illumination pinhole radius
$\mathbf{zr_r}$	:	Rayleigh distance
$\mathbf{r_a}$	:	radius of airy disc
$\mathbf{S}$	:	Sthrel ratio
$\mathbf{W}$	:	wavefront error
$\mathbf{a}, \mathbf{b}$	:	Spherical aberrations coefficients
$\mathbf{x}, \mathbf{y}$	:	(Pupil) coordinates
$\mathbf{X}, \mathbf{Y}$	:	(Field) coordinates
$\mathbf{r}, \phi$	:	(Pupil)coordinates in polar system
δ, ε	:	Wavefront errors at the edge of pupil
$\mathbf{x}, \mathbf{y}$	:	pupil coordinates
$\delta \mathbf{x_{1,2}}$	:	illumination pinhole radius
$\mathbf{R}$	:	pupil radius
$\sigma \mathbf{z}$	:	RMS focus error

OPTICAL DESIGN AND DEVELOPMENT OF A MICROMIRROR BASED HIGH ACCURACY CONFOCAL MICROSCOPE

SUMMARY

The need for fast, non-contact and precise metrology systems in the micrometer and nanometer range has long been acknowledged as an important requirement in the production of the fine machined surfaces and microelectronics. Optical technologies have made a lot of progress in the last few years and some of them are now as accurate as high grade stylus profilometers. One of the non-contact system is confocal microscope.

In recent years the technique of confocal microscopy, which first described by Minski, has become a more and more powerful tool for surface characterization, in parallel with the development of computer based image processing systems. The basic principle of confocal microscopy, light emitted from point light source is imaged onto object focal plane of a microscope objective. When a specimen position in focus leads to maximum intensity at detector pinhole. The depth discriminated detector signal is limits by the pinhole size is reduced strongly when object is defocused. One of the other significant advantage of confocal microscopy against the classical light microscopy is that the lateral resolution is significantly greater. Also optical sectioning allows the determination of z coordinates in real time.

Various designs of confocal microscope are possible, this thesis describes adaptation of Digital micromirror arrays (DMD)to confocal microscopy. DMD is a planar array of $16\ \mu\text{m} \times 16\ \mu\text{m}$ mirrors that are bistable at $\pm 10°$ normal to chip. Each individual mirror acts as an "on/off" switch by either reflecting light towards the optical system or by reflecting light into light trap. DMD unit refreshed at video rate. By controlling the video signal delivered from PC, individual mirrors can be set to their "on/off" position creating any arbitrary pattern of pixels on the chip. The design of DMD allows us project of an arbitrary pixelated image onto object. The reflected image is contain noise and losses that are the function of chip geometry. Experiments show us that the losses are around 10%.

In this thesis beside the effect of the pinhole size, all optical aberrations were studied and DMD based systems optical system were developed. This items were discussed in detail in Chapter 2 and Chapter 3. Further experimental setup which is based on the optical design and simulations and capability of the developed system were further proved in Chapter 4. The obtained results were discussed in Chapter 5.

Finally the adaptation of DMD unit for confocal applications were proved. With this study a new type of confocal system built and it capabilities proved. This adaptation process leads us further DMD applications in the direction of

lithography applications where the DMD unit can be used for optical maskless applications.

YÜKSEK DOĞRULUKLU MİKROAYNA DİZİNLİ KONFOKAL MİKROSKOBUN OPTİK DİZAYNI VE GELİŞTİRİLMESİ

ÖZET

Mikroelektronik ve hassas mühendislik yüzeylerinin imalatında mikrometre ve nanometre seviyelerinde doğruluğa sahip hassas temassız ölçme cihazlarına duyulan ihtiyaç uzun zamandır bilinen ve kabul edilmiş bir gerçektir. Optik ölçme teknikleri son yıllarda önemli bir ilerleme kaydetmiş ve hassasiyetleri temaslı ölçüm cihazları kadar yüksek hale ulaştırılmıştır. Bu yeni optik ölçme tekniklerinden birisi de Konfokal mikroskopdur.

İlk defa Minsky tarafından geliştirilen konfokal mikroskop son yıllarda, bilgisayar sistemlerinin de gelişmesi ile, yüzey ölçümlerinde giderek daha önemli bir cihaz haline gelmiştir. Konfokal mikroskobun temel çalışma prensibi, nokta ışık kaynağının optik sistem sayesinde mikroskop objektifinin fokusunda yer alan objenin üzerine görüntülenmesidir. Obje tam olarak sistemin fokus mesafesinde yer aldığı zaman bu detektör üzerinde maksimum sinyalin elde edilmesine neden olur. Eğer obje fokus mesafesinin dışında ise sinyalde şiddetli bir azalma görülür. Konfokal mikroskobun klasik mikroskopiye göre bir diğer avantajı ise yatay rezülüsyon üstünlüğüdür. Düşey (z) yönünde gerçekleştirilen tarama uygulaması ile de konfokal mikroskop ile gerçek zamanlı ölçümler mümkün olabilmektedir.

Konfokal mikroskopun farklı dizaynları bulunmaktadır, bu tez çalışmasında DMD'nin (Digital Micromirror Device, Dijital mikroayna dizini) konfokal mikroskopa adaptasyonu çalışması yapılmıştır. DMD, $16\ \mu\mathrm{m} \times 16\ \mu\mathrm{m}$ boyutunda, her biri kendi çapraz ekseni üzerinde $\pm 10^\circ$ dönme kabiliyetine sahip iki boyutlu ayna dizinidir. Bu özelliği her bir aynanın gerektiğinde ışığı optik sistemin içine, gerektiğinde ise bir ışık tuzağına gönderilmesini sağlayan bir "on / off" anahtar vazifesi görebilmektedir. Herbir aynanın bilgisayar yardımı ile birbirinden bağımsız olarak programlanabilmesi yüzey tarama işlemi sırasında istenilen büyüklükte nokta kaynak ve istenilen yüzey tarama şeklinin oluşturulmasına avantaj sağlar. Yansıtılan görüntü, ayna yapısının bir fonksiyonu olan gürültü ve kayıpları da içermektedir. Deneyler bu kayıpların %10 civarında olduğunu göstermiştir.

Bu tezde, nokta deliğinin büyüklüğünün yanı sıra bütün optik sapmalar araştırılmış ve DMD esaslı optik sistem geliştirilmiştir. Bu çalışma ve sonuçları Bölüm 2 ve Bölüm 3' de detaylı olarak tartışılmıştır. Optik dizayn ve simülasyon sonuçlarına dayanan deneysel çalışma ve geliştirilen sistemin kapasitesi Bölüm 4' de ispat edilmiştir. Elde edilen sonuçlar Bölüm 5' de tartışılmıştır.

Son olarak DMD'nin konfokal mikroskop uygulamalarına adaptasyonu gerçekleştirilmiştir. Bu çalışma ile yeni bir konfokal sistem oluşturulmuş ve kapasitesi ispatlanmıştır. Gerçekleştirilen bu adaptasyon çalışması bizi masksiz baskili devre imalatı gibi yeni DMD uygulama alanlarına yönlendirmektedir.

1. INTRODUCTION

Today's industrial needs mainly determined by the miniaturization demand in the last decades. Due to the demand for miniaturization in the market, the accuracy of measuring instruments must be improved continuously. Today, products are benefiting from the new technologies, namely Micro System Technology and Nanotechnology, of miniaturizing and precision manufacturing originally developed in micro-electronics, molecular-biology and quantum optics.

1.1 Micro system technology

Micro **S**ystem **T**echnology (MST) in a classical way can be defined as the art of producing miniaturized systems. Usually, MST refers to devices that have a characteristic dimensions of less than 1 mm but more than 1 μm. MST can be applied precisely and economically to many different areas from medical instrumentation to industrial instrumentation, from consumer electronics to automotive industry [5] [6] [7] [8]. MST can mainly be classified as combination of three main areas namely Optics, Electronics and Mechanics. Figure 1.1 illustrates the interaction between these areas.

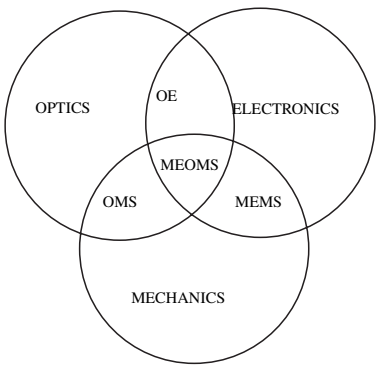

Figure 1.1: Classification of Micro System Technology.

The combination between optics and electronics is called opto-electronics (OE). The integration of diode arrays in CMOS technology and electronics (shift registers, amplifiers, etc.) on a chip can be given as good example for such a combined instrument. Micro-electro-mechanical systems (MEMS) is concerned with the production of miniature motors, fluids pumps, mechanical sensors and similar devices. Opto-mechanical devices (OM) combine mechanics and optics. The variable power objective developed by Philips can be given as an example for this combination. The acronym MEOMS (Micro-Electro-Opto-Mechanical Systems) is used for combinations of all three areas of technology and together with Micro-Electro-Mechanical-Systems (MEMS) it forms the specialized technology fields where miniaturized optics, electronics and mechanics are used. An example of a MEMS device is the Digital Micromirror Device (DMD^{TM}), which is developed by Texas Instruments for Digital Light Projection (DLP) applications and is shown in Figure 1.2.

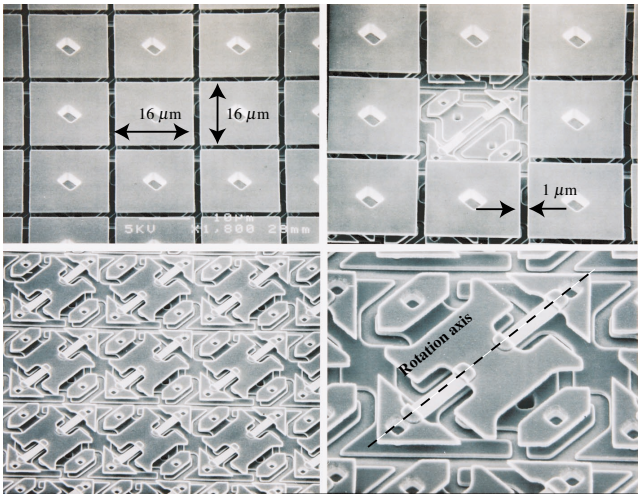

Figure 1.2: Digital Micromirror Device (DMD^{TM}) as MEMS. Each pixel has a size of 16 μm $\times$ 16 μm and the distance between two DMD mirror is 1 μm. Mirrors can rotate $\pm 10^\circ$ around the diagonal axis.

The device contains over a million tiny pixel-mirrors; each mirror has a size of 16 μm $\times$ 16 μm and is capable of rotating $\pm 10^\circ$, about a diagonal axis with. DMD's are used for projectors, high definition televisions (HDTV's), flexible illumination systems in modern cars and in digital cinemas where traditional liquid crystals technology cannot compete [9]. MEMS technology has made it

possible to decrease the distance between the mirrors to less than 1 μm. The structure of the DMD gives us chances to use this MEMS device as a MEOMS device for some application as optical switching elements. Basically, in this project the DMD is used as a rewritable pinhole array.

1.2 Nanotechnology

The word Nanotechnology was initially used to describe the target accuracy for fabrication processes involving ultra-precision surface technology. Its' basic concept was introduced by Taniguchi in 1974 [1]. In his researches Taniguchi suggested that the traced historical development of the accuracy of material processing can be used for the prediction of future trends. A modified version of his approach is given in Figure 1.3 where the time development of the accuracy of machine processing is shown together with corresponding measuring resolution [10] [11].

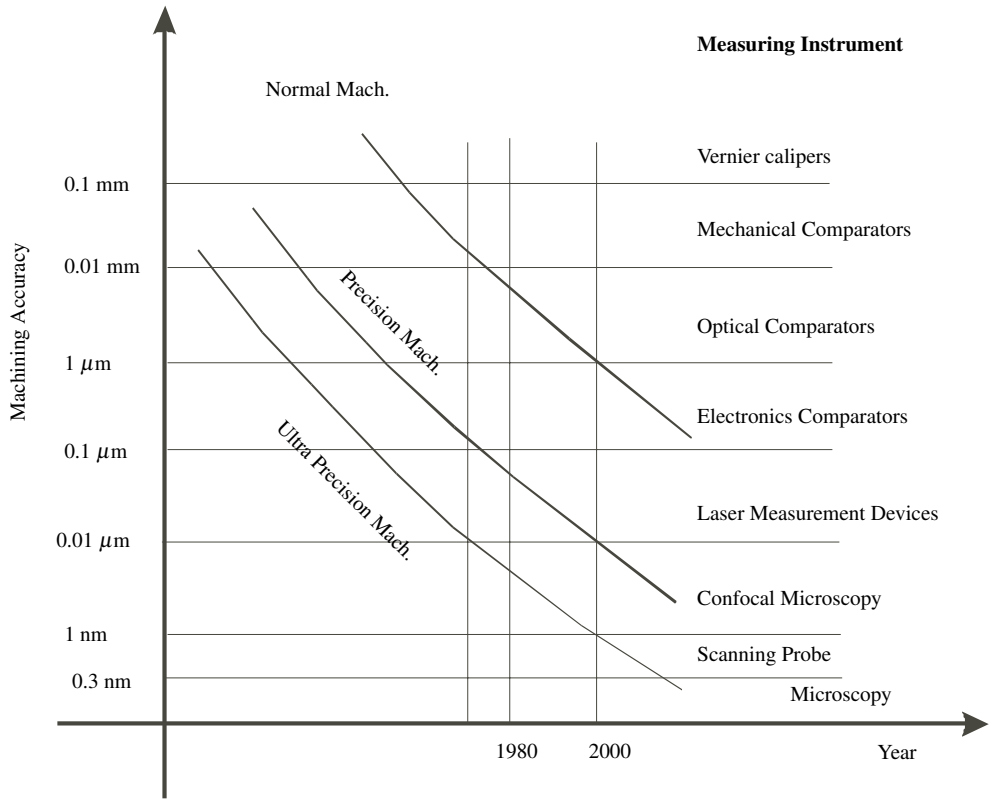

Figure 1.3: Taniguchi's approach, future trend in nanotechnology. Adapted from [1].

The continuous miniaturization in manufacturing technologies now allows us to produce nano-sized samples with nano-sized structures as well as nano-scale precision [12]. Nanotechnology products are now found in biological applications, chemistry, medical applications, microelectronics, and in precision engineering [13]. Nanotechnology is not a simple continuation of microtechnology. It marks the ultimate end of materials science, namely the dimensions where the material properties stop and molecular properties start. Nanotechnology includes not only extra-high precision processing technology but also measuring and positioning technologies with sub-nanometer resolution and scattering error. To support the current technologies it is necessary to provide devices that allow measurements of very small dimensions. These devices must measure correctly, in other word they must be traceable to the definition of the meter in the SI[1] [14].

1.3 Technology needs measurement

In the production line it is important to know whether a product meets with specified functional demands. This control process, quality control, can be done by quantitative measurements which are traceable to an agreed metrology scale. Quality control is required for all important physical quantities not only for an end product but also at various stages in the production starting from design to prototype evaluation until implementation. Therefore, metrology should be considered as a very important subject for technology, it should be developed together with science and technology. In order to apply metrology in the field of micro and nanotechnology, it is necessary to make measurements in the nanometer range traceable to the primary SI units by using:

- Proper scientific instruments
- Written standards
- Measurement standards
- Agreed measurements procedures and traceability chain.

[1] Système International des Unités / International System of Units

Not all of these requirements are fulfilled in MST or Nanotechnology; especially for surface characterization, to which this thesis is devoted, much work still has to be done. It should be remembered that technology without related metrology is incomplete.

1.4 Characterization of engineering surfaces

Due to miniaturization, the surface of products and their components has become more important. Not only the surface structures become smaller but also the surface becomes more important when the product dimensions become smaller. From 1980s' until today line-widths in microelectronic devices have decreased from 1 μm to 0.07 μm [15]. The conditions of surfaces in a production line are important for two reasons:

- the surface condition is a determinant of the functionality of the product
- it shows the conditions and efficiency of the production tool.

Thus in these conditions surfaces can be defined as "*the place where tools and materials make contact or the place where two different materials make contact*" [3]. In a more general and classical way the surface can be defined as "*a part of the solid that represents the boundaries between the solid body and its environment*" [16] [17] [18]. Surface geometry is a three-dimensional attribute and its detailed features are termed as surface topography. Simply, in engineering, topography represents the main external features of a surface. Therefore, surface topography is significant for surface performance and the importance of surface topography measurement is accepted. In production technology, surface topography is usually divided in three main groups that represent different aspects of the production process and machine tool, which is illustrated in Figure 1.4. :

- Surface form
- Surface waviness
- Surface roughness

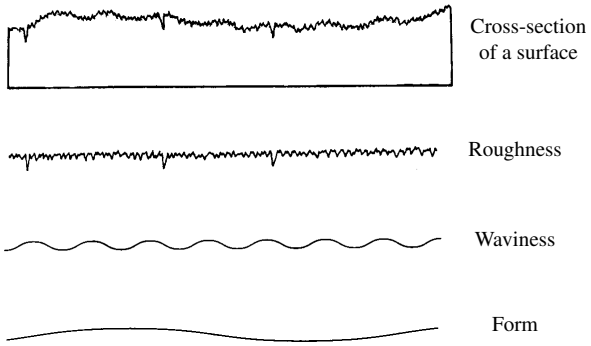

Figure 1.4: Layer of engineering surfaces

Surface form is that part of surface topography that is specified as the end result of the production process. In many cases it is the largest dimensions (or longest wavelength) that can be seen on the surface. But in microelectronics and other subfields of MST systems the specified form can contain small details. As the end result of a production process is never exactly realized, one needs metrology to obtain information about the deviations from specifications. This means that the measuring device must be able to resolve details that are much smaller than the smallest form details. Such devices do not always exist.

Surface waviness is concerned with the tracks of the production method, such as a cutting pattern in milling. Waviness can simply be defined as:
"*surface deviations that are caused by the tool used in the production process*". Usually these deviations have a quasi-periodic character; their spatial frequencies lie between 1 to 100 per mm. The orientation, which is also called lay, of the waviness is typical for the production method such as honing, milling or turning [19].

Surface roughness is basically defined as: *a random deviation which is mostly determined by the material according to manufacturing process.* Roughness consists of random surface deviations with dimensions, generally, of the order of microns in lateral directions and sub-micron dimensions in the vertical direction. Roughness depends on the material beneath the surface, it is different for crystalline, amorphous, glass or metal surfaces. Theoretically it is an avoidable parameter by selection of the proper process and material. The smoothness of

the surface can be improved by polishing, this is often applied in conventional technology such as silicon wafers and optical components, but it is not possible in Micro System Technology.

Beside these three main groups of surface topography, that are illustrated in Figure 1.4, two sub-groups, that can occur with dimensions in the range of those of waviness or form both in macro or micro level on the surface, must be added to surface characterization [3] [20].

- Surface texture
- Surface defects

Surface texture consists of two-dimensional (quasi) periodic patterns that have a specified function, for instance, to enhance the visual appearance of a surface or to influence friction. The measurement of a surface texture includes the determination of two periodicities and their orientations [20] [21].

Surface defects are incidental deviations such as scratches, digs and inclusions. For quality control applications not only the determination of surface defects but quantifying them is relatively important. For instance the size and depth of a hole on the car body in the automotive industry and the matching of bullets and fire-arms in forensic researches.

1.5 Optical methods for surface characterization

In practice surfaces are most often characterized with the aid of profilometers [22] [23] [24]. From profile measurements, surface parameters can be derived. It is well known that for the same object different parameter values are obtained from different measuring techniques and instruments. It turns out that measurement results depend on the physical principle on which the method or the instruments is based. An often used criteria to differentiate between instruments is the mechanism of interaction between instruments and sample. When this interaction consists of mechanical contact, as with a mechanical stylus system, the possibility of damage of the sample or the stylus itself can not be excluded [23] [25]. In some scanning probe systems such as AFM (Atomic Force Microscope) this

mechanical interaction is minimal. When light is used as a stylus in profilometry the interaction, reflection or absorption of light, is less likely to damage the sample surface or the probe. The use of optical methods in metrology has some advantages, in many cases better than with their mechanical counterparts [26], such as their measurement speed, accuracy and robustness. Many electro-optic devices, like CCD sensors, laser diodes, and DMD's can be used in metrological applications [27] [?]. The market acceptance and industrial interest in optical instruments for metrology can be seen from the number of patent applications. Figure 1.5 shows the number of patent applications between 1960 and 1990 and clearly indicates that there will be rapid growth for optical metrology applications in the next decades [2].

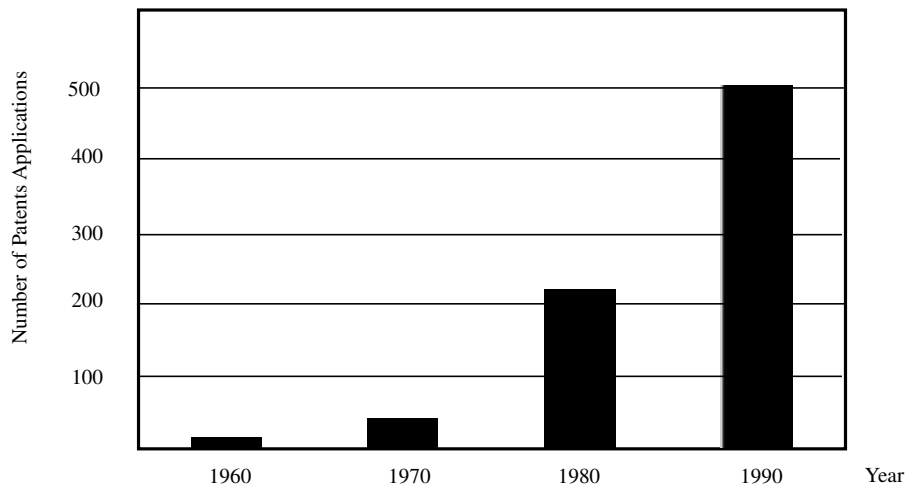

Figure 1.5: Worldwide number of patent applications in the field of optical metrology. From [2] according to Market engineering research for the total European industrial vision system market, 2000, Frost & Sullivan Report, Frost & Sullivan.

Optical instruments for surface characterization can be divided into two classes:

- Point sensors (where the output after scanning is a profile)
- Imaging sensors (where the output)

In the following the state-of-the-art instruments in optical surface characterization will be reviewed.

1.5.1 State of the art review

The instruments that are reviewed in this section are rather new but already widely used in industry [16] [24] [28]. In the context of the European research program BCR (now called SMT, Standards, Measurements and Testing) diverse studies have been done in the field of surface characterization. Further details on the techniques that are reviewed in this section can be obtained from EU Reports, 15178 EN [24], 15707 EN [29] and 16161 EN [30].

Optical stylus: This instrument is also known as auto-focus sensor. The optical stylus used to be the most common optical profiler; its principle is illustrated in Figure 1.6.

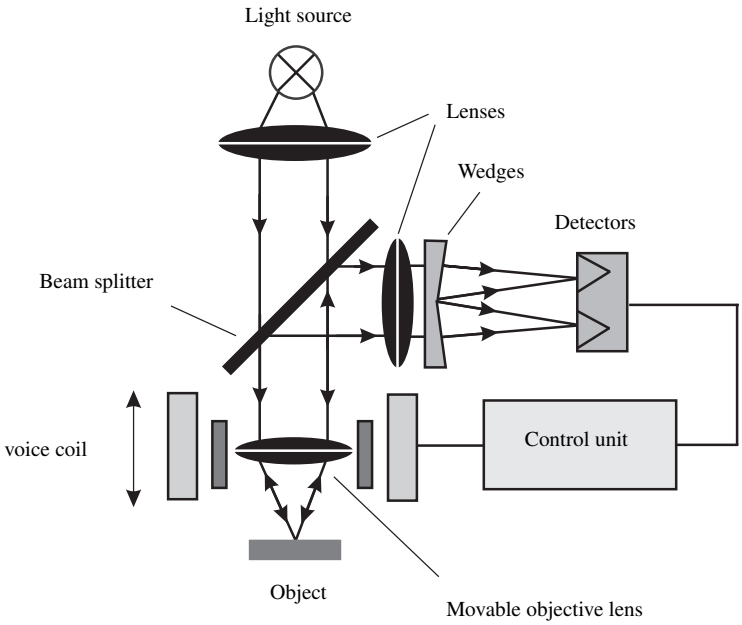

Figure 1.6: Principle of the auto-focus sensor. Adapted from [3]

A collimated beam of light is focused onto the surface of the specimen, the reflected light is directed to a focus detector that consists of a lens, two wedges and two pairs of detectors. Depending on the position of the specimen surface relative to the focal plane of the objective lens, the outer or inner segments of the detector pairs are illuminated. From the signals of the detector pairs a focus error signal, which is independent of the intensity of the beam, is obtained. The microscope objective can be moved up and down to bring the surface into

focus, the movement of the microscope objective is measured by a high resolution inductive measurement system. On a smooth specimen a resolution of 10 nm can be obtained. The specimen is mounted on a *x*-*y* translation stage to determine profiles of the surfaces. The measurement range of focus sensors is rather limited, typically 1 mm or less. This system cannot cope very well with large surface slopes; at steep edges it shows a huge overshoot. Therefore, it is not suitable for the measurement of surface roughness or the profiles of rough surfaces. Because an optical stylus needs to scan the object, its measuring speed is slow compared to imaging instruments; this is true for most point sensors.

Triangulation sensors: The triangulation sensor is a simple and reliable height measurement instrument. For this reason triangulation sensors are widely used for in-process metrology and coordinate metrology, especially in the automotive industry [31]. The main components of a triangulation sensor are a collimated light source and a detector unit which are shown in Figure 1.7.

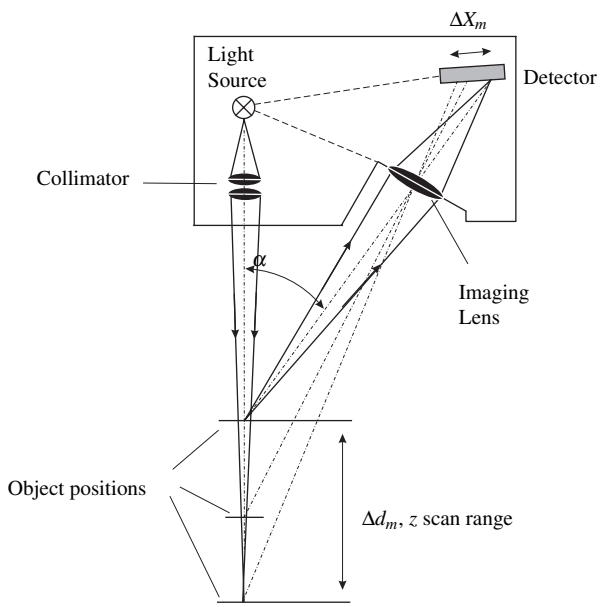

Figure 1.7: Principle of the triangulation sensor. Adapted from [2].

The optical axes of the illuminating beam and the detector unit form a fixed angle α which is called the triangulation angle. The sensitivity of a triangulation sensor depends on this angle [3] [32]. The object surface is brought close to the point where both axes intersect; the diffuse reflection of the light spot on the

workpiece surface is imaged onto the detector. The detector is preferably a point sensitive diode (PSD) [32] that measures the position of the center of gravity of the spot image. From this position the distance between sensor and specimen can be calculated. The roughness of the workpiece surface is necessary in the set-up depicted in Figure 1.7; smooth surfaces cannot be measured in this way because of insufficient diffuse reflection. Errors in the measurement may be induced by surface slopes (direct reflections), edges (shadowing), volume scattering or surface texture. Detailed studies have showed that non-cooperative surfaces can lead to large measurement errors [20] [33]. Due to the small numerical aperture of the illuminating beam, the spot size on the specimen surface is not very small, typically between $10\,\mu$m and $100\,\mu$m. This limits the lateral resolution. The vertical resolution is of the same order of magnitude [3].

Fringe projection: This method can be seen as an extension of the triangulation technique. Its principle is given in Figure 1.8.

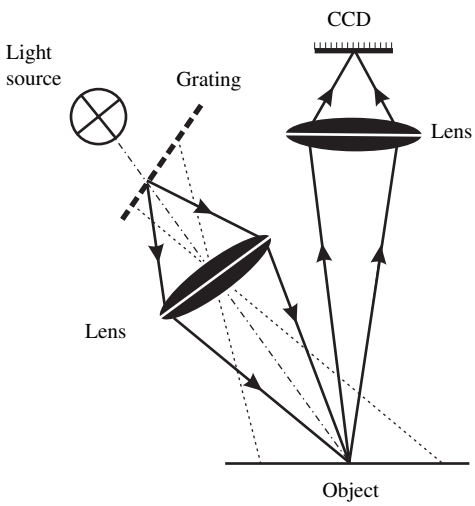

Figure 1.8: Principle of the Fringe projection. Adapted from [3]

A sinusoidal grating image is projected on the specimen surface at an angle. The lateral position of the fringes in this image can be converted into a height map of the surface. To this end the fringe pattern is imaged onto a CCD detector. The fringe pattern is shifted a few times ($n \geq 2$) over a fraction of its period; from CCD images thus gathered the height map can be computed by a simple algorithm. This procedure, called phase shifting, is used also for fringe analysis

in interferometry [34]. The height resolution of the system is determined by the number of fringes in the field and by the angle between illumination and viewing directions; for a 1 mm field size, it is usually of the order of 1 μm. The lateral resolution is determined by the number of pixels of the CCD. The most important advantage of fringe projection is that the technique can be applied to object sizes from millimeters to meters (the resolution is proportional to the object size). Like an optical stylus, fringe projectors have difficulties with steep edges and rough surfaces, resulting in creation of optical artifacts.

Interferometric surface characterization: Interferometric microscopy is widely used for the measurement of roughness and waviness, texture and defects [35]. In this technique either monochromatic or polychromatic light can be used. An application for the roughness measurement using laser illumination is reported by Velzel [30]. Step height measurement with polychromatic light using a shearing interferometer is described in [35]. A recent application of interferometry to surface characterization is the measurement of surface topography from interference contrast, using light of short coherence length. This method is also called “white light interferometry" [3]. The intensity (or Contrast), I, on a pixel depends on the distance, z, between the specimen surface and the reference plane. Figure 1.9 shows the most commonly used interferometer applied for white light interferometry.

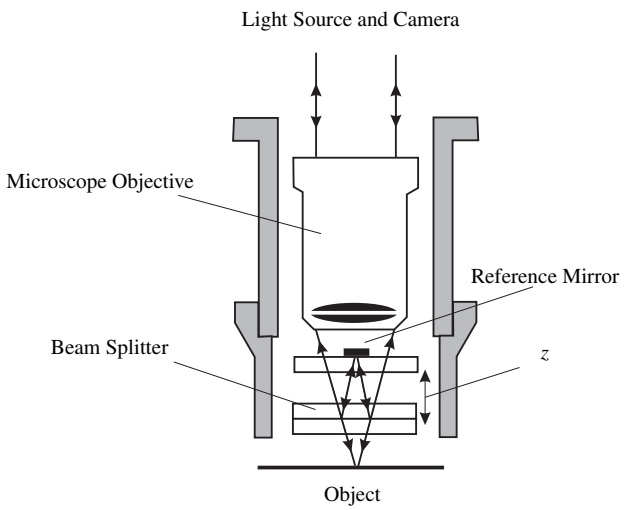

Figure 1.9: Principle of the Mirau interferometer

The reference mirror consists of a coating on an internal surface of the microscope objective; in such a way a compact construction can be realized. The vertical measurement range is determined by the free working length of the objective with interferometer; usually a few mm. To determine the surface height, the reference mirror or the complete objective are moved in the z direction. The surface height is concluded from the maximum of the contrast curve. To measure a complete surface section a series of CCD images is evaluated, giving the surface height pixel by pixel.

Confocal microscopy: In confocal microscopy a point source is focused on the object surface; the reflected light is detected by a point sensor in the image plane. Figure 1.10 illustrates the principle of confocal microscopy.

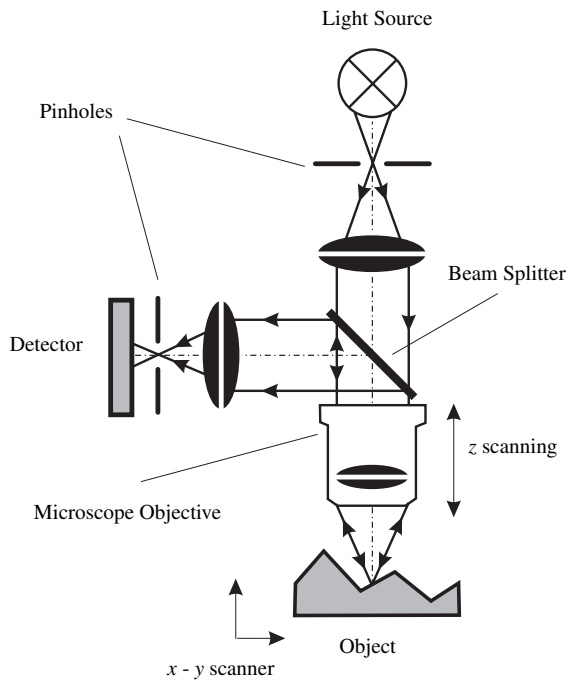

Figure 1.10: Principle of confocal microscopy

When the object surface is exactly in focus, the maximum amount of light is detected [36]. The focal plane is scanned to produce a complete image; in this image only those parts of the object that are in focus or very near to focus show up. The source and detection pinholes prevent the light emanating from regions above and below the focal plane from contributing to the observed image.

By scanning the objective in the axial direction, z, a three-dimensional image of the surface topography can be obtained.

Confocal microscopes have several advantages over conventional optical microscopes [37] [38]. Their images do not show out-of-focus blur, so that it is possible to generate three-dimensional images of transparent objects by optical sectioning [39]. Because of the spatial filter formed by the source and detector pinholes the formation of optical artifacts is prevented to some extent. This makes it an attractive technique for surface characterization because more faithful images of steep edges, grooves and rough surfaces can be obtained. Also the lateral resolution of a confocal microscope is better than that of standard light microscopes [40]. Confocal microscopy will be discussed in more detail in Chapter 2.

1.6 Comparison of measurement techniques

Surfaces can be measured in different techniques way with contact (stylus) measurements and/or without contact (optical) measurements. In this section the comparison of these techniques among themselves and also with the most commonly used technique mechanical stylus measurement will be given.

1.6.1 Comparison of optical measurement techniques

The resolution and measurement ranges, vertical as well as lateral, of the optical techniques are summarized in Table 1.1.

Table 1.1: Comparison of optical measurement techniques.

	Optical Stylus	Tri-angulation	Fringe Projection	Inter-ferometry	Confocal Microscope
δz	0.01 μm	25 μm	0.1 μm – 1 μm	0.001 μm	0.002 μm
ΔZ	1 mm	25 mm	2 μm – 200 μm	500 μm	200 μm
δx	1 μm	100 μm	1 μm – 20 μm	1 μm	0.7 μm
ΔX	n.a.	n.a.	500 μm – 10 mm	2.5 mm	1.5 mm

δz Vertical resolution
ΔZ Vertical range
δx Lateral resolution
ΔX Lateral range

In Table 1.1 the lateral measurement range for the optical stylus and laser triangulation is denoted by n.a. (not applicable). The instruments in question are point sensor applications where the lateral range is limited by the scanning mechanism and not by the principle of the sensor. This is not so for the other three techniques that are based on imaging techniques. It can be seen from Table 1.1 that laser triangulation is not usable for sub-micron measurements. Nevertheless this technique is frequently used in industry because of its simplicity and robustness.The optical stylus cannot be used with rough or structured surfaces. This prevents its application to the complete field of surface characterization. Other types of point sensors have been developed that are more useful, especially those that operate according to the confocal principle [41]. Because we discuss confocal microscopy in detail in the next chapter, we do not elaborate on this technique here.

Fringe projection, especially when combined with microscopy can result in sub-micron vertical and lateral resolution. The technique is, however, not usable for the measurement of surface roughness, because of optical artifacts and shadowing effects.

White light interferometry and confocal microscopy, can both be used for all measurements in surface characterization with the required accuracy. The lateral resolution of a confocal microscope is better by about 30% than that of a white light interferometer. The vertical resolution is of the same order for both techniques; it should be noted that the vertical resolution of interferometric microscopes is independent of the numerical aperture of their objective. On the other hand confocal microscopes are less susceptible to optical artifacts and less sensitive to steep slopes and edges. In view of technological developments the improvement of lateral resolution, if possible below the diffraction limit, remains desirable [42]. In the field of semiconductor technology near-field microscopy methods such as SPM (Scanning phase microscope) and AFM (Atomic force microscope) are widely used for testing. This technique, invented in the eighties by Pohl [43], and improved able to resolve atomic structures, where the lateral resolution goes down to nm level. This may be required for semiconductor quality assurance but because of the restricted range of measurement, $100\ \mu\text{m} \times 100\ \mu\text{m} \times$

10 μm, the application in surface characterization is limited. In addition, these techniques are expensive, time consuming, not user friendly and require trained personnel.

1.6.2 Comparison with mechanical stylus measuring techniques

Stylus instruments have the longest history of use in surface characterization. For many years such instruments have been most widely used in industry [16] [28]. Three-dimensional stylus instruments have been developed directly from 2D instruments by adding an extra translation degree-of-freedom, z, perpendicular to the horizontal x-y plane. The principle of stylus instruments is simple; the vertical movement of the tip of the stylus, which is made to follow the object surface, is amplified and digitized so that the desired surface parameters can be extracted [44] [45]. There are some drawbacks in the use of mechanical stylus instruments for measurement of surface topography. Some of them are:

- the technique is relatively slow,
- stylus can damage the surface,
- to measure 3D topography many profiles have to be obtained.

These drawbacks may be overcome by the use of optical measurement techniques. Especially imaging techniques gather the information about surface topography much faster than stylus instruments. The interaction of probe and surface is very small when light is used as a probe. The vertical resolution of optical techniques can be extended far below the classical criterion for depth-of-focus. In this way (sub)nanometer resolution can be obtained. With a conventional stylus instrument the vertical resolution is limited by mechanical vibrations and electronic noise to about 2 nm [19]. The lateral resolution of optical instruments is limited by the chosen wavelength. In stylus instruments the tip geometry determines the lateral resolution. Due to the finite tip radius, small pits and cracks in the surfaces are not detected. With some optical techniques steep slopes, edges and peaks in the surface give rise to false signals, the so-called "optical artifacts". In the early years of optical surface characterization this has hindered

the acceptation of optical techniques in industry. The introduction of imaging optical techniques has also been hindered by the circumstance that calibration standards for profile measurements are widely available whereas standards for areal measurement do not exist [17]. As a last remark, it should be stressed that optical and stylus techniques are not incompatible but complementary. Each technique has its own strengths and weaknesses.

1.7 Classification of measuring instruments

As can be seen from Table 1.1, instruments differ widely in performance, in both vertical range and resolution and in the range of surface wavelengths detectable [17]. A graphical method to describe the performance of instruments for surface characterization has been developed by Stedman [22] [46] [47]. This method is based on the limiting response of the instrument to sinusoidal surface perturbations of varying amplitude and wavelength. The limits are mapped in an amplitude-wavelength space, with logarithmic scales so that it is possible to have nanometers and meters in one diagram. Such a diagram is called a Stedman diagram in honor of its inventor. A Stedman diagram of diverse techniques is given in Figure 1.11 [19].

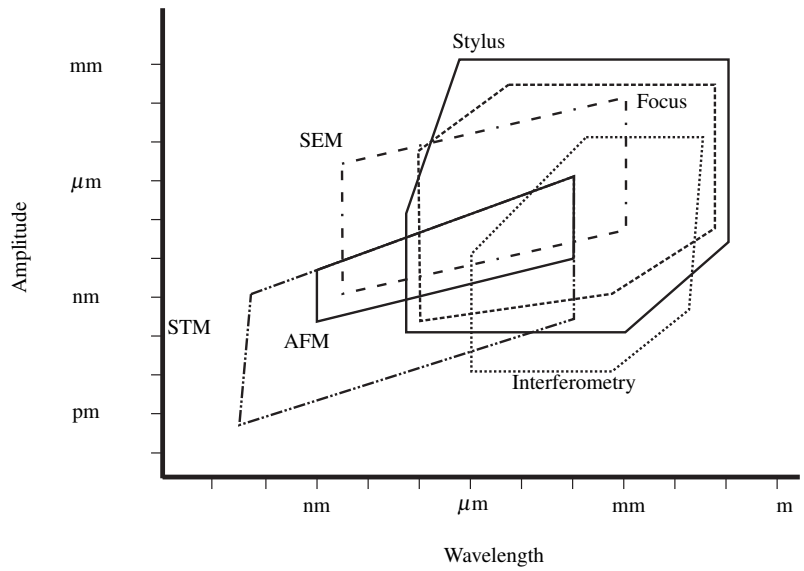

Figure 1.11: Stedman Diagram. *Amplitude-wavelength* plot of the working range of 3*D* surface measurements instruments

The horizontal contours in this diagram represent amplitude resolution and range, the vertical contours show the smallest and largest wavelength detectable. Apart from these we also see contours at angles of $arctan1$ and $arctan2$ with the wavelength axis, these contours represent limits of slope and curvature respectively [19]. The Stedman diagram gives a convenient summary of instrument performance. It allows easy and objective comparison of the fundamental capabilities and limitations of different techniques. A Stedman diagram covering all the instruments at a measurement laboratory shows its overall capability and shows which instruments can tackle a job and where there are gaps in the metrological armor.

1.8 Objectives and outline of the thesis

It is clear from the description of Micro System Technology and Nanotechnology in Sections 1.1 and 1.2 and from the conclusion that is drawn in Section 1.3, that technological developments into the nanometer range must be accompanied by innovation in metrology. It can also be concluded from the state-of-the-art review and the comparison of measurement techniques in Section 1.6 that we consider confocal microscopy as the most promising candidate for further development (with white light interferometry as a good second). Confocal microscopy is already being used in the industry for a great number of applications [48] [49]. The price of a confocal microscope is between €60.000 and €200.000, this prevents the general application of the instrument, especially in the production line.

In this dissertation a novel technique of confocal microscopy is analyzed. The key part of this technique is an innovative system itself, the Digital Micromirror Device (DMD) as an example of Micro System Technology. The DMD was already used in optical metrology for fringe projection systems [50] [31] [51]. In the developed system DMD was used as a scanning point-source device. There are two other scanning point-source devices used in confocal microscopy, the scanning laser beam and the Nipkow disc [4]. In comparison, DMD has the advantage of higher flexibility in the generation of source patterns, also it does not

contain moving macroscopic mechanical components that are sources of unwanted vibrations.

1.8.1 Research objectives

This research is a continuation of the EC Craft Project, SMT4-CT98-5525, "Development of a High Speed Optical 3D Scanner with a Micromirror Array for Illumination and Detection, MICROSCAN" where the basic principles were established and the preliminary experiments were done [52] [53]. The objectives of the Craft project were:

- Measurement time in the range of a second,
- Measurement volume ranges:
  from $10\,\mathrm{mm} \times 10\,\mathrm{mm} \times 5\,\mathrm{mm}$ to $100\,\mu\mathrm{m} \times 100\,\mu\mathrm{m} \times 10\,\mu\mathrm{m}$,
- Measuring accuracy ranging from $1\,\mu\mathrm{m}$ to $10\,\mathrm{nm}$ depending on the measurement volume,
- System price lower than €50.000.

An optical concept somewhat similar to that used during the EC Craft project was patented by GFM company at Teltow (Germany)(patent no. EP0943950A1). The goal of the extension of the project is to develop and build a stand alone 3D scanner prototype, based on the new optical measuring technique using the Digital Mirror Device (DMD). The optical concept of the developed system is based on the idea of Dr. Chris Velzel [54] and the optical lay-out is different from the patented lay-out during the EC Craft project.

In this dissertation the research is concentrated on the smaller measurement volume with the $10\,\mathrm{nm}$ resolution target. It did not look realistic to aim at short measurement times, because with the given control electronics of the DMD this is the matter of smart software; we concentrated on the optical and mechanical aspects of the the developed system. The system price will eventually be determined by the market, a system cost of €40.000 is realizable but cost reduction was not one of the focused target. Table 1.2 shows the summary of the project target and the selected components: The prototype that we

Table 1.2: Developed system specifications

Measurement Volume	10 mm × 10 mm × 5 mm	10 μm × 10 μm × 5 μm
Targeted Accuracy	1 μm	10 nm
CCD[2]	number of pixels	pixel size
Sony XC − 8500 CE	782 h × 582 v	8.3 μm × 8.3 μm
DMD[3]	848 h × 600 v	16 μm × 16 μm

developed was based on standard catalog parts, intended for testing the concept and validating the system.

1.8.2 Outline of the thesis

Besides this Chapter as an Introduction, this thesis contains the following:

Chapter 2, Confocal scanning microscopy in surface characterization starts with the technical background of confocal microscopy and explains it's use in surfaced characterization. Depth discrimination, lateral resolution and the influence of aberrations are discussed and a new model for the depth response curve is introduced and finally, a short review of existing systems is given.

Chapter 3, Micromirror based confocal microscope Starts with the explanation of the components of Microscan. Discusses a confocal microscope based on micromirrors. Shows the basic optical design and presents the result of optical simulations of its imaging properties, tolerance calculations and worst case design.

Chapter 4, Explains the experimental set-up which the measurements were done. Describes the measurement procedure and the corresponding software and finally presents the result of validating measurements.

Chapter 5, Summarizes the study and presents conclusions and recommendations.

[2]Act as a virtual detection pinhole
[3]Act as a virtual illumination pinhole

2. CONFOCAL SCANNING MICROSCOPY IN SURFACE CHARACTERIZATION

2.1 A short history of confocal microscopy

The ideas that led to the invention of confocal microscopy were formed in the early 1950's. The first development was done by Young and Roberts [55] who built a scanning microscope. An early and essential contribution to scanning microscopy was done by Minsky [56]; a few years later he invented and patented the confocal microscope [37] [57]. His problem with the proper illumination was partly solved by the development of the gas laser, and the first working confocal scanning microscope using laser illumination was built by Davidovits and Edgerin [58]. Recent developments were done by Wilson and Sheppared [59] who were inspired by the studies of Lemons and Quate on scanning acoustic microscopy [60]. Parallel to these developments an other type of confocal scanning microscope was invented by Petran and Hadravsky in the late 1960's [61]. They used a Nipkow disk, invented already in mechanical scanning television, to fulfill the requirements of point illumination and point detection. They called their invention *a tandem-scanning reflected light microscope* (TSROM). In the late 1980's this design was improved by Xiao, Corle and Kino and they called their system *a real time scanning optical microscope* (RSOM) [62] [63]. As a result of these developments, confocal microscopy has become available as a new technique for surface characterization, which exhibits several advantages over conventional optical microscopy. In the following a comparison between these two branches of microscopy is given.

2.2 Conventional microscopy versus scanning microscopy

For this comparison a simplified model of image formation can be used. From this model the performance of scanning microscopy and scanning confocal microscopy, which gives an improved image of structured surfaces, can easily be inferred. Early studies on this subject were done by Wilson and Sheppard [59] [64] and by Corle and Kino [4]. Figure 2.1(a) shows a simplified scheme of image forming in a conventional (bright field) microscope

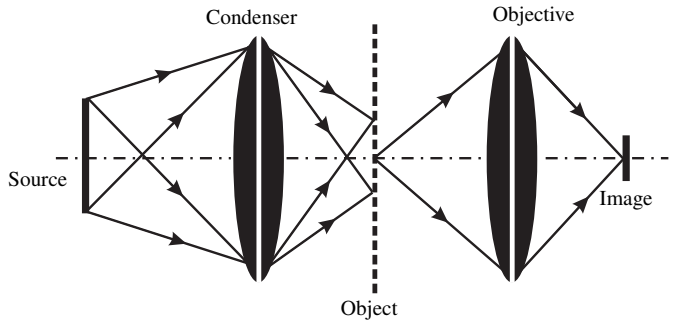

(a) Scheme of a classical microscope

(b) Conventional microscope image of a Vickers indent

Figure 2.1: The idea of a conventional microscope

This scheme shows a microscope with critical illumination (Kohler illumination); a large source is focused by a condenser onto a specimen in such a way that the interesting part of the specimen is illuminated by a patch of light, corresponding to the full field of the objective. Information from each illuminated point in the specimen is simultaneously transmitted in parallel by the objective lens to form an image. The important property of this system is that the objective is primarily responsible for image formation and determines its lateral resolution, whereas the condenser plays only a secondary role in this respect. When an image of an object with surface deviations larger than the depth of focus is captured, a blurred image is obtained. Such an image, made by a bright field microscope, is shown in Figure 2.1(b). The object was a metal surface with a microindent of a Vickers hardness probe, with a depth of approximately 12 μm. It is clear that

the 3D form of such a structure cannot be found from such a blurred picture. A scanning microscope can be realized departing from the scheme of Figure 2.1 whether by scanning a point source over the source plane or by scanning a point detector over the image plane, thereby building up a picture of the object point by point. This type of microscope was called by Wilson and Sheppard a *Type-I* scanning microscope [59], a schematic illustration is given in Figure 2.2 for the case of image plane scanning (detectors moves in image plane).

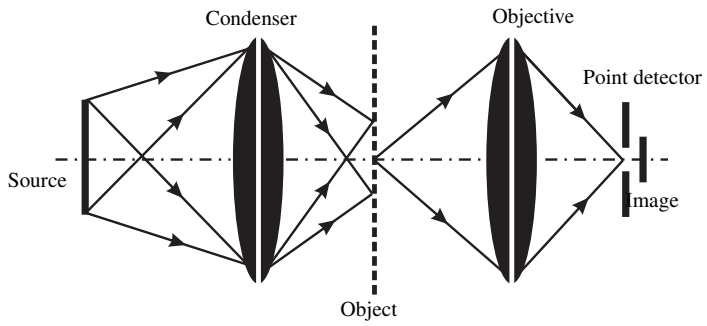

Figure 2.2: The idea of a *Type-I* scanning microscope

When the object is focused in such a way that the objective lens makes a diffraction limited image of a point object, the point detector sees only this part of the object and its immediate surroundings. This leads to a considerable reduction of flare due to light scattering in the optics of the microscope. This advantage is also valid for Type-I scanning microscopes where a cathode-ray tube is used as a scanning source [55]. The contrast can be further improved by using a point source and a point detector at the same time. This arrangement has been termed a *Type-II* or *confocal scanning microscope* [59]. A scheme of confocal microscope is given in Figure 2.3.

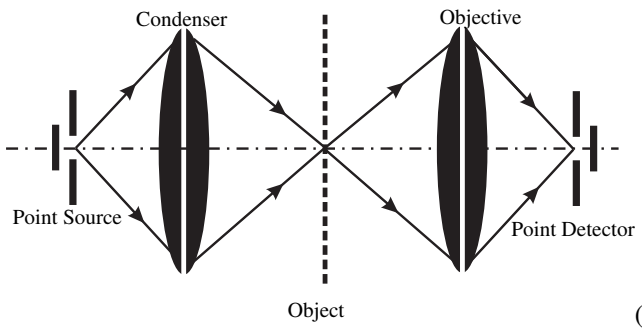

(a) Scheme of a confocal microscope

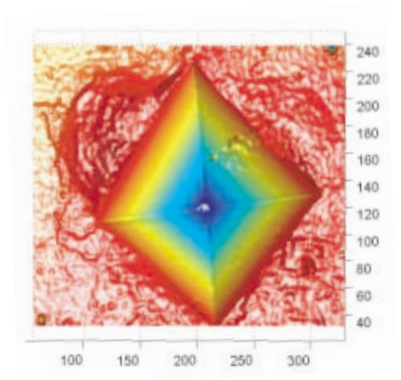

(b) Microscan image of a Vicker indent

Figure 2.3: The idea of a confocal scanning microscope

In this configuration both condenser and objective play an equal role in forming the image, leading to a sharper image with a better contrast than the image in conventional microscopy, see Figure 2.1. Moreover this scheme allows the possibility of optical sectioning [39]. The application of confocal scanning microscopy to surface characterization has been worked out by Jordan [36] and Velzel [30]. Figure 2.3(b) shows a false color coded three-dimensional image of a Vickers indent, such as is used for the measurement of micro-hardness. Comparing this to Figure 2.1(b) it can be concluded that a whole new dimension is opened for metrology by confocal microscopy.

2.3 Depth response of the confocal microscope

Detailed studies about the theory of confocal microscopy based on scalar wave diffraction and vector diffraction were done respectively by Wilson, Sheppard and Corle [59] [65]. In this section these theories will not be reproduced but the results of the scalar theory with respect to depth discrimination will be given. These results are based on the work of Lommel as reported by Born and Wolf [66]. Figure 2.4 illustrates a reflection mode confocal microscope based on scalar theory. The axial intensity, I, caused by a point source (the illumination pinhole) on axis, as a function of defocusing z, is given by,

$$I(z) = I_0 \left(\frac{\sin \frac{u}{4}}{\frac{u}{4}} \right)^2 , \qquad u = \frac{2\pi z}{\lambda} \cdot \sin^2 \theta \tag{2.1}$$

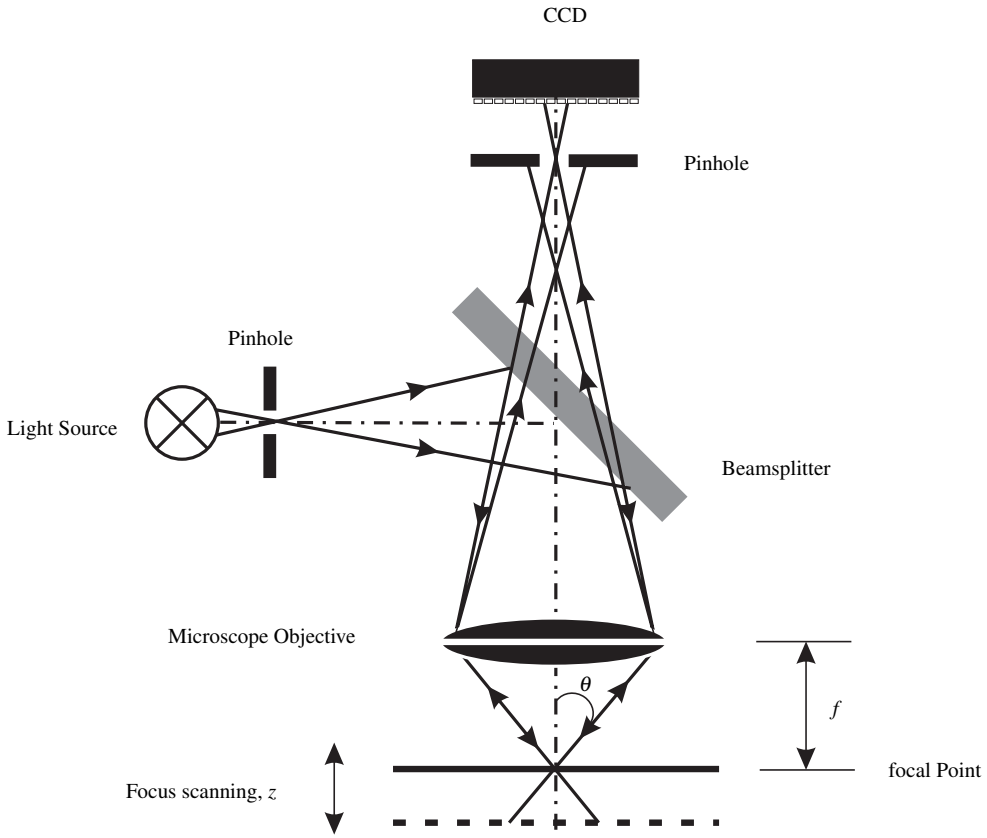

Figure 2.4: The principle of confocal microscope

where $\sin\theta$ is the numerical aperture of the microscope objective and λ is the wavelength of the light source. With a specularly reflecting object, as it is taken in the thesis of Corle [4], the double value of the defocusing must be taken, the depth response, defined as the normalized axial intensity now becomes,

$$i_s(z) = \left(\frac{\sin \frac{u'}{4}}{\frac{u'}{4}} \right)^2, \qquad u' = \frac{4\pi z}{\lambda} \cdot \sin^2\theta \tag{2.2}$$

The FWHM of $i_s(z)$ is given by,

$$FWHM_s = \frac{0.87\lambda}{\sin^2\theta} \tag{2.3}$$

The depth response given in Equation 2.2 is obtained when the illumination and detection pinholes are small compared to the Airy resolution. The effects of pinhole diameter will be considered in the next section.

For a diffusely reflecting object the depth response is not given by Equation 2.2. It is obtained from the following argument: a scatterer at a position z on the axis is illuminated by an intensity as given by Equation 2.1, the defocusing leads to the reduction of the axial intensity on the detection pinhole by another factor $I(z)/I_0$, so that the depth response for the case of diffuse reflection becomes

$$i_d(z) = \left(\frac{\sin \frac{u}{4}}{\frac{u}{4}} \right)^4, \qquad u = \frac{2\pi z}{\lambda} \cdot \sin^2 \theta \tag{2.4}$$

Equation 2.4 is also valid for pinholes which are small compared to the Airy diameter. The FWHM now takes the value

$$FWHM_d = \frac{4}{\pi} \cdot \frac{\lambda}{\sin^2 \theta} \tag{2.5}$$

2.3.1 The influence of finite pinhole size

in the previous section we deduced depth response functions for specular and diffuse objects under the assumption that the illumination and detection pinholes are small compared to the Airy radius. In practice this is not always the case and the effect of the size of pinhole diameters on the depth response must be investigated. In the following an approximate theory based on Gaussian beam propagation [67] will be presented. When the illumination pinhole is not very small, the spatial coherence of the illumination becomes an important factor in determining the depth response.

First it is focused on specular objects. With an illumination pinhole radius smaller than the coherence length we consider the pinhole a the waist of a Gaussian beam with radius w_0. Similar to previous section all dimensions are translated to the object space. Therefore ω_0 is the radius of the pinhole image in the focal plane. With a Gaussian beam the beam diameter as a function of the axial position z is given by Hecht [67].

$$\omega^2(z) = \omega_0^2 \left(1 + \left(\frac{z}{z_r} \right)^2 \right), \qquad z_r = \frac{\pi \omega_0^2}{\lambda} \tag{2.6}$$

The depth response for a small detection pinhole is given by;

$$i_s = \frac{\omega_0^2}{\omega^2(2z)} \tag{2.7}$$

From Equations 2.6 and 2.7 follows that the $FWHM$ of the depth response is given by;

$$FWHM_s = z_r \tag{2.8}$$

We conclude that as long as the illumination pinhole is coherently illuminated, the width of the depth response is proportional to the square of its radius. With a very small illumination pinhole we can take ω_0 equal to the Airy radius. In this case the entrance pupil of the objective is a approximately uniformly filled with;

$$\omega_0 = 0.61\frac{\lambda}{\sin\theta} \tag{2.9}$$

we obtain;

$$z_r = 1.13\frac{\lambda}{\sin^2\theta} \tag{2.10}$$

This is an approximate value, because the beam in object space is not Gaussian.

When the radius of the illumination pinhole is large compared to coherence radius the illumination is partially coherent. An approximate value of the beam radius is now given by;

$$\omega^2(z) = r_i^2 + \omega_0^2\left(1 + \left(\frac{z}{z_r}\right)^2\right), \qquad z_r = \frac{\pi\omega_0^2}{\lambda} \tag{2.11}$$

where r_i is the pinhole radius and ω_0 the coherence length. Using this result in Equation 2.7 the $FWHM$ is found as;

$$FWHM = z_r\sqrt{\frac{r_i^2 + \omega_0^2}{\omega_0^2}} \tag{2.12}$$

We now consider values of the detection pinhole radius. With a specular object the beam width in the detection plane is $\omega^2(2z)$, where ω^2 is given by Equation 2.6 or Equation 2.11 depending on the coherence radius. In real confocal systems the radius r_d^2 of the detection pinhole is smaller than $r_i^2 + \omega_0^2$; a larger value would lead to unwanted broadening of the depth response function. The depth response is now given by;

$$i_s = \frac{1 - e^{\frac{-r_d^2}{\omega^2(2z)}}}{1 - e^{\frac{-r_d^2}{\omega^2(0)}}} \tag{2.13}$$

With $r_d = \omega(0)$ and $\omega^2(2z) = 2\omega^2(0)$ we obtain $i_s = 0.622$ The $FWHM$ is found when $\omega^2(2z) = 2.57\omega^2(0)$ to be;

$$FWHM_s = 1.25 z_r \sqrt{\frac{r_i^2 + \omega_0^2}{\omega_0^2}} \tag{2.14}$$

It is concluded that even at limit condition, a detection pinhole with radius $r_d = \sqrt{r_i^2 + \omega_0^2}$ has only a small broadening effect. With a diffusely reflecting object we consider only the case that the illumination pinhole is coherently illuminated and that the detection pinhole has a small radius. The broadening effects of incoherent illumination and finite detection pinhole radius are equal to those obtained with a specular object. Assuming a Gaussian illuminating beam with beam waist radius ω_0, the spot radius on the defocused object is given by Equation 2.6. This spot is imaged in the detection plane. When we assume that it consist of incoherent point sources the radius of the resulting image is given by;

$$\omega^2(z) = \omega_0^2 \left(1 + \left(\frac{z}{z_r}\right)^2\right) + r_a^2 (1 + \frac{z}{z_a}) \tag{2.15}$$

where r_a is the radius of the Airy diffraction spot and z_a is the Rayleigh depth of focus,

$$r_a = \frac{\lambda}{2\sin\theta}, \qquad , z_a = \frac{\lambda}{2\sin^2\theta} \tag{2.16}$$

Taking $i_d = \omega^2(0)/\omega^2(z)$ we have a $FWHM$ equal to;

$$FWHM_d = z_a z_r \sqrt{\frac{\omega_0^2 + r_a^2}{\omega_0^2 z_a^2 + r_a^2 z_r^2}} \tag{2.17}$$

with $\omega_0^2 = r_a^2$, $z_r^2 = z_a^2$ we obtain $FWHM_d = z_a$ the same as in Equation 2.8. With $\omega_0^2 = 4r_a^2$, $z_r^2 = 16 z_a^2$ we obtain $FWHM_d = 2z_a$. We conclude that with a diffusely reflecting object the broadening depends approximately linearly on the radius of the illumination pinhole.

2.4 Influence of aberrations on the depth response

This section focuses on the influence of some basic aberrations of (symmetric) optical systems on the depth response. The following aberrations are discussed:

1. Chromatic aberrations (in the paraxial domain)

2. Monochromatic aberrations

The latter are divided into two subgroups:

(a) Aberrations that decrease the image contrast; this heading considers

- Spherical aberration
- Coma
- Astigmatism

(b) Aberrations that deform the image; the items in question are

- Field curvature
- Distortion

These aberrations are described in the literature [66] [67] [68].

2.4.1 Chromatic aberrations

In the paraxial domain two chromatic aberrations can be distinguished:

- Longitudinal chromatic aberrations (Chromatic focus error)
- Transverse chromatic aberrations (Chromatic magnification error)

Both are caused by the dispersion of optical glasses that gives rise to a dependency of lens powers from the wavelength of the radiation used [67]. With the lenses that is used in the project it has been tried to make this effect as small as possible by achromatization. This means that by the use of different types of optical glass the lens powers are made equal for wavelengths in the red and the blue. The remaining deviations of power with wavelength form the *secondary spectrum*. The secondary spectrum of the set-up, that uses standard achromats, is shown in Figure 2.5.

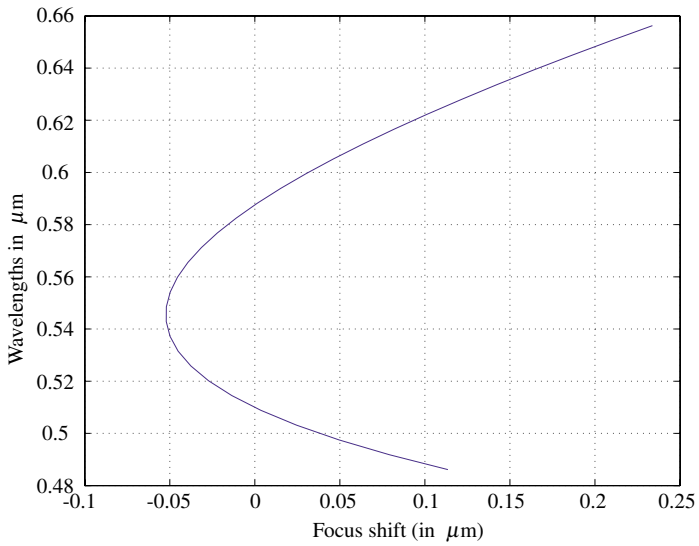

Figure 2.5: Zemax simulation result of the developed system for the axial chromatic aberration. Microscope objective is simulated with paraxial lens. During simulation green light is selected as main focusing wavelength

In this figure the microscope objective is accepted as an ideal lens and the aberrations of the microscope objective are neglected. From the numbers given in Table 2.1 it is concluded that the chromatic focus error gives rise to a slight broadening of the depth response curve and also to a possible shift of its maximum by a few tenths of a μm.

Table 2.1: Numerical values of Figure 2.5. The system is focused for green light

Wavelength in μm	Color	Focus Shift in μm
0.486	Blue	0.113
0.587	Green	0.0
0.656	Red	0.233

Both effects are relatively small compared to the FWHM of the curve (about 1.5 μm). The shift of the maximum gives rise to a systematic error of height measurement and this error can be removed by calibration. The chromatic magnification error depends on the position of the pupil in the optical system. In Section 3.3, where the optical design will be discussed, it will be shown that this position was chosen in such a way that this error is insignificant. It is also necessary to mention here another effect connected with the source spectrum.

From the theory given in Section 2.3 that the FWHM of the depth response curve depends linearly on the wavelength. This effect is shown in Figure 2.6 where the focal shifts (for the wavelengths chosen these are about equal) is neglected.

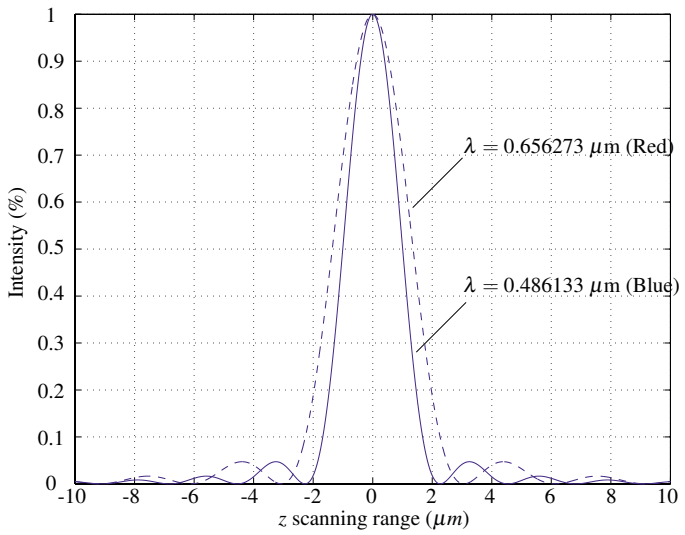

Figure 2.6: Theoretical intensity curve response of z scanning for confocal microspe for microscope objective 20× with NA 0.45 and for $\lambda = 0.486133\ \mu$m (blue) and $\lambda = 0.656273\ \mu$m (red). Demonstration of the effect of chromatic aberration in confocal microscopy

Finally, it can be concluded that the effects of the source spectrum are small and can be neglected, as long as the source spectrum is constant in time. This means that in practice one must take into account the thermal time constant of the sources used (halogen incandescent lamps or Xe high pressure gas discharges).

2.4.2 Spherical aberration and astigmatism

These aberrations are considered together, because the wavefront errors connected with them are even with respect to the meridional pupil coordinate. This is also true for the wavefront error connected with defocusing. Therefore these two aberrations will be discussed together with defocusing. Coma has an uneven wavefront deviation with respect to the meridional pupil coordinate. Therefore it will be discussed separately. The method that will be used to treat the first group of monochromatic aberrations is to calculate Strehl's number, defined as the normalized intensity in the maximum of the point spread function [66]. When

the aberrations are small, it can be shown that Strehl's number S is given to a good approximation by

$$S = 1 - \left(\frac{2\pi}{\lambda}\right)^2 Var(W) \tag{2.18}$$

The curve $S(z)$, Strehl's number as a function of defocusing, describes the central part of the depth response curve for the case of specularly reflecting objects. When spherical aberration and astigmatism are present the wavefront error (deviation of the wavefront from the reference sphere) can be written as;

$$W(x,y) = a \cdot r^2 + b \cdot r^4 + c \cdot r^2 \cdot \sin^2 \varphi \tag{2.19}$$

where x, y are pupil coordinates and r,φ are polar coordinates in the pupil, so that

$$x = r \cdot \cos \varphi \quad , \quad y = r \cdot \sin \varphi \tag{2.20}$$

The coefficient a is the coefficient of defocusing. It is connected to the defocusing distance z by the approximate relation

$$a = \frac{z}{f^2} \tag{2.21}$$

where f is the focal length of the objective in Figure 2.4.

The coefficient b in Equation 2.19 is the coefficient of spherical aberration. The radius of the blur circle connected with spherical aberrations is given by;

$$\rho_s = 4 \cdot b \cdot r^3 \cdot f \tag{2.22}$$

The coefficient c in Equation 2.19 is the coefficient of astigmatism. It depends quadratically on the field coordinate Y. The length of the focal line connected with this aberration is given by

$$\eta_a = 2 \cdot c \cdot r \cdot f \tag{2.23}$$

The variance of W is defined by;

$$Var(W) = \overline{W^2} - \left(\overline{W}\right)^2 \tag{2.24}$$

where a bar denotes an average over the pupil domain

$$0 < r < R \quad , \quad 0 < \varphi < 2\pi \tag{2.25}$$

With Equation 2.19 for W:

$$Var(W) = \frac{1}{12} \cdot a^2 \cdot R^4 + \frac{4}{45} \cdot b^2 \cdot R^8 + \frac{1}{8} \cdot c^2 \cdot R^4 + \frac{1}{6} \cdot a \cdot b \cdot R^6 + \frac{1}{12} \cdot a \cdot c \cdot R^4 + \frac{1}{12} \cdot b \cdot c \cdot R^6 \tag{2.26}$$

With Equation 2.21 and taking $R/f = sin\theta$ the FWHM of the depth response curve is, in this approximation, given by

$$FWHM_{STREHL} = \frac{\sqrt{6}\lambda}{\pi sin^2\theta} \cong \frac{0.77\lambda}{sin^2\theta} \tag{2.27}$$

when aberrations are zero. Comparing this to Equation 2.3 it can be concluded that the approximation is a fair one. With Equations 2.19 and 2.26 Strehl's number can be rewritten as a function of z:

$$S(z) = 1 - (2\pi)^2 \left(\frac{1}{12} \left(\frac{z}{z_R} \right)^2 + \left(\frac{1}{6}\beta + \frac{1}{12}\gamma \right) \frac{z}{z_r} + \frac{4}{45}\beta + \frac{1}{12}\beta\gamma + \frac{1}{16}\gamma^2 \right) \tag{2.28}$$

where the constants z_R, β, γ are defined as follows; $z_R = \frac{\lambda}{\sin^2\theta}$, $\beta = \frac{b \cdot R^4}{\lambda}$, $\gamma = \frac{c \cdot R^2}{\lambda}$. The distance z_R is the depth of focus of the objective according to Rayleigh's criterion. The constants β and γ are the spherical aberration and astigmatism at the edge of the pupil, in wavelengths. It can be seen that $S(z)$ is a parabolic curve, its maximum is found for

$$\frac{\widehat{z}}{z_R} = -\left(\beta + \frac{1}{2}\gamma \right) \tag{2.29}$$

The maximum value of $S(z)$ is given by;

$$S(\widehat{z}) = 1 - (2\pi)^2 \cdot \left(\frac{1}{180} \cdot \beta^2 + \frac{1}{24} \cdot \gamma^2 \right) \tag{2.30}$$

The FWHM for this case is;

$$FWHM_{STREHL} = \sqrt{\frac{6}{\pi^2} - \frac{2}{15} \cdot \beta^2} \cdot \frac{\lambda}{\sin^2\theta} \tag{2.31}$$

The result of Equation 2.29 is not unexpected. It is known from the geometrical theory of aberrations from Hecht [67] that the best focus in the presence of spherical aberration is found when the wavefront errors due to defocusing and spherical aberrations have opposite signs and have an equal magnitude on the edge of the pupil; in others words, when in Equation 2.19

$$a \cdot R^2 + b \cdot R^4 = 0 \tag{2.32}$$

Also the term $\frac{1}{2}\gamma$ is plausible, because it situates the best focus in the presence of astigmatism just half way between the focal lines; the geometric spot is circular at that position. It is clear that with both aberrations the system has some broadening of the spot on the detector pinhole and thus a smaller maximum value of the detector signal. The result of Equation 2.31 is unexpected. From ray diagrams of beams with spherical aberration, see Figure 2.7, it is expected an increase of the $FWHM$; this behavior is perhaps due to the simplicity of our model and should be checked by numerical calculations. The absence of γ in Equation 2.31 shows that the average spot broadening due to astigmatism is the same as that due to defocusing.

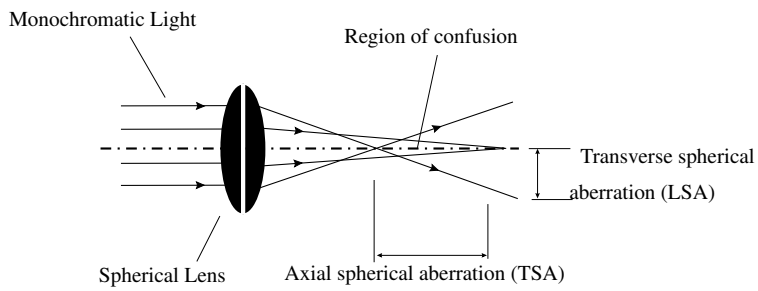

Figure 2.7: Spherical aberration

2.4.3 Coma

With coma we have a complication, because the maximum intensity of the spot on the detector pinhole is not found at the intersection of the chief ray and the image plane, as is the case with spherical aberration and astigmatism. Therefore, the wavefront aberration for coma is written as;

$$W(r,\varphi) = d \cdot r \sin\varphi + e \cdot r^3 \sin\varphi \tag{2.33}$$

in polar pupil coordinates (r,φ), where a linear term is added to find the position of the maximum. In the same way as in the previous section the Strehl's number is written

$$S = 1 - (2\pi)^2 \left(\frac{1}{4}\delta^2 + \frac{1}{3}\delta\varepsilon + \frac{1}{8}\varepsilon^2 \right) \tag{2.34}$$

where δ and ε is equal to:, $\delta = \frac{d \cdot R}{\lambda}$, $\quad \varepsilon = \frac{e \cdot R^3}{\lambda}$; the wavefront errors at the edge of the pupil, in wavelengths. It can be seen from Equation 2.34 that the maximum of S is obtained for

$$\delta = -\frac{3}{2} \cdot \varepsilon \tag{2.35}$$

At this position the Strehl's number becomes

$$S = 1 - (2\pi)^2 \left(\frac{1}{72} \varepsilon^2 \right) \tag{2.36}$$

With half a wavelength of coma the Strehl's number is already down to 0.86. Note that ε depends linearly on the field coordinate Y, this gives a quadratic decrease of S with field radius. From Equation 2.33 can be seen why coma is treated apart from spherical aberration, astigmatism and defocus. The reason is that the cross products of the terms in Equation 2.33 and those in Equation 2.19 are on average equal to zero.

2.4.4 Field curvature and distortion

With field curvature the system has a defocus that depends quadratically on the field radius, to a first approximation, (there may also be terms of higher order). Distortion gives a lateral shift of the spot that is an uneven function of the field radius, to a first approximation of the third order. Both aberrations displace the intensity curve, vertically or laterally respectively. When these displacements are known, they can be removed from the measurement result.

As a summary it can stated that chromatic aberrations, spherical aberrations, coma and astigmatism should be kept within the specified boundaries, whereas field curvature and distortion should be known so that they can be removed from the measurement result.

2.5 Depth resolution

From the depth response curve as discussed in Section 2.3 the axial position of the sample surface is determined. This is done by changing the distance between sample and probe (microscope objective) in a number of steps. Usually steps of 1/10 of the depth of focus is taken as given in Equation 2.3. There are several methods to calculate the focus position from measured intensities. Here it is

assumed that the position of the center of gravity of the depth response curve is estimated from the detector signals, $I(z_i)$, measured at a number N of focus steps z_i. For simplicity it is assumed that the center of gravity position $\bar{z}$, given by

$$\bar{z} = \frac{\sum_0^N z_i \cdot I(z_i)}{\sum_0^N I(z_i)} \tag{2.37}$$

is equal to zero when the intensities $I(z_i)$ are without error. When an error, for instance due to noise, n_i, is present in the ith measurement, the measured signal can be written $I_m(z_i)$ as

$$I_m(z_i) = I(z_i) + n_i \tag{2.38}$$

The focus error now becomes

$$\Delta\bar{z} = \frac{\sum_0^N z_i \cdot n_i}{\sum_0^N I(z_i)} \tag{2.39}$$

assuming that the n_i are zero on average. When the errors n_i are uncorrelated and have Gaussian statistics the RMS focus error is, to a good approximation, given by

$$\sigma_z = z_R \cdot \frac{\sigma_n}{\sqrt{N} \cdot I(0)} \tag{2.40}$$

where z_R is the depth of focus, given by Rayleigh's criterion or alternatively from Equation 2.3, and σ_n is the RMS measurement error. In Equation 2.40 it is assumed that the measurement positions all lie in the top of the depth response curve, between the half maximum points. Measurements further away from focus have an unfavorable signal-to-noise ratio. With a wavelength of 550 nm and a numerical aperture of 0.46 a depth of focus of about 3 μm is obtained. With a signal-to-noise ratio, $I(0)/\sigma_n$, of about 100 and $N = 10$ measurements we would have $\sigma_z \cong 9$ nm. This estimated resolution agrees with our target as formulated in Section 1.8.1. It is seen that the RMS focus error can be considerably smaller than the wavelength λ of the source. This gives a parallelism with the theory of superresolution [42] that (lateral) superresolution is possible under two conditions:

1. The object field is limited,

2. Sufficient a priori knowledge of the object.

In the case of confocal microscopy there is indeed a limited depth range (depth of focus). The a priori knowledge in this case is that there is a well-defined surface; the same result could be obtained by a coated specimen. A difference with the theory of lateral superresolution is the dependence on noise. In the developed system the depth resolution depends linearly on the signal-to-noise ratio. In the lateral case the dependence is in general much weaker, but this depends on the number of degrees-of-freedom in the object structure [69], which in the developed system is very small.

2.6 Lateral resolution

In a Type-I scanning microscope, as described in Section 2.2, the lateral resolution is determined by the point spread function (PSF), that is the intensity distribution in the image of a point source. When the imaging is diffraction limited, the $FWHM$ of the PSF of a system with a circular pupil is given by

$$\Delta x_{1/2} = \frac{1.22 \cdot \lambda}{\sin\theta} \tag{2.41}$$

The two point resolution as defined by Rayleigh [67] is half of this value. With a Type-II, or confocal scanning microscope, it is well known that the lateral resolution is about 30% better than in a Type-I scanning microscope or a conventional bright field microscope [59], for both of which Equation 2.41 is valid. This can be understood as follows:

Let a point scatterer in the focal plane move through the illuminating spot. It is illuminated with an intensity proportional to the point spread function of the illuminating system. The scatterer projects a moving intensity distribution in the detection plane proportional to the (magnified) point spread function of the imaging system. This distribution is sampled by the detection pinhole. When this is small, the transmitted power is proportional to the product of the point spread functions. With a reflective object, such as in surface characterization, the amount of radiative power transmitted by the detection pinhole as a function of the position of the scatterer is to a good approximation proportional to the square of (a cross-section) of the point spread function. This gives a theoretical improvement of lateral resolution by a factor of $\sqrt{2}$. Longitudinal chromatic

aberration, spherical aberration, coma and astigmatism all have influences on depth discrimination. In a well-designed confocal microscope these aberrations must be, for this reason, well corrected so that we can speak of diffraction limited imaging. Transverse chromatic aberration is the only primary aberration that influences lateral resolution exclusively. Therefore, it must be well corrected when one wants to profit from the $\sqrt{2}$ advantage mentioned above.

2.7 Practical aspects of confocal microscopy

The speed of measurement of a confocal microscope is related to the scanning technique used. In industrial production, where it is often important to test every product, speed of measurement is one of the parameters that determines throughput. The scanning techniques that discussed in this section are illustrated in Figure 2.8.

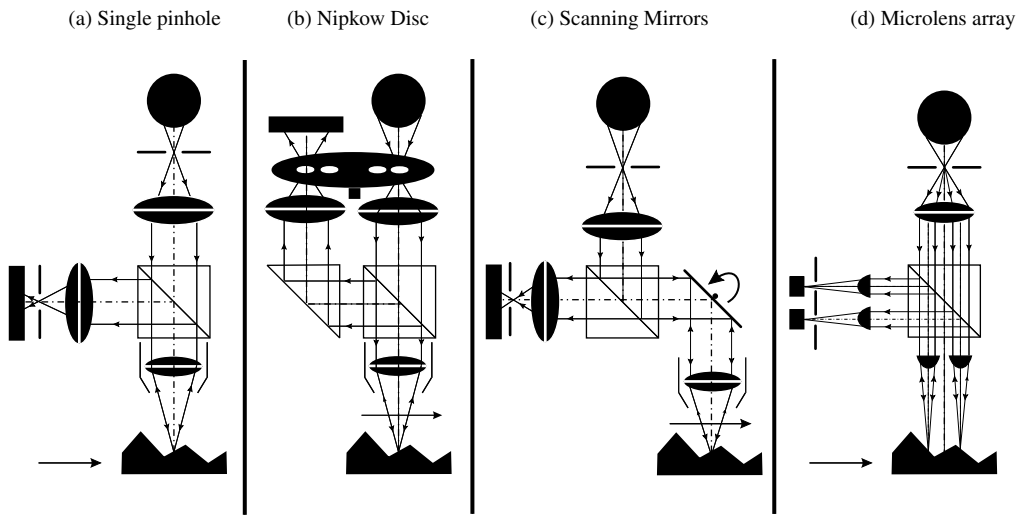

Figure 2.8: Types confocal applications

The scanning techniques shown in Figure 2.8 can be divided into single beam and multiple beam techniques. The simplest single beam scanning technique consists of a relative lateral movement of microscope and object Figure 2.8(a). The main advantage of this technique is that the illumination pinhole and the detection pinhole are situated on the axis of the optical system, so that it is not necessary to correct field dependent aberrations to a high degree, only correction

of coma and lateral chromatic error is necessary. This makes the optical system simpler and cheaper, as in CD players. A main problem of this technique is to ensure that the scanning movement occurs exactly perpendicular to the optical axis. The system of Figure 2.8(a) can also be called a confocal profilometer; because relatively heavy objects must be moved (the microscope or the object table) it is the slowest of the scanning techniques reviewed here. It is used in those applications where a good lateral resolution is important.

With multiple-beam systems, that usually also have multiple detection pinholes, the detector is either an array of diodes or an image detector, such as a CCD array. Such a system is that invented by Petran and Hadravsky [61], illustrated in Figure 2.8(b). In this system a Nipkow disk, known from pioneering early TV system [70], is used for scanning. One side of the disk is imaged onto the other side, so that the pinholes on the disk act as both illumination and detection pinholes. The system in this form has the disadvantage that alignment and production tolerances of the Nipkow disk are very narrow.

A system without this disadvantage was invented by Kino and Xiao [71]. In this system, illustrated in Figure 2.9, each pinhole of the Nipkow disk is imaged onto itself, thus acting as illumination and detection pinhole. Note that the beamsplitter in the system is situated above the disk, in the full light of the source. Because of this, a special beamsplitter design is necessary to avoid false reflections from the beamsplitter.

In a modern design of this system, the object is scanned twelve times during a revolution of the disk. To obtain a frame time of 20 msec a revolution frequency of about 4 Hz is sufficient. Such a disk contains thousands of pinholes with a diameter of about 20 μm and with a distance between pinholes of about 134 μm to avoid cross-talk between pinholes.

Another single-beam technique is illustrated in Figure 2.8(c). Here the collimated beam from the illumination pinhole is scanned over the field of the objective by a rotating mirror in the back focal plane. A single detection pinhole receives the back scattered light. Two-dimensional scanning can be obtained by adding a second scanning mirror, with its rotation axis perpendicular to the first. With

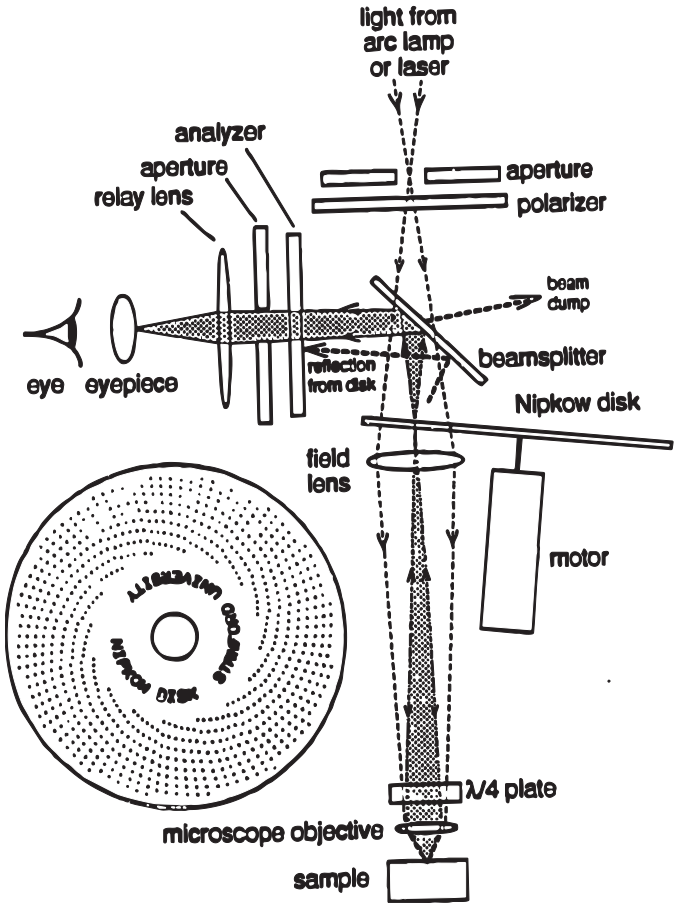

Figure 2.9: New generation Nipkow disk based confocal microscope. Developed by Corle and Xiao [4].

this technique it is customary to use a laser as a point source. This introduces the problem of false interference patterns that can be overcome by accurate coating of the optics. As the moving parts in the systems are less heavy than in the previous one, its scanning speed can be much higher. With a rotating polygon a frame time of 20 msec is possible [72]. As to lateral resolution, this technique makes much higher requirements to the optical system, especially vignetting of the laser beam must be prevented rigorously. Also the correction of off-axis aberrations becomes necessary. In single-beam/single-pinhole systems a single detector can be used, in existing systems this is often an avalanche diode or photo-multiplier, the latter when object fluorescence must be detected.

An alternative technique for multiple-beam scanning is the microlens array confocal microscope, illustrated in Figure 2.8(d), invented by Tiziani [51]. It uses arrays of about 200×200 microlenses with a diameter of $150\,\mu$m. The

distance between these lenses is also 150 μm. The object field covered is therefore 60×60 mm. The lateral resolution is limited by the numerical aperture of the microlenses. The spot array is imaged onto an array of pinholes, behind which an array of detectors is located. This system has the advantage of having no moving parts but it gives only a local sampled rendering of surface topography. In Table 2.2 a summary of the conclusions of this Section is given. White-light interferometry is used as a comparison where it was discussed in Section 1.5.1 which has the limitation of cross-talk between pixels.

Table 2.2: Numerical values of Figure 2.8.

System	Frame time	Resolution	Resolution field	Limitation
Mechanical scanning	1 sec.	10 nm 10 μm	0.5 μm $>> 1 \times 1$ mm	slides movement
Nipkow disk	20 msec.	2 nm 10 μm	1 μm 1×1 mm	beam splitter disk wobble
Scanning mirrors	$0.25 - 0.02$ sec.	5 nm 10 μm	1 μm 1×1 mm	scan frequency
Lens array	20 msec.	50 nm	1 μm 60×60 mm	numerical aperture
Mirau interferometry	20 msec.	1 nm 10 μm	2 μm 1×1 mm	cross-talk artifacts

2.8 Summary

In this Chapter after a short summary of confocal microscopy and the types and the advantages of it the two former studies from Corle [4] and Jordan [73], where confocal microscopy was examined with reflected surfaces, is in detailed discussed. The unsolved problems for both diffusely and specularly reflected surfaces were discussed and a theory was built for broadening of depth response curve. Also the affect of the aberrations on the system's lateral and vertical resolutions is discussed.

3. MICROMIRROR BASED CONFOCAL MICROSCOPE

3.1 Toward a new type of confocal microscope

In Chapter 2.7 a number of practical realizations of the confocal microscope were reviewed. Three out of four types that were discussed there, are regularly used for the characterization of surfaces. These are:

- the confocal profilometer (with mechanical stage scanning),
- the laser scanning confocal microscope (with mirror scanning),
- the white-light confocal microscope (with Nipkow disk),

and their properties were reviewed in Table 2.2.

In this thesis a new and different type of scanning confocal microscope will be presented. The aim of the new type confocal microscope can be easily found from Table 2.2. The performance of the existing instruments can be improved. That means:

- Shorter frame time,
- Better depth resolution,
- Larger depth range,
- Better lateral resolution,
- Larger field of view.

Also a new instrument could be free of some of the limitations of existing instruments. There are also other aspects to be considered:

- user friendliness (easy operation)

- influence of the environment
- price-performance ratio

For the user there are arguments to prefer one instrument above another:

- flexibility of applications,
  this means, applied to surface characterization, that the instrument can be used to measure all categories of surface topography, as mentioned in Section 1.4 and that the measurement is largely independent of the material of the surface. Also limitations of slope and curvature should not to be too inconvenient.
- from the standpoint of the user, not all performance parameters mentioned above are equally important. It could be that for instance a shorter frame time is more urgent than the best lateral resolution.

The sensitivity of the instrument to its environment determines to a great extent where the instrument is going to be used. In the research laboratory, in the measuring room, on the factory floor or even outdoors. Environmental aspects to be considered are:

- temperature changes,
- vibrations and shocks,
- dust,
- room light,
- electro-magnetic interference and compatibility.

The list is certainly not complete. As to price-performance ratio it should be noted that some users prefer a low price above a high performance. So that even when a new instrument has, in some respects, a lower performance than existing instruments, it is nevertheless preferred when the price is significantly lower.

In the following a new type of confocal microscope, based on the use of a micromirror array as a scanning illumination device will be presented.

3.2 Analysis of the Microscan system's components

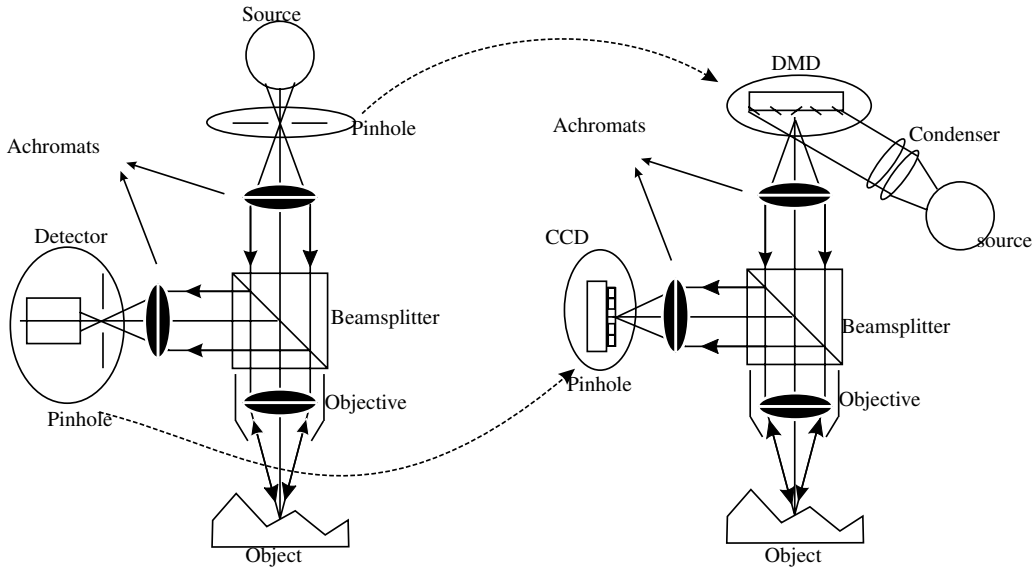

Figure 3.1: Illustration of DMD based confocal system (Microscan) by comparing to with the classical confocal microscope

The establishment of the virtual pinholes based confocal microscope (Microscan) system is illustrated in Figure 3.1 in comparison with the principle of a classical confocal microscope with mechanical scanning. The main differences between two systems are:

- instead of classical illumination pinholes a Digital Micromirror Device (DMD^{TM}) completed with its off-axis illumination system is used. The light source is a Xe-arc lamp and the light is transported to the microscope with the help of a fibre-bundle,
- a CCD-array, where the each pixel is used as detection pinhole, is selected as the detector.

The microscope objective, the two tube lenses (for which we use standard achromats) and the beamsplitter are the same in both systems. Depth scanning can be performed by moving the microscope, the object or by translating the objective by a piezo-actuator. In the following sections the key components of the system will be reviewed:

- the DMD^{TM}unit,
- microscope objective,
- CCD array.

3.2.1 The DMD and its properties

The Digital Micromirror Device (DMD) is one of today's most successful MEMS. It was invented in 1987 after 10 years of development by L.J.Hornbeck at Texas Instruments and continuously improved and enhanced until today. Modern DMDs, shown in figure 3.2(a), consist of up to 2048×1024 micromirrors made of an aluminum alloy. DMD is a semiconductor-based array of fast, reflective digital light switches that precisely control a light source using a binary pulse-width -modulation technique. The DMD chip size and single micromirrors details are given in Figure 3.2(a) and Figure 3.3(b). Each DMD mirror is $16\,\mu\text{m} \times 16\,\mu\text{m}$ in size with a $1\,\mu\text{m}$ gap between them, resulting in a DMD filling factor of approximately 89% [74].

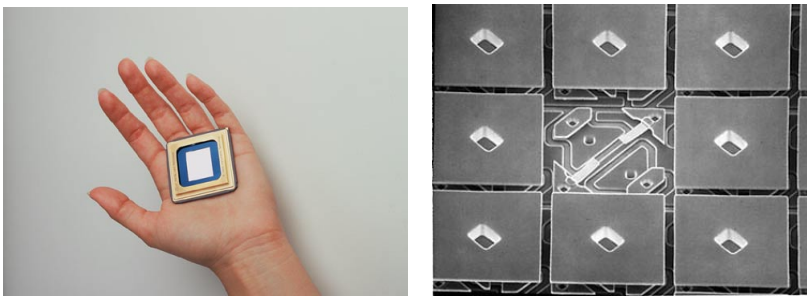

(a) Image of a full DMD chip in hand (b) Detailed image of DMD pixels and tilting mechanism

Figure 3.2: Image of a DMD chip and the detail of the group of DMD pixels

By electrostatic attraction each mirror can be individually tilted around its diagonal axis over an angle of $\pm 10°$ within $15\,\mu\text{s}$ depending on the state of the underlying memory cell. Some of the most important properties of DMDs are summarized in Table 3.1.

Table 3.1: DMDs specifications list

Manufacturer	Texas Instruments
Mirror Size	16 μm $\times$ 16 μm
Gap Between Mirrors	1 μm
Filling Factor	89%
Mirror Material	Aluminum alloy
Mechanical Switching Time	15 μs
Available Resolutions	800×600
	1024×768
	1280×1024

In its' original application, digital image projection systems, the DMD operate to reflect light from light source through a projection lens onto a screen, with each mirror representing a single pixel of a complex image. Gray scales are generated by high speed pulse width modulation of the mirror positions and colors can be created, for instance, by using a color wheel and time multiplexing the red, green and blue components of the image. Beside the application of digital image and video projection, DMDs are also used for digital fringe projection systems in the filed of optical metrology. Since the DMD can also operate as a pinhole, it may as well be used as flexible scanning device in a confocal microscope [52] [75] [53] [**?**]. Now it can be focused on some important specifications of the DMD for confocal microscope applications.

3.2.1.1 DMD as a light switch

The DMD as a light switch is shown in Figure 3.3(a). Each DMD pixel acts as an light switch that can reflect light in one of two directions, depending on the state of the underlying memory cell. Rotation of the mirror is accomplished through electrostatic attraction produced by voltage differences developed between the mirror and the underlying memory cell. With the memory cell in the "*on*"or (1) state, the mirror rotates $+10°$. With the memory cell in the "*off*" or (0) state, the mirror rotates $-10°$. The DMD light switch is able to turn light *on* and *off* rapidly by the beam-steering action of the mirror. By combining the DMD with a suitable light source and illumination optics, Figure 3.3(b), the mirror reflects incident light either into or out of the pupil of the tube lens by a simple beam-steering technique. Thus, on the (1), **on**, state of the mirror appears bright and on the

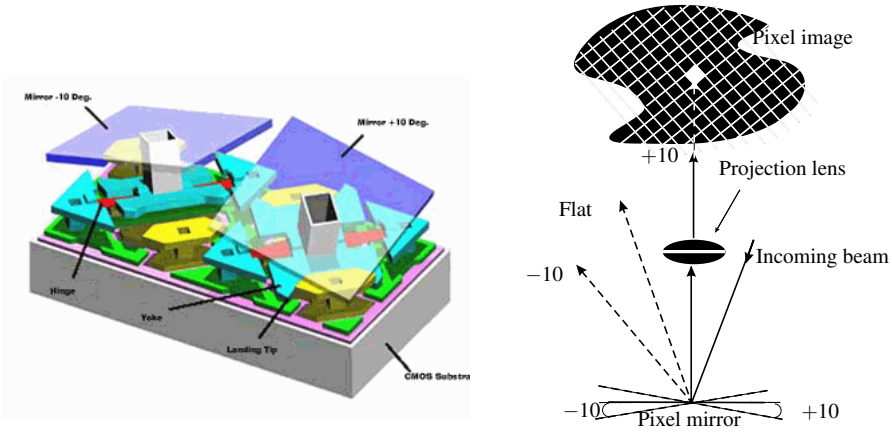

(a) DMD mirrors positions. Each DMD mirror is capable of tilting ±10° around its diagonal axis

(b) DMD optical switching principle. According to the position of the DMD mirror reflected light is either directed into the optical system or outside the optical system, in most cases to a light trap

Figure 3.3: The idea of using a DMD unit as an optical switch

(0), **off**, state of the mirror appears dark. Compared to diffraction-based light switches, the beam-steering action of the DMD light switch provides a superior trade-off between contrast ratio and the overall brightness efficiency of the system.

The optical switching time for the DMD light switch is approximately 2 μs. The mechanical switching time, including the time for the mirror to settle and latch, is approximately 15 μs [9].

3.2.1.2 Grayscale operation

Grayscale illumination is achieved by binary pulse-width-modulation of the incident light. As the mirror rotates, it either reflects light into or out of the pupil of the projection lens, to create a burst of digital light pulses. The details of the binary pulse-width-modulation (PWM) technique are illustrated in Figure 3.4. For simplicity, the PWM technique is illustrated for a 4-bit word (24 or 16 gray levels). Each bit in the word represents a time duration for light to be *on* or *off* (1 or 0).

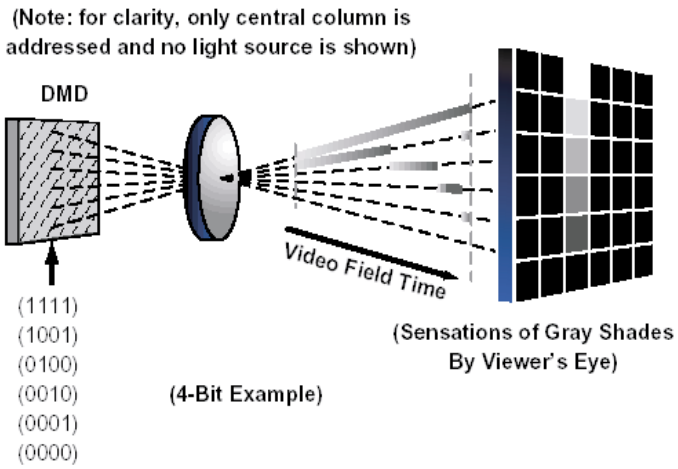

Figure 3.4: The idea of the grayscale operation

3.2.1.3 Resolution

DMD chips are produced at a variety of resolutions, SVGA (800×600), XGA (1024×768) and SXGA (1280×1024). The DMD family of chips uses a common pixel design having a $16\,\mu$m mirror arrayed with a $17\,\mu$m pixel pitch. As the DMD resolution is increased, the pixel pitch is held constant so that the chip diagonal becomes larger in proportion, see Figure 3.5.

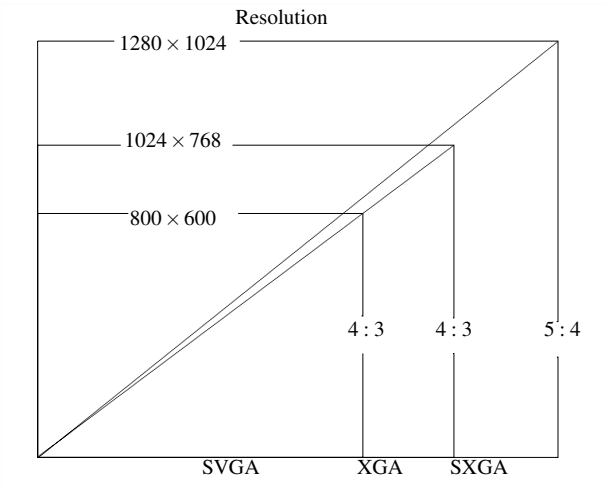

Figure 3.5: DMD resolution vs chip diagonal

This approach has some advantages;

- the optical efficiency and contrast ratio of the pixel are maintained at all resolutions,
- the pixel timing is common to all sizes,
- the chip diagonal increases with resolution, which improves the DMD based system optical efficiency.

3.2.1.4 Optical efficiency and contrast

The optical efficiency of DMD based systems is the product of the efficiencies shown in Figure 3.6, namely the lamp-projection-lens and pixel efficiencies. The pixel efficiency is composed of several factors namely the fill factor, mirror *on* time reflectivity and diffraction efficiency. The efficiency of a DMD based systems can reach maximum 61% [76]. The illumination efficiency depends on the reflection

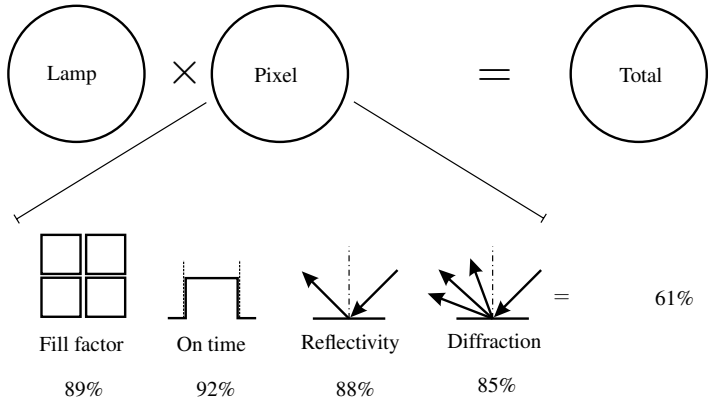

Figure 3.6: Optical efficiency of DMD based systems

and absorption in the components of the illumination system, on the geometry of the light source, the numerical aperture of the condenser lens and the ratio of beam and chip area. The contrast ratio is defined as the ratio of the light flux with all pixels turned *on* and the flux with all pixels turned *off*. In a DMD, it is limited, with a DMD, by diffraction from the mirror edges, the substrate and the metalized holes in the center of the mirror, where the support post is situated, Figure 3.3(a). The estimated contrast ratio of the developed system is about $7:1$; this estimation will be discussed in detail in Chapter 4.

3.2.1.5 Applications

DMD based projection systems are well suited to high-brightness and high-resolution applications [50] [74] [77]. DMD is a key component in digital projection systems, that require digital video input and produce digital light output. Grayscale operation can be achieved by pulse-width-modulation; colored images can be produced by the use of a color wheel and time-multiplexing the color components of the image. Beside the application in image projection and digital video, DMD's are also used in fringe projection systems for optical metrology [31] [?] [78].

3.2.2 Microscope objectives

Many considerations must be taken into account while choosing a microscope objective that suits the needs of the Microscan system. Apart from the obvious points such as field of view and numerical aperture also the correction of aberrations is important. Because polychromatic light is used for illumination the chromatic aberrations must be well corrected. Spherical aberration, coma and astigmatism must not exceed the diffraction limit. Distortion and field curvature can be tolerated to a small amount. The working distance (clearance) becomes important when specimens with large differences in depth are introduced. It will be clear that only the metallurgic type of objective, where no cover glass is used, can be considered for use in the developed system. In the following a few types of objectives with respect to their suitability will be discussed.

3.2.2.1 Achromatic objectives

In this type of objective glasses of different refractive index and dispersion are used to correct chromatic aberration. The secondary spectrum will cause a broadening of the depth response curve. With achromatic objectives spherochromaticity[1] cannot be corrected very well.

[1] the dependence of spherical aberration on wavelength

3.2.2.2 Fluorite objectives (semi-apochromatic)

The secondary spectrum can be reduced considerably by the use of fluorite glass in the design. This leads to a narrower depth response curve with a higher maximum and improves the depth resolution. Also the lateral resolution will be better than with an achromatic objective. The spherical aberration is still only corrected for one primary color (green). Fluorite glass exhibits some strain birefringence and is therefore not ideal in combination with polarization or fluorescence microscopy.

3.2.2.3 Apochromatic objectives

This type of objective is fully corrected for the three primary colors. The secondary spectrum is practically eliminated. Spherical aberration is corrected for blue and green. Apochromatic correction is usually applied to objectives of high power and high numerical aperture. Because of the need for special types of optical glass, the higher number of components and narrower production tolerances, these objectives are expensive (3-4 times the price of an achromatic objective); it does not follow that they are better for each application. Usually the working distance is rather small. The increased numerical aperture can induce increased glare that must be under control by reducing the field of view.

3.2.3 The image detector

Requirements for the image detector in the Microscan system are:

- high signal to noise ratio (SNR),
- resolution compatible to that of the DMD.

The image detector that is universally available is the Charge Couple Device (CCD) array. In order to avoid Moiré effect between the CCD and the DMD unit a CCD array with square pixels and a number of pixels about equal to the DMD that was chosen. The size of the pixels was $8.3\ \mu\mathrm{m} \times 8.3\ \mu\mathrm{m}$, the number of pixels $782\ \mathrm{h} \times 582\ \mathrm{v}$ where the DMD has $800\ \mathrm{h} \times 600\ \mathrm{v}$ pixels. The noise in a CCD array image detector has several components [70]:

- photon noise, due to the quantization of the incoming light; in our case this is incoherent light so that the photon noise has Poisson statistics,
- dark-current noise, this is the prominent noise source,
- read out noise, caused by the read-out amplifier.

The RMS dark-current noise in a room temperature CCD with MOS photo diodes is 1000 electrons per pixel. The number of electrons stored per pixel is of the order of 100.000 so that a SNR of 100 is a realistic value. By cooling of the CCD the SNR can be improved; this option was not used during the project. The spectral sensitivity of silicon CCD-arrays decreases about linearly from a quantum efficiency of about 30% at 700 nm to 8% at 400 nm. For this reason a Xe-arc lamp that has a fairly continuous spectrum in the visible region of the spectrum is used in the system. To avoid chromatic broadenning of the depth response curve a green filter with a peak transmission at 550 nm can be used.

3.2.4 Results of system analysis

The system analysis can be shortly summarized as:

- For the microscan project a suitable microscope objective type is the semi-apochromatic (Fluorite) objective,
- The selection of the proper type of DMD depends on the lateral resolution of the system components. In other words, the light source (wavelength) and microscope objective NA value. For the chosen microscope objectives and light source (0.55 μm) these values are given in Table 3.2. The best choice for the Microscan project is a SVGA type DMD unit which has 800×600 pixel resolution.

Selected system components With the help of the knowledge built up to now, the following system components are chosen for the next step in the project, see Table 3.3.

Table 3.2: Selection of the proper DMD type

Microscope objective			Lateral Res. for DMD type		
Magnification	NA	Lateral Resolution μm	SVGA 400 pixel in FoV	XGA 500 pixel in FoV	SXGA 600 pixel in FoV
20	0.46	0.73	3.31	2.65	1.33
50	0.8	0.42	1.33	1.06	0.53
100	0.95	0.35	0.66	0.53	0.27

Table 3.3: Selected system components and their specifications

Imaging system CCD	
Effective picture elements	782×582 (horizontal/ vertical)
Sensing area	$\frac{1}{2}$ inch-size
Cell size	8.3×8.3 μm (horizontal / vertical)
Chip size	8.10×6.33 mm (horizontal / vertical)
DMD unit	
Pixel numbers	800×600 pixels (horizontal/ vertical)
Pixel size	16 μm $\times$ 16 μm
Microscope Objectives	
UMPLFL 20$\times$	NA $= 0.46$
UMPLFL 50$\times$	NA $= 0.80$

3.3 Establishment of the optical set-up

By using the key elements, DMD, microscope objective and CCD camera, different matching possibilities between the DMD and the CCD can be created. Figure 3.7 shows the critical areas that determine the matching condition of the Microscan system. By nature each microscope objectives has it's own circular field of view (FOV) area which is given by the manufacturer specifications. In a similar way the chosen CCD camera and the DMD unit have their own usable areas, different from the circular FOV area, in rectangular shape, which cause partly matching difficulties with the microscope objective's FOV area.

3.3.1 A basic approach for the optical set up

The main approach in the Microscan project is to use the key and most expensive element, the DMD unit, as efficiently as possible, in other words to use maximum

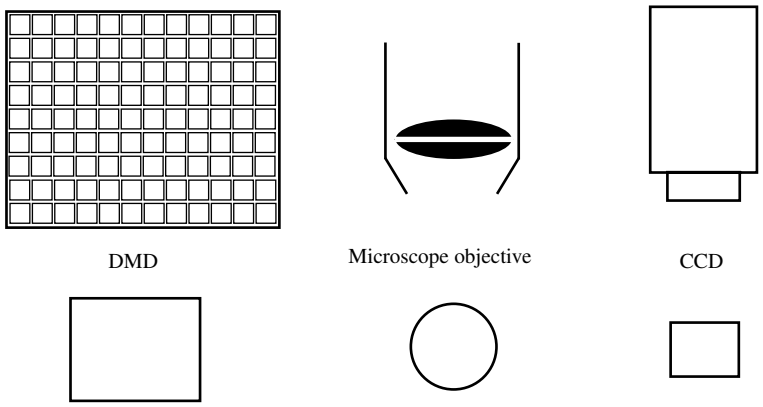

Figure 3.7: Basic limitations for the matching between the Microscan components

area on the DMD unit. For this purpose the microscope objective's FOV is matched with both the DMD and the CCD chip area in order to use the full DMD and CCD areas. It is quite possible to create some series of alternative matching conditions according to the existing areas. Basically the created solution mostly depends on the aimed purposes, such as:

- in order to use the maximum FOV area,
- in order to use the maximum DMD area.

The number of matching conditions could be increased just by using a different combination between the given areas. For given sets of specifications and constraints one or more concepts for an opto-mechanical system can be created. Two alternative matching conditions for the Microscan system were formerly developed and tested during the early stage in the project [52] [79]. In the following, the starting idea and final design approaches will be explained, presented and simulated. At this stage of preliminary design, all optics are accepted as thin lenses. The locations, sizes and orientations of images and pupils are correct to a first order approximation in this ideal representation. In order to obtain the Microscan layout specifications, i.e. the related focal distance and lens diameters, one could start with a simple $2D$ model of the optical system by using the primary elements specifications (CCD and DMD) and just by ignoring the beamsplitter, Figure 3.8.

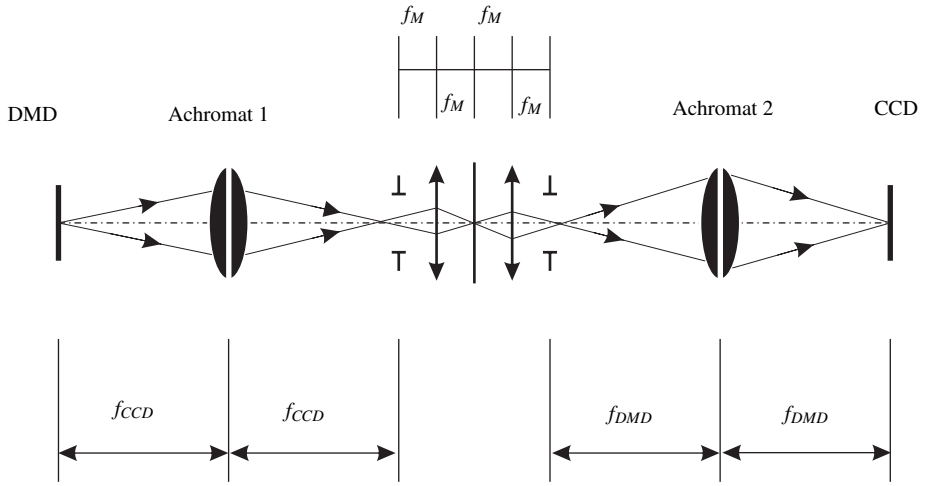

Figure 3.8: 2D scheme of the developed system.

The parameters given in the 2D scheme present:

- f_{DMD}, focal length of the achromat 1,
- f_{CCD}, focal length of the achromat 2,
- f_M, focal length of the microscope objective.

In order to establish the lay-out of the optical system the FOV of the microscope objective is adapted to the usable area of the DMD and the CCD, Figure 3.9.

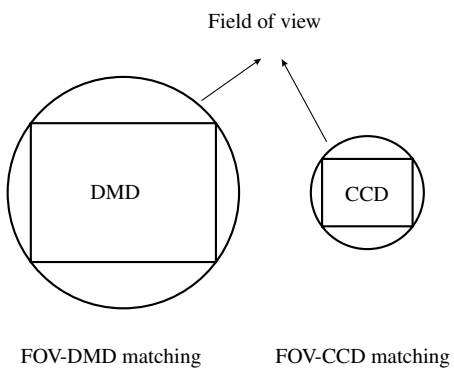

Figure 3.9: Matching approach on DMD and CCD

The microscope objective that will be most frequently used is a 20× magnification microscope objective, with a 1.1 mm FOV of diameter. This enables to obtain

profiles of 800 μm long, which is a standard for the cut-off length in roughness measurements for mechanical stylus measurements [19]. When the diagonal length of the DMD image is equal to 1 mm, the whole DMD image fits comfortably inside the FOV of the microscope objective. The long side of the DMD image is now shrunk to 0.8 mm. The DMD itself has a long side of 13.6 mm so that the required magnification from object to DMD is $13.6/0.8 = 17$ times. The focal length of the 20× microscope objective is 9 mm and it requires a tube lens with a focal length of $9 \times 17 = 153$ mm. In the suppliers catalog available achromats with focal lengths of 150 mm and 160 mm and the first value is preferred because it is nearest to 153 mm and there is still some spare room inside the FOV. The usable area of our CCD has the same form as the DMD but its dimensions are a factor of 2.1 smaller. Therefore a tube lens of focal length 80 mm or 75 mm is taken on the side of CCD.

After determining the rough focal distances and image-object relations, it can be continue with the improved and detailed $2D$ schema. Even if it is thought that theoretically light travels parallel after achromat 1 and the position of the microscope objective is not important, in reality this is not true for the outer DMD mirrors. This off-axis problem, which mainly causes a vignetting effect, must be taken in to account. The aim of this design is to minimize the vignetting effect in the system and to obtain as much light as possible at the position of the microscope objective's entrance pupil. In the current situation the distances between the tube lenses and the objective are still free. It is aimed to have a system that is tele-centric on the side of the object, so that the defocusing of the object does not change the magnification with respect to the DMD and the CCD. That means that the stop of the objective must be in its back focal plane. Fortunately, the supplier has already taken care of this. In order to achieve the aimed tele-centricy on the side of the CCD and the DMD the stop must be in the focal plane of both tube lenses. This fixes the distances from the tube lenses to the objective. An optical path correction must be introduced for the thickness of a cube beamsplitter. This correction is given by Equation 3.1 and shown in Figure 3.10.

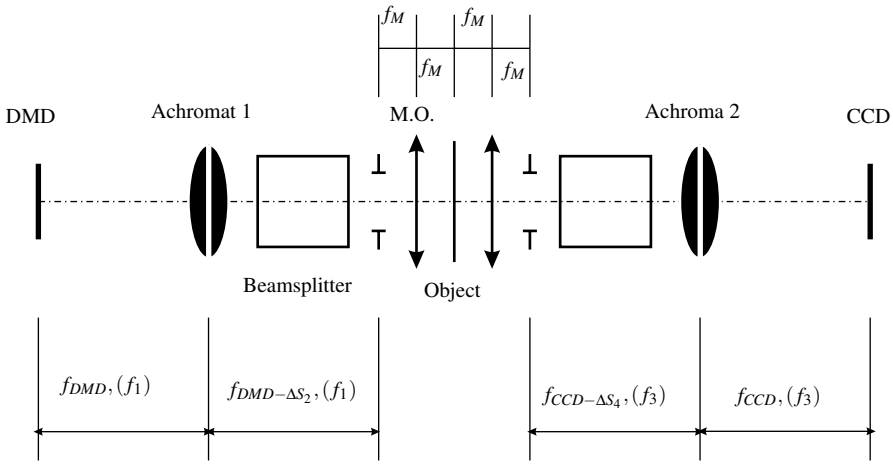

Figure 3.10: 2D scheme of the developed system where M.O. is used for microscope objective

$$\Delta S_2 = \Delta S_4 = \frac{1-n}{n} d, \tag{3.1}$$

where d is the thickness of the beamsplitter. In our case $n = 1.517$ and $d = 25$ mm so that $\Delta S_4 = \Delta S_2 = -8.52$ mm. The last step in establishing the lay-out is the calculation of the required diameter of the tube lenses. The numerical aperture of the DMD side tube lens is $0.46/17 = 0.027$. This means that the diameter of this tube lens must be at least equal to

$$\Phi_1 = 17 + 2.150 \times 0.027 = 25.1 \text{ mm} \tag{3.2}$$

The diameter of the CCD side tube lens must be more than 16.6 mm. The catalog lenses have a free diameter of 25.4 mm. The dimensions of the lay-out,Figure 3.10, are given in Table 3.4. It is assumed that the light source (the end of a fibre-bundle $\Phi = 3$ mm) is placed in the focal point of the condenser, so that its image is projected in the stop of the objective.

For scanning steps in z direction it is accepted that the vertical scanning steps will be approximately 10% of the related DoF, Table 3.5, it means that for each microscope objective the calculated DoF value will be scanned in ten steps by the piezo element.

Table 3.4: System specification summary

Tube lens	$f_1 = 150$ mm	$\Phi_1 = 25.4$ mm
Distance S_2	$S_2 = f_1 - \Delta S_2 = 141.5$ mm	
Objective	$f_2 = 9$ mm	
Tube Lens	$f_3 = 80$ mm	$\Phi_2 = 25.4$ mm
Distance S_4	$S_4 = f_3 - \Delta S_4 = 71.5$ mm	

Table 3.5: DoF and Vertical Resolution relation table

Depth of focus (μm)	**Vertical scanning step (μm)**
1.1	0.11
0.43	0.043
0.34	0.034

From these calculations and the two important system parameters, namely the achromats focal length at the DMD and the CCD sides, 150 mm and 80 mm, the optical schema can easily be built.

3.4 Ray tracing analysis

Up to now, during the calculations for the optical path of the rays in the system, it is assumed that the lenses are thin lenses (first-order, paraxial optics). However, the first order theory is no more than just a good approximation. Deviations from the ideal conditions are known as aberrations. As described in Hecht [80] and Born & Wolf [66], there are several types of aberration such as spherical, coma and astigmatism. In the optical scheme of the developed scanner, there are 3 lenses in the system including the microscope objective. Both, lens 1 and lens 2 are achromatic doublets, which consist of a combination of a positive convex crown glass lens and a negative concave flint glass lens. The advantages of an achromatic doublet are reduction of chromatic aberration, as well as correction for spherical aberration (SA) and coma. Though these aberrations can be reduced by the use of achromats, a complete correction for SA is not possible. The use of analytical ray tracing, instead of the paraxial theory, gives us a more realistic impression of the actual optical paths through the system. A full description of this method can be found in [67] [80]. As this method requires a lot of computations, for

this reason the ZEMAX^{TM}program has been used. In a 3D scanner system, the requirement is that the focusing beam on the object must have the smallest spot diameter. The ray tracing analysis is started with the assumption that the objective is an ideal lens with $f = 9$ mm and $NA = 0.46$. This means that the diameter of the stop, in the back focal plane, is equal to 8.1 mm. The calculations are done with cemented achromatic doublets from the Linos catalogue. The data for these doublets are given in Table 3.6.

Table 3.6: Microscan system lens data

Type	Achromat 1	Achromat 2
Number	322227	322307
Surfaces	5	4
Effective focal length	150.504	80.86075

Figure 3.11 illustrate the complete optical train, here it is assumed that the object is exactly focused.

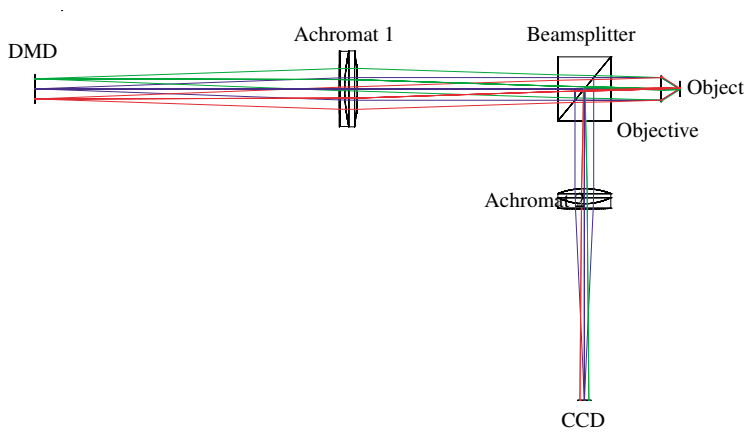

Figure 3.11: First simulation schema

The calculation was executed for 5 points on the DMD, see Figure 3.12, with the specifications given in Table 3.7.

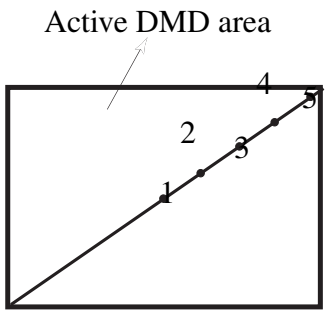

Figure 3.12: Selected simulation points on the DMD

Table 3.7: Simulation field table

Field number	X,Y position on the DMD in mm	Remarks
1	0,0	Center DMD mirror
2	1,1	
3	2,2	
4	3,3	
5	4,4	Outer DMD mirror

The results of these calculations are shown in Figure 3.13 and Figure 3.14. These figures show that the spot diagram falls inside the first Airy ring for all the field points.

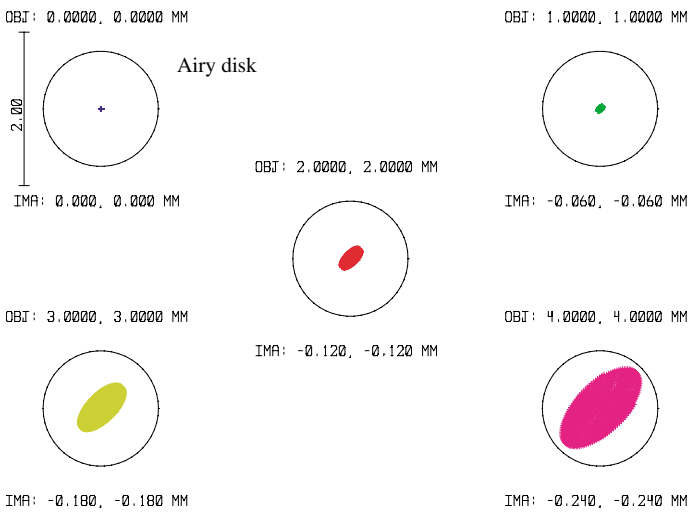

Figure 3.13: Spot diagram on the object, the system is focusing for center DMD.

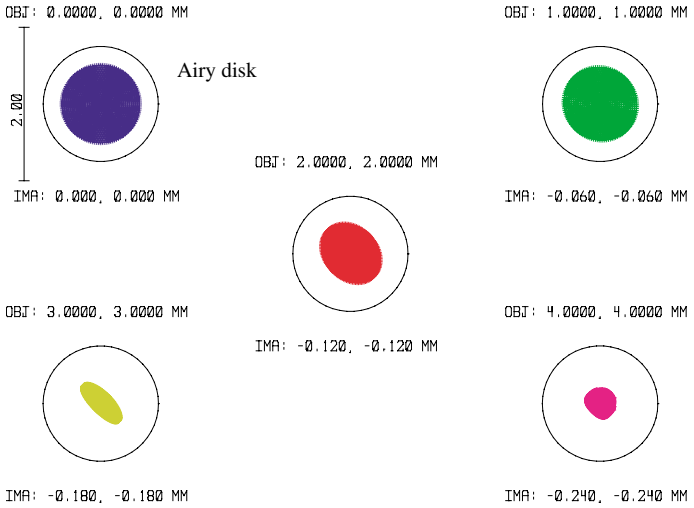

Figure 3.14: Spot diagram on the object, the system is focusing for outer DMD.

Spot diagrams on the CCD are given in Figure 3.15 and in Figure 3.16 for focusing center DMD field (1) and for focusing outer DMD field (4) respectively.

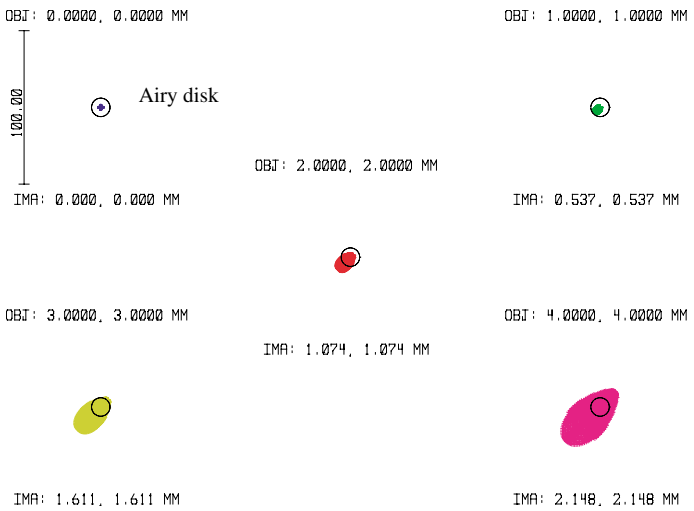

Figure 3.15: Spot diagram on the CCD, system is focusing for center DMD mirror

Although the data of our microscope objectives are not available to us to simulate, from the literature [81] it is inferred that the current objective design can result in near-diffraction-limited imaging over the whole FOV. Therefore the ideal lens approach is accepted. In order to simulate the depth response curve the

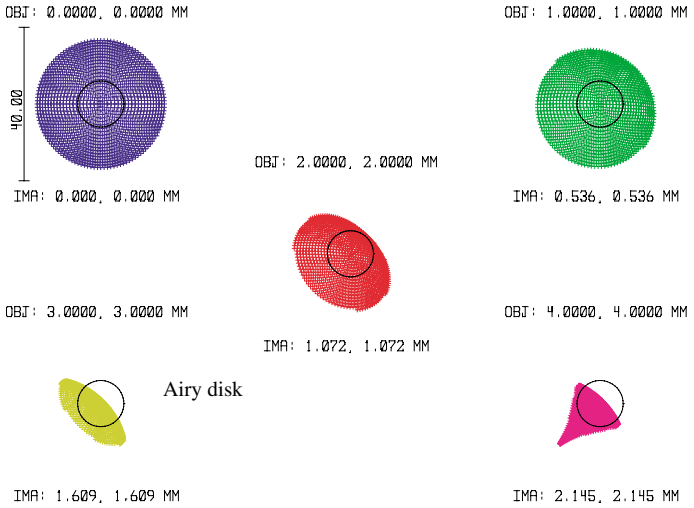

Figure 3.16: Spot diagram on the CCD, system is focusing for outer DMD mirror

defocusing of a specularly reflecting object is simulated by changing the distance between object and objective in steps of $0.1\lambda/\sin^2\theta$. 7 steps are taken on both sides; with $\lambda = 550$ nm and $\sin\theta = 0.46$, we have $\Delta z = 260$ nm per step. After each step the point spread function and from that the energy within a circle of radius $0.61\lambda/\sin\theta = 0.73$ μm is calculated, this is the radius of the first dark ring of the Airy pattern. This exercise is done for the five field positions defined above, and after fitting a polynomial through the calculated points the five depth response curves shown in Figure 3.17 are obtained.

The ideal depth response curve, as given by Corle [63] is shown in Figure 2.6. The effects of broadening and sagging down predicted in Section 2.4 can be seen. The results are found in Section 2.4.2 that predicted narrowing of the depth response curve in the presence of spherical aberration are not confirmed by this calculation. To give an impression of lateral resolution the point spread functions of the illumination and detection subsystems (with the beamsplitter included) is calculated.

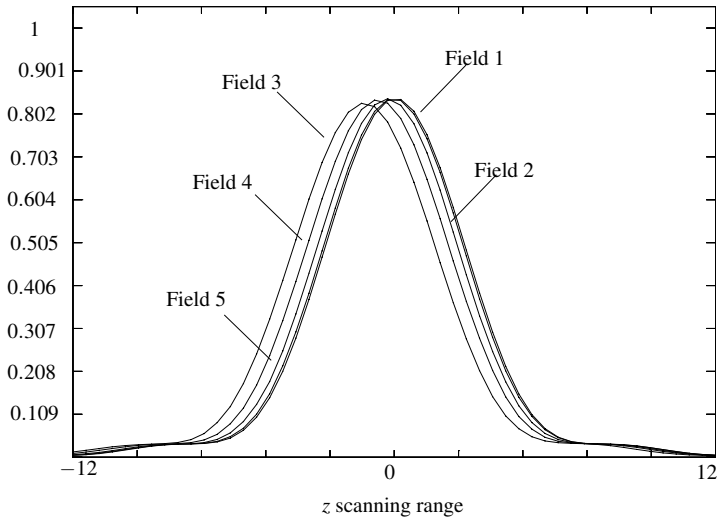

Figure 3.17: Depth response of the developed system for the ideal objective application

3.5 Tolerance budget and worst-case design

In order to predict the performance of the developed system an error budget performance analysis are done. During the analysis the following contributers to the system are taken into account, Figur 3.18.

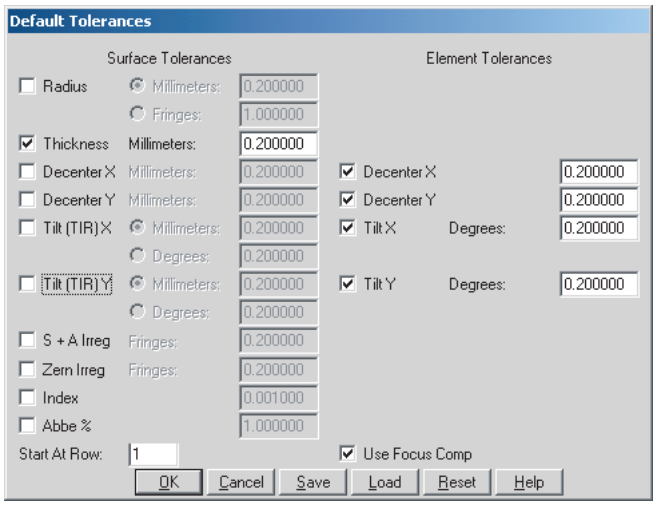

Figure 3.18: Screen shot for Zemax tolerancing

There are several categories of error sources need to be accounted for:

- Errors in fabrication (*will not be analyzed*)

  - Incorrect radius and curvature,
  - incorrect thickness,
  - incorrect surface shape,
  - curvature center offset from mechanical center,
  - incorrect or unwanted conic or other aspheric coefficients.

- Errors in material (*not examined*)
  - Index accuracy,
  - index homogeneity,
  - index distribution
  - Abbe number dispersion

- Errors in assembly
  - elements offset from mechanical axis,
  - elements positions wrongly,
  - elements improperly tilted relative to the optical axis,
  - elements having wrong orientation

- Errors due to environment
  - Thermal expansion (contraction) of materials (optical & mechanical),
  - thermally induced changes in the refractive indices.
  - alignment sensitivities introduced by system shock and vibration
  - mechanical stresses,
  - elements having wrong orientation

Figure 3.19 shows the simulated critical movements in the developed system:

- tilt and decentering of the tube lenses,
- tilt of the beam splitter,
- tilt of the objective.

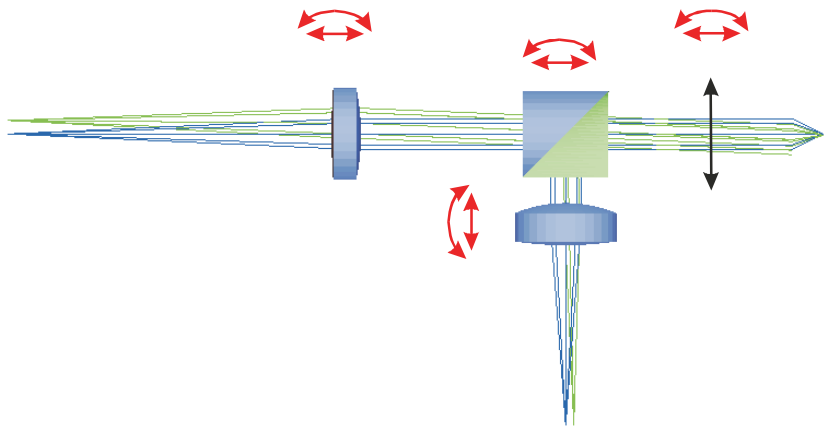

Figure 3.19: Error sources in the system

3.5.1 Establishing Tolerances

There are several steps in the analysis of tolerances:

- Determine a " figure of Merit" to use as a tolerance criteria
  - For current system it is focused on two merit function these are RMS spot size and MTF profile of the developed system
- Determine how much the system performance can depart from design
- Define initial set of tolerances
  - Default ZEMAX values accepted as start point
- Evaluate the the tolerances (according to following items) to estimated the expected cahnge in performance
  - sensitivity
  - Inverse sensitivity
  - Monte Carlo

This study on tolerancing gives a clear insight about how the relevant optical components affect the quality of the image spot diameter and the image quality.

For the tolerance set-up, calculations of the effects introduced by misalignments of the each individual component (tilting and decentering) are performed.

It is not necessary to consider decentering of the objective, because only the relative decentering of objective and tube lenses is relevant. Because the tube lenses have a FoV magnifican of 17 and 8.5 mm, respectively, a decentering of 0.1 mm will change the aberrations only to a small amount. A tilt equal to the decentering divided by the focal length is roughly equivalent to the decentering. For the DMD-side tube lens, from Figure 3.10, this is equal to 2/3 of a mrad for the CCD side tube lens it is 4/3 of a mrad. A tilt of the objective of 1 mrad is introduced. The spot diagrams for the individual centering errors and for the worst case, where all errors are present simultaneously are simulated and just a little variation which can be omitted in spot size and MTF profile is observed.

3.6 Summary

The results of the optical design and simulations can be listed as follows:

- The overall performance for the current system can not be accepted as a diffraction limited system,
- In order to avoid aberrations in the system, especially for the outer DMD fields, it is necessary to improve the system. The easy solution is to make the focal distances longer; this idea will be discussed in detail in Chapter 4
- Thin lens calculations are sufficient to establish the optical set-up,
- Because of the quite high optical tolerances the optics that is used in Microscan, accepted and treated as low precision components
- Because of the nature of the FoV, it is not possible to use the complete area of the DMD and the CCD,
- In order to obtain high efficiency from the light that we use, we must place the objective entrance pupil at the lens back focal plane,
- Simulated mechanical design tolerances quite big and the system can be accepted *low precision system.*

4. EXPERIMENTAL SET-UPS and MEASUREMENTS

4.1 Introduction

This chapter presents the realization of the micromirror based confocal microscope *Microscan* that was described in Chapter 3. In comparison to Kino's RSOM (Real-time Scanning Optical Microscope), described in Chapter 2 the developed microscope does not use a physical pinhole array. The mirrors of a DMD unit are used as virtual illumination pinholes and the pixels of a CCD array as virtual detection pinholes. As a result the optical system becomes simpler and easier to align and to adjust. Furthermore this new design eliminates the sources of vibration and stray light from the system that caused problems in the existing system. In Section 4.2 some experimental results related with replacing the Nipkow disk with a DMD will be presented. Simply the depth response curves were measured in a semi-confocal set-up, with a real pinhole on the illumination side and a CCD array on the detection side and compared with the depth response curve which was obtained with the DMD based virtual pinhole. This led to the establishment of a new type of confocal microscope, in which the DMD unit is replaced by a set of pinhole masks, Section 4.3. Section 4.4 presents two different set-ups of the Microscan system. The first set-up is based entirely on the design that was described in Section 3.3. After preliminary measurements it was concluded that some modifications of the set-up were necessary. This led to the second set-up, with which the measurements were performed. The measurements were used for the verification of the Microscan concept where the developed system is aimed to be used in surface characterization. Therefore measurements were focused on to verify whether the system is able to obtain the 3D surface topography of representative samples. Section 4.5 gives a detailed description of the procedure that is followed in the measurements. Section 4.6 describes and discusses the measurements that were used in the verification of

the Microscan concept. Finally, Section 4.7 discusses the performance and the limitations of the Microscan system.

4.2 Comparison of real pinholes with DMD pixels

Pinholes are the most important parts of a confocal microscope. Replacing them by a different device can have a negative influence on the advantages of confocal microscopy. For this reason it was decided to do first an experiment to check the effects of replacing the real physical pinhole by a DMD pixel. From literature [74] it is well known that the contrast ratio between the *on* and *off* states of a DMD pixel - although it is better than in other digital projection systems- is clearly worse than that of a pinhole. With a DMD the *on* state intensity is lower due to reflection losses at the mirror surface, absorption by the protective cover layer and a filling factor of less than 100%. At the same time the *off* state intensity is higher because of reflection by the protection layer and scattering by the edges of the micromirror. The main differences between the intensity patterns generated by a pinhole and a DMD pixel are illustrated in Figure 4.1.

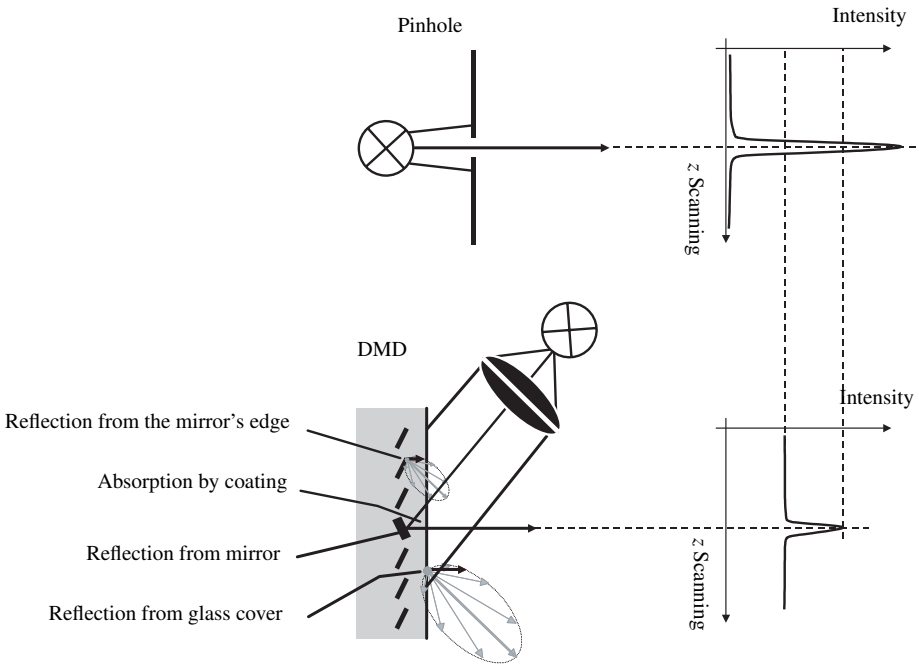

Figure 4.1: Comparison of pinhole vs DMD by means of intensity curves and contrast efficiency

Figure 4.2 shows the set-ups that the experiments were done.

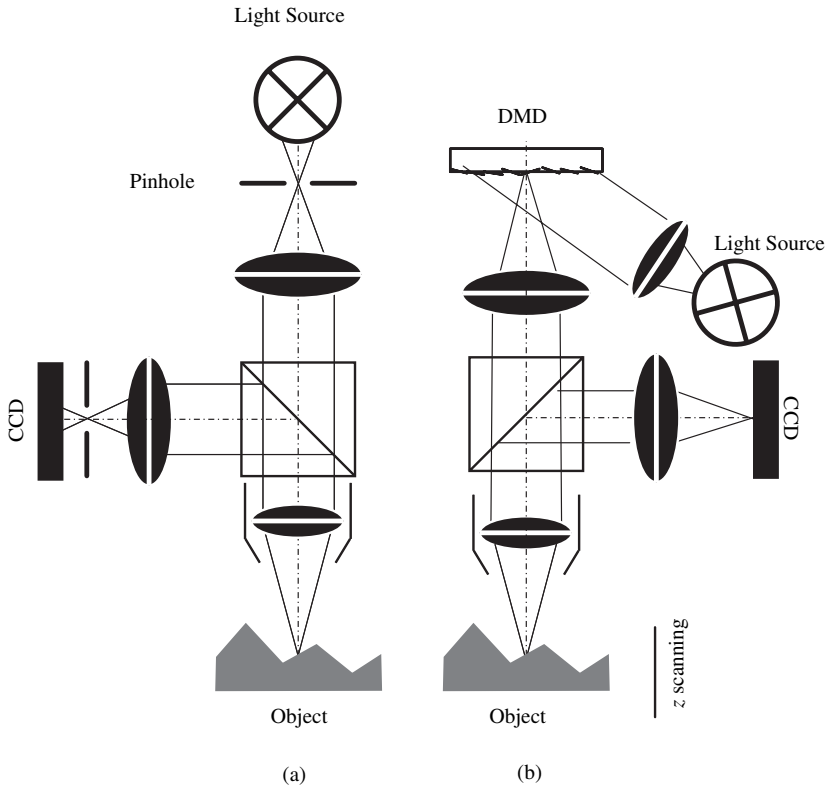

Figure 4.2: Experimental set-ups for comparison of DMD pixel with real pinhole

In Figure 4.2(a) the pinhole is illuminated in transmission, it is placed on the axis of the optical set-up to eliminate as much possible as the disturbing influence of aberrations. In Figure 4.2(b) the DMD is illuminated in reflection, the axial pixel is switched to the *on* state. On the detection side a CCD array and as an object, a plane mirror with interferometric quality was used. In both cases experiments were done with a 20× with 0.46 NA value semi-aprochromate microscope objective. The objective was scanned in the z direction by a piezo-electric actuator [1].

[1] A PIFOC system from Physic Instruments (PI)

In the first experiment the depth response curve was obtained for a 10 μm in diameter pinhole and a single pixel of the DMD. The results are presented in Figure 4.3(a). The experiment was repeated with a pinhole of 100 μm in diameter and a virtual pinhole consisting of 5×5 DMD pixels. With a pixel size of 17×17 μm the areas of both pinholes are about equal. The results of this second experiment are presented in Figure 4.3(b).

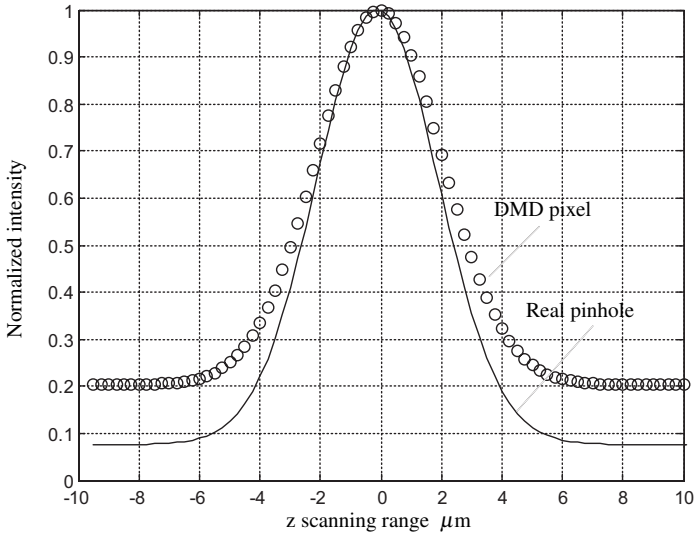

(a) Result of experimental comparison of pinhole vs DMD by the means of intensity curves and contrast efficiency. 1 DMD pixel vs 10 μm hole

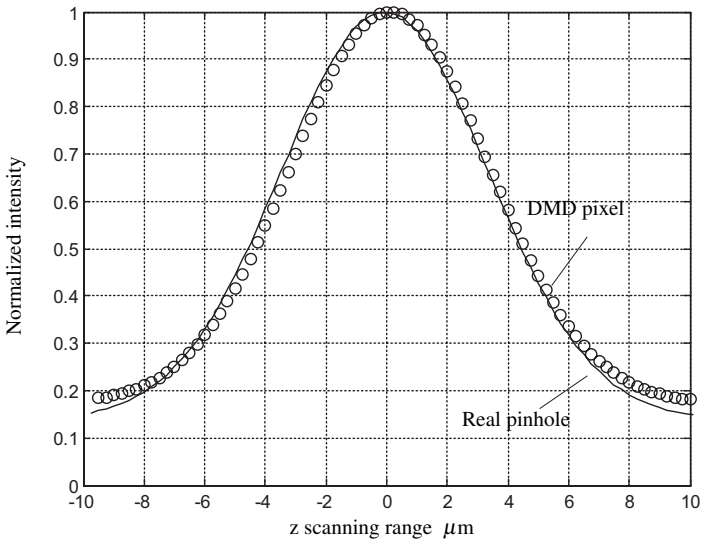

(b) Result of experimental comparison of pinhole vs DMD by the means of intensity curves and contrast efficiency. 5×5 DMD pixel vs 100 μm hole

Figure 4.3: Result of experimental comparison of pinhole vs DMD by the means of intensity curves and contrast efficiency

The intensities in Figure 4.3 are normalized. It is seen in Figure 4.3(a) that the contrast obtained with a real pinhole is better than with a single DMD pixel. The FWHM of both depth response curves in Figure 4.3(a) is about equal to $5\,\mu$m. This is about a factor 2 larger than the prediction of Corle's theory (using $\lambda = 0.55\,\mu$m). The possible causes of this difference in results will be discussed in Section 4.4. In Figure 4.3(b) only a slight difference in contrast is seen. The FWHM has grown to $8\,\mu$m. Although the contrast ratio obtained with the DMD is inferior to that the pinhole, the depth response curves are almost equally useful for depth discrimination. After these two experiments it is concluded that concepts of confocal microscopy can be applied to a system with DMD illumination. The same conclusion can be drawn, *mutatis mutandis*, about the replacement of detection pinholes by a CCD array. We did not do any experiment on this issue, but we are convinced that the result would be in agreement with the result given above.

4.3 A semi-confocal microscope

When the illumination pinhole of Figure 4.2 is replaced by a pinhole array, a semi-confocal microscope is obtained as illustrated in Figure 4.4

In this microscope design $x-y$ scanning is not possible (except by mechanical movement). Without $x-y$ scanning a sampled version of the 3D topography of the sample surface is obtained. It is clear that z scanning is still necessary. The pinhole diameter and pinhole density of the mask can be adapted to the application; a set of pinhole arrays must be available. Such a set of pinhole arrays was produced by the central work shop of Eindhoven University of Technology using etching in an aluminum layer. A few examples are shown in Figure 4.4. Because of the absence of $x-y$ scanning the measurement time of this system is smaller than that of the DMD based microscope. With the DMD based Microscan system it is also possible to omit $x-y$ scanning. Operation of the in this mode will be explained in Section 4.5 and the results of the measurements in Section 4.6. Because the results are identical, the measurement results will not discussed in this section.

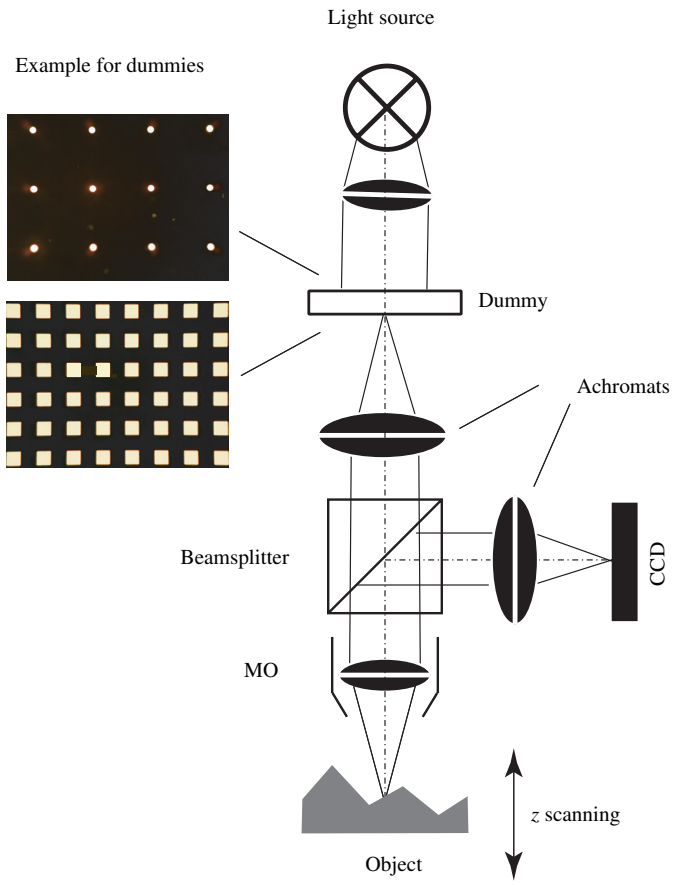

Figure 4.4: Experimental set-up with dummy. Dummies can be realized with pinholes of different size and shapes.

4.4 DMD based experimental set-ups

During the project two different set-ups were built. The first set-up was based entirely on the design that was described in Section 3.3. The lay-out data of this design are given in Table 3.4. The specifications of the key components, DMD, CCD and microscope objective are summarized in Table 3.3. For z scanning a PIFOC piezo-scanner from PI with a range of 100 μm and a minimum step size of 10 μm was used. Figure 4.5 shows the first experimental set-up. Because of its importance the illumination system will be discussed in detail in Section 4.4.1

During the experiments with this set-up it is found that the depth response curves obtained at positions in the outer regions of the field of view were of low quality, compared to the depth response on axis. Characteristics intensity curves for this

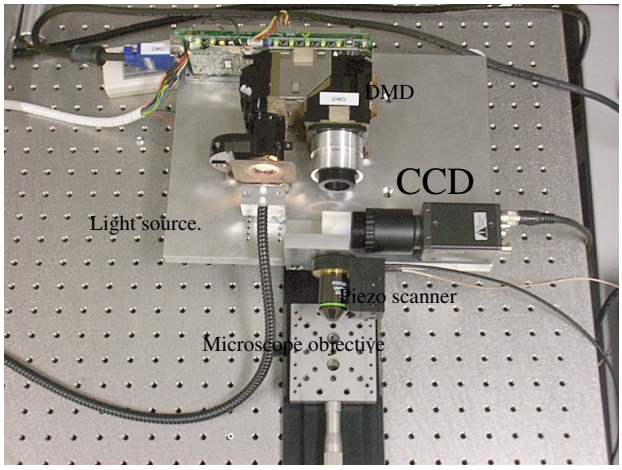

Figure 4.5: The very first build experimental set-up

system are given in Figure 4.6 where the depth response curves were obtained with a 20× with 0.46 NA microscope objective.

Figure 4.6(a) shows the depth response curve for the center DMD pixel. It has a FWHM of about 5.5 μm and it is also a bit asymmetric, where the asymmetry could be caused by spherical aberration, and also by small alignment errors in the developed set-up. Figure 4.6(b) shows the depth response for the outer field point. The maximum intensity is decreased from 230 to 155, arbitrary but identical units and the FWHM has grown to 11.5 μm. Moreover, there is a significant asymmetry of the curve. These effects are mainly caused by field aberrations (coma, astigmatism) over the diffraction limit. The presence of these aberrations was already presented in the spot diagrams in Figures 3.15 and 3.16. A further problem with the first set-up was that it was built in a horizontal plane, as can be seen from Figure 4.5. Although this approach resulted in a good mechanical stability, it makes the sample handling rather difficult. Therefore it is decided to build a second set-up where the main differences with the first one are:

- the set-up is built in a vertical plane, so that the object can be placed and measured in the horizontal plane,
- longer focal distances both on the DMD and the CCD side are chosen.

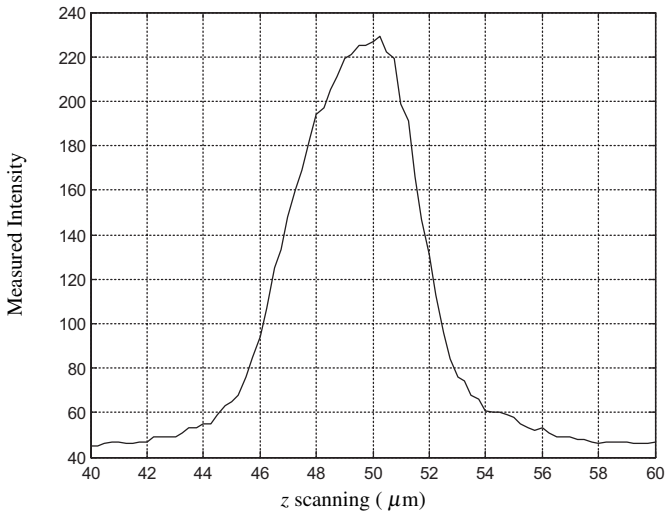

(a) Depth response curve for the center DMD pixel

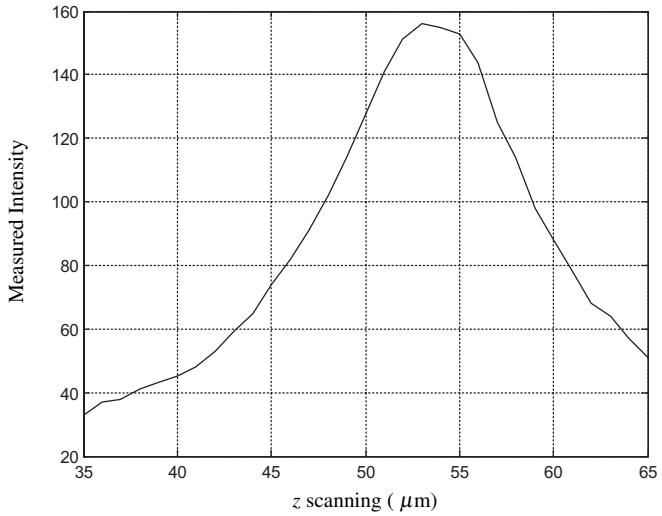

(b) Depth response curve for the outer DMD pixel.

Figure 4.6: Depth response curves of the first experimental set-up

Figure 4.7 shows the second experimental set-up. Longer focal distances have the consequence that the image of the DMD in the field of view of the microscope objective is a factor of 3/4 smaller than in the first design. Therefore, with 20× magnification only 600 μm profiles can be obtained. In a more definitive design the profile length must be restored to 800 μm. This can be done by replacing the existing achromats with air-spaced aplanic doublets or triplets. Because the part of the FoV that is used is smaller now and the field angle of the achromats is also reduced, the effects of the aberrations on the depth response curve are less serious. The set-up is tested by obtaining the depth response curves for the axial and the outermost pixel of the DMD. These proved to be nearly identical.

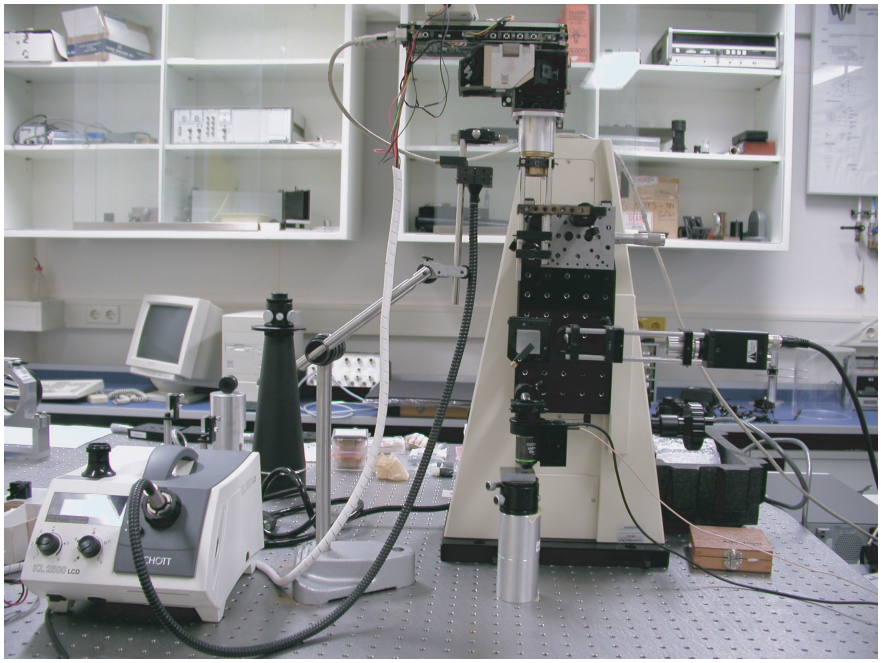

Figure 4.7: 2nd set-up

The depth responses obtained for the outermost DMD pixel by using 20× and 50× microscope objectives are given in Figure 4.8, where the FWHM values are 6.2 μm and 1.5 μm respectively. It should be noted that the prediction of Corle's theory is 2.5 μm for the 20× and 0.43 for the 50× microscope objective.

The differences between the measured and the predicted values are caused by the following phenomena:

- finite illumination and detection pinhole size,
- broadening due to aberrations,
- alignment errors in the set-up.

From the approximate theory that is formerly developed it is shown that a diffraction spot with diameter d_0, broadened by a virtual DMD based pinhole of diameter e, creates a broadening of the spot on the object by a factor b, given approximately by Equation 4.1.

$$b = \sqrt{1 + \frac{e^2}{d_0^2}} \tag{4.1}$$

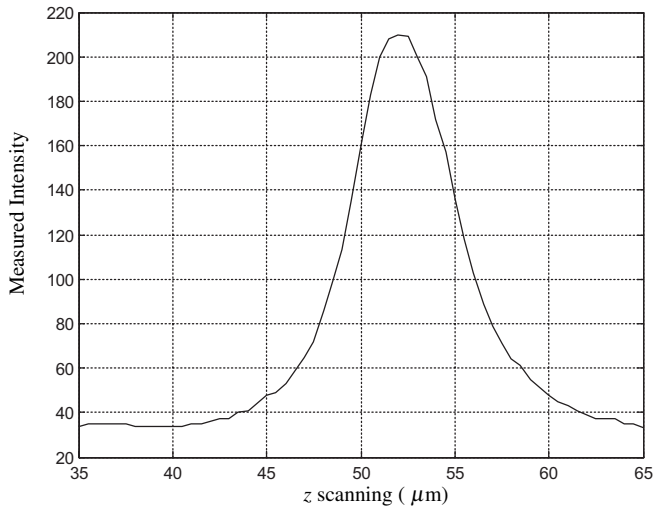

(a) PSF 20 X

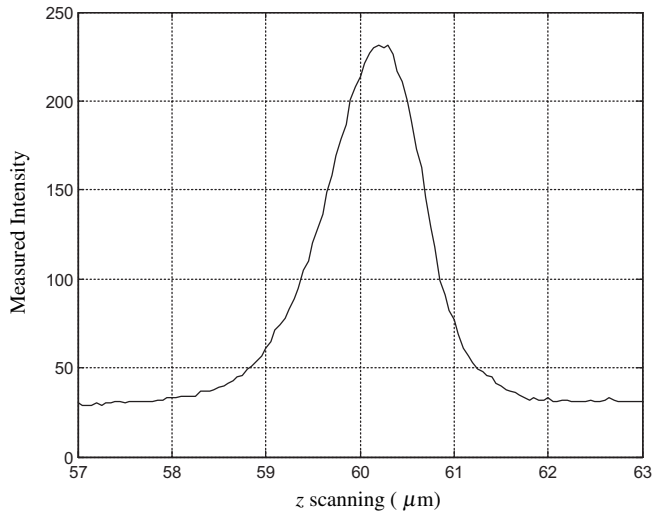

(b) PSF 50 X

Figure 4.8: PSF functions

Measurements mostly are done with a virtual pinhole of 2×2 pixels so that $e = 2\ \mu\text{m}$ on the object with a $20\times$ microscope objective. With $d_0 = 1.5\ \mu\text{m}$, $b = \frac{5}{3}$ so that the broadening caused by the finite pinhole diameter would give a FWHM of $4.2\ \mu\text{m}$. But, it is measured $6.6\ \mu\text{m}$, so this does not give a complete explanation of the measured results. The results of Figure 4.9 are obtained by taking the signal from a single pixel on the CCD, this does not lead to a further broadening of the depth response curve.

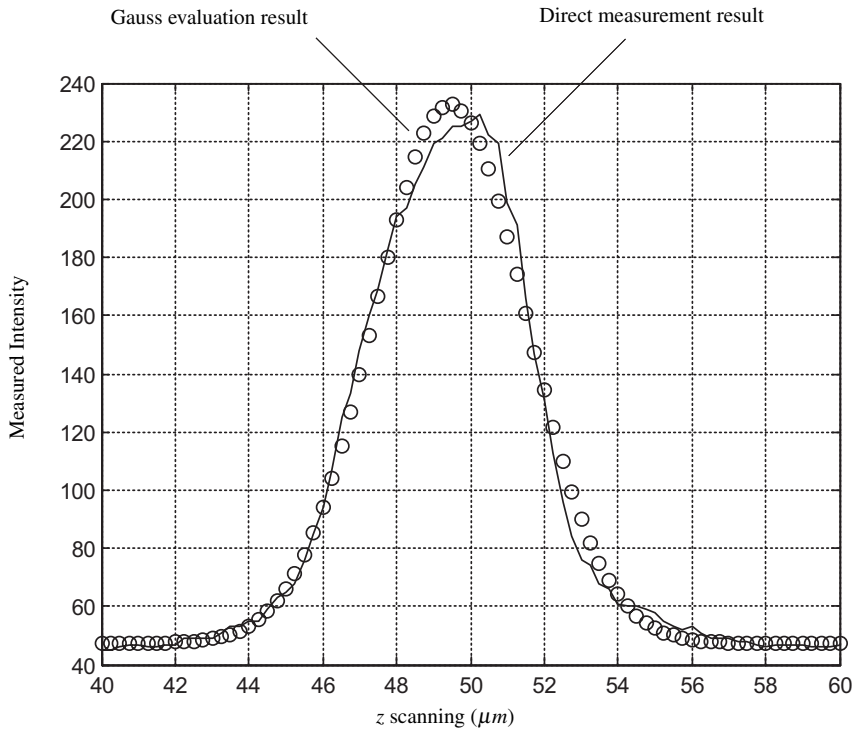

Figure 4.9: Comparison of Gauss evaluation and direct measurement result.

4.4.1 Illumination of the DMD

The light source and the illumination optics are two important components of the developed system. Both were identical in the two set-ups that are developed during the project. For the light source the essential parameters are the spectrum and the effective source geometry. In Section 2.4 the influence of chromatic aberrations on the depth response curves is discussed. It is found that with the imaging optics that are used, this influence is not very strong. Therefore, it is concluded to use a source with a broad spectrum. The influence of the spectral width is tested by inserting a glass transmission filter with a maximum transmission at 550 nm; a small narrowing of the depth response curve is observed. As a result, it is decided to use the Schott 2500 KL, LCD lamp over the whole visible spectrum. In this source the light of an Osram 50 W halogen lamp is projected on a fiber bundle with a diameter of 3 μm. This has the advantage that heat and vibrations can be kept away from the rest of the optical system.

The illumination optics serves to illuminate the DMD homogeneously and to send the light from *on* pixels through the imaging optics to the CCD via the sample. Because of the lay-out chosen for the developed system, that is described in Section 3.3.1 the effective source must be situated in the focal plane of the condensor lens, so that the DMD is illuminated by a bundle of plane waves. This idea is illustrated in Figure 4.10.

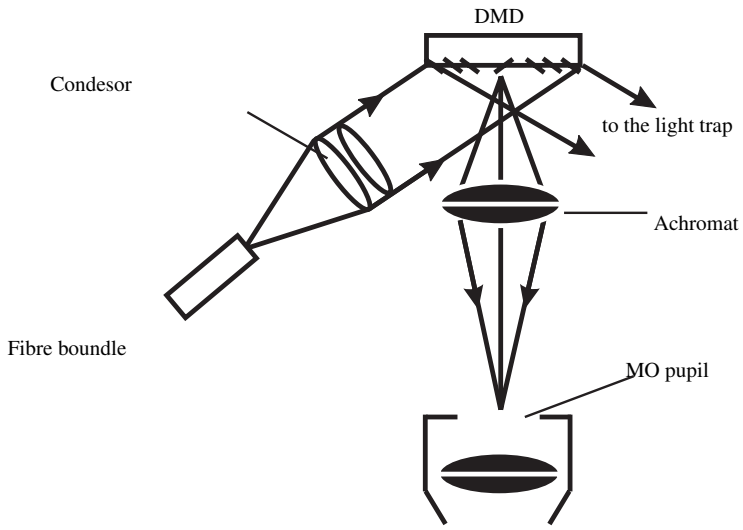

Figure 4.10: Illumination principle of Microscan

The effective source is imaged by the condenser and the first achromat onto the pupil of the microscope objective. For the developed system the DMD is obtained from a 3M projector. This had the additional advantage that the control unit and a part of the illumination optics are easily adapted to Microscan. The adapted illumination optics for the proper DMD illumination is described in detail by Chang and Shieh [82]. They designed a special prism to fold up the light path of the illumination system. The housing of the illumination optics, which has its own light trap and the specially designed prism, is used in the developed system in order to collect the light reflected from the *off* pixels of the DMD and for the proper illumination of the DMD unit. Figure 4.11 shows the prism and the housing that is partly adapted from the original projector.

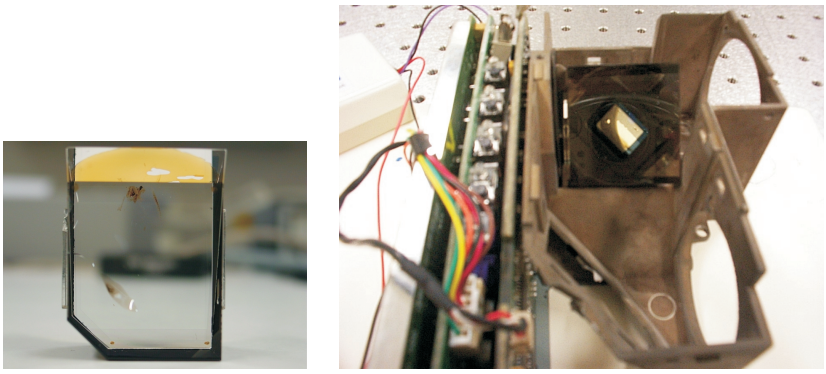

(a) Prism (b) Housing

Figure 4.11: The proper illumination optics for DMD

4.5 Measurement procedure

The flow chart of the measurement procedure is illustrated in Figure 4.12.

The course of the measurements is: first, a specified pattern of DMD super pixels is produced and the CCD image is evaluated at the corresponding regions of interest. Then the DMD super pixels and CCD regions of interest are moved and evaluation is carried out again at different positions on the specimen. These steps are repeated until the surface is completely scanned in x and y direction. Afterwards, the microscope objective or the object is moved in vertical direction and lateral scan restarts. After the depth scan is completed, the interpolated intensity maximum is calculated for each super pixel. The intensity maximum is linked to the piezo-scanner position allowing the $3D$ surface topography to be obtained, see Figure 4.13.

In the following the steps in the measurement procedure will be reviewed in more detail and the possibilities that arise with each step will be discussed.

4.5.1 Virtual pinhole patterns

While creating a periodic virtual pinhole pattern on the DMD the form of the pinhole ($n \times m$) and the period of the pattern $N \times M$ are the essential parameters. During measurements $n \times n$, $m = n$ square pinholes[2] are used, where n is equal to

[2] super pixel

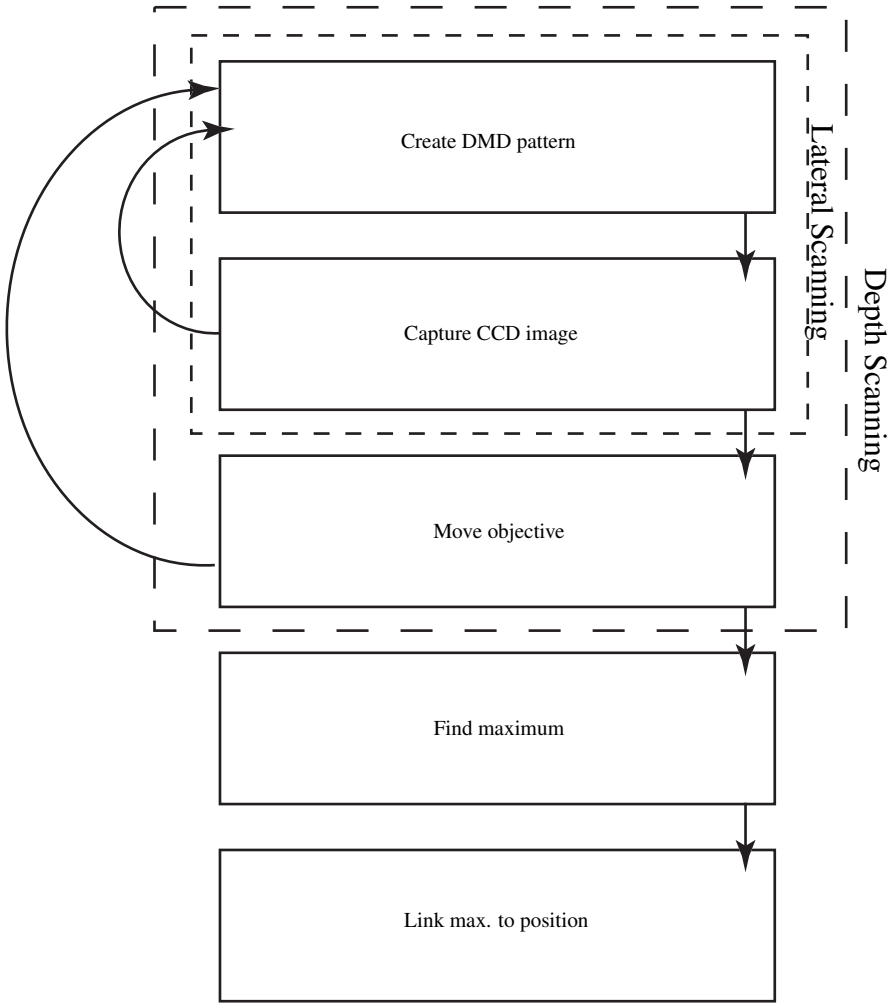

Figure 4.12: Flow chart for scanning

1, 2, 4 and the size of the pixel determines the lateral resolution of the developed system. For the improved system a pixel image on the object has a size of 0.75 μm which was about the half of the theoretical airy disk diameter, which is calculated 1.5 μm for a 20× microscope objective.

For objects that reflect less light the pinhole size can be taken larger naturally at a cost of lateral resolution. This possibility can also be used for local drops in reflected intensity or in other words, for uniform illumination on the detection sensor (CCD) by adjusting each DMD pixel's *on* time which is explained formerly in Section 3.2.1. Although the scanning matrix size N can be chosen as $2n$ as long as the height variations are smaller than the depth of focus of the objective (about 2.5 μm for 20×, 0.46 NA microscope objective) during the measurements

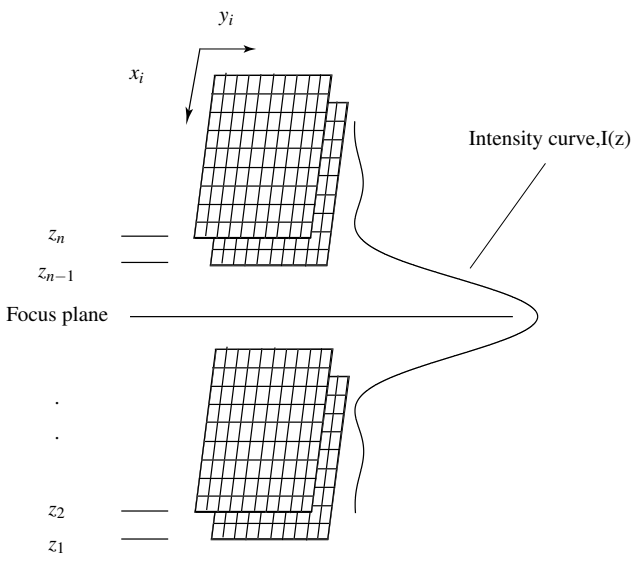

Figure 4.13: Idea of the confocal image forming

it is chosen $N = 10$ and $N = 20$ which is actually equal to $5 \times n$ and $10 \times n$. Figure 4.14(a) illustrates the idea of creating a super pixel and the scanning of the DMD and Figure 4.14(b) shows the DMD based real pinholes created during a measurement.

4.5.2 Matching between the DMD and the CCD

In order to create the virtual detection pinholes on the CCD it is necessary to establish a matching between the DMD and the CCD. A DMD pixel D_1 with the coordinates (x_{d1}, y_{d1}) is imaged on a CCD pixel C_1 with the coordinates (x_{c1}, y_{c1}). This procedure is repeated for the three other DMD pixels where the DMD pixels are entered by the user and related CCD pixels, imaged points, are determined, see Figure 4.15.

As a result, matching between the DMD and the CCD is obtained for each DMD pixel which is imaged on the CCD. If there is any not imaged DMD pixel(s), this pixel(s) will not be taken into account during the data analysis. When the x, y axes of the DMD and the CCD are well aligned and distortion is neglected, the matching between two sets of coordinates can simply be written as

$$\left[\ X_{DMD} + i\ Y_{DMD}\ \right] \cdot \left[\ a + i\ b\ \right] + \left[\ c + i\ d\ \right] = \left[\ X_{CCD} + i\ Y_{CCD}\ \right] \tag{4.2}$$

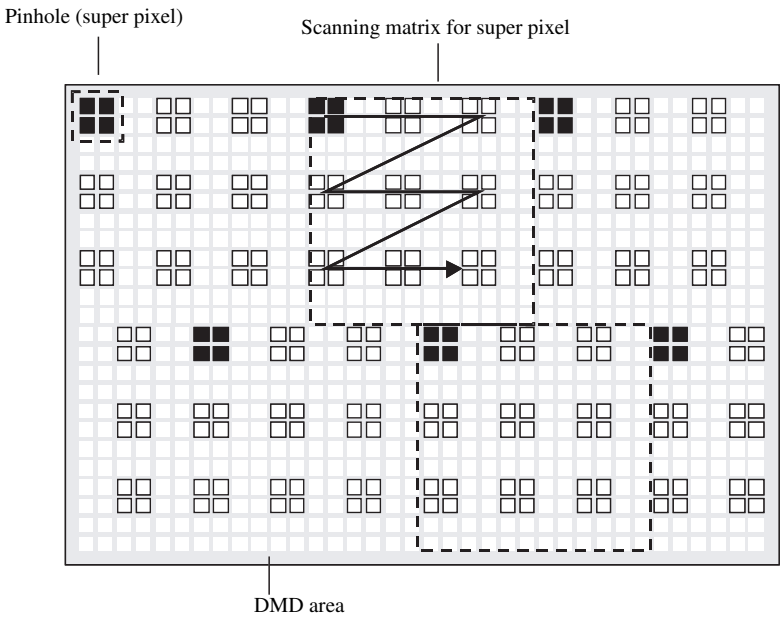

(a) DMD based spot creation

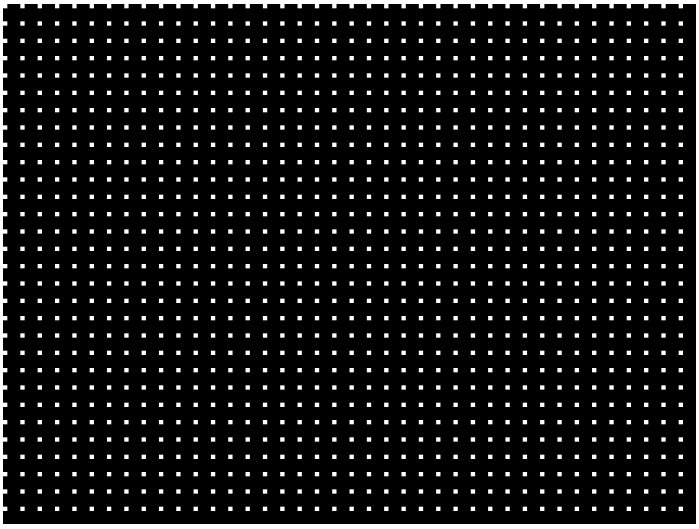

(b) DMD based pinholes, which are created during a measurement

Figure 4.14: Real output for DMD scanning

where $\left[\ a+i\ b\ \right]$

is for rotating and scaling and $\left[\ c+i\ d\ \right]$

is for transpose Consequently for full DMD to CCD matching can be described by the following equation.

$$\begin{bmatrix} x_{d1}+i\ y_{d1} & 1 \\ x_{d2}+i\ y_{d2} & 1 \\ x_{d3}+i\ y_{d3} & 1 \\ x_{d4}+i\ y_{d4} & 1 \end{bmatrix} \cdot \begin{bmatrix} a+i\ b \\ c+i\ d \end{bmatrix} = \begin{bmatrix} x_{c1}+i\ y_{c1} \\ x_{c2}+i\ y_{c2} \\ x_{c3}+i\ y_{c3} \\ x_{c4}+i\ y_{c4} \end{bmatrix} \tag{4.3}$$

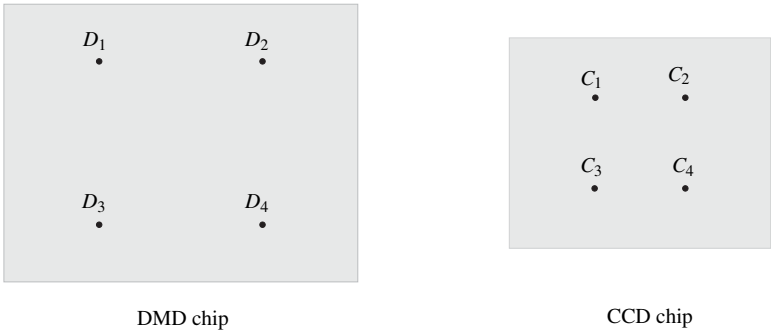

Figure 4.15: Realization of the matching between the DMD and the CCD chip

The coefficients a, b, c, d are depended on both achromats on the CCD and on the DMD side. Actually these are the functions of the system and it is not necessary to focus these coefficients in details, because in a well aligned system lateral magnifications are mostly the same and equal to one. For each imaging condition they can be calculated just after a simple matching test. Because the DMD pixels are manually entered by the user and the detected CCD pixels are the results, the transfer function between these two components, the coefficients, can be obtained by reverse calculation. Matching application between the DMD and the CCD is done (normally) with the help of the mirror object. This procedure creates perfect matching conditions but it is also possible that the matching conditions can be realized on the object that will be measured. In that case the problem that is caused by extreme scatter or wavy surfaces can be reduced to a minimum. If this is the case, it can be said that the developed system introduces not only *virtual pinholes* but also *adaptive pinholes* application. After an imaged CCD pixel is found the imaging pinhole is created by turning neighboring pixels *on*. The size and the shape of the pinhole are again determined by the user. The depth response value is obtained by recording the summed signal from the region of interest. In order not to degrade the lateral resolution too much the size of the region of interest (virtual pinhole, roi) should be taken equal to or smaller than the spot on the CCD. During the experiments usually the size of the roi was taken just bigger than the super pixel, for example for a 2×2 super pixel the roi is chosen as 4×4 CCD pixels. Figure 4.16 shows the illumination and detection pinholes during the measurement. As it can be seen from the Figure that the

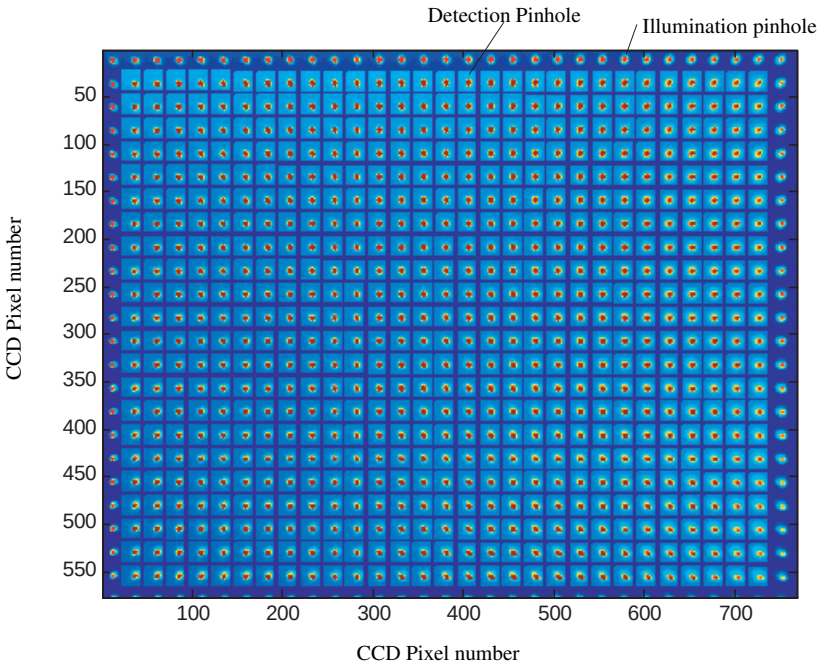

Figure 4.16: The DMD and the CCD matching during a measurement

bright spots are the imaged DMD pixel(s) on the CCD and the gray areas are the related detection pinholes created on the CCD. On the CCD edge although there are imaged DMD pixels to avoid the problems no CCD pixels were created. This safety zone can also be easily canceled or can be increased.

4.5.3 Lateral scanning

The importance of lateral scanning for measurements is that the number of the spots on the object basically determines the scanning time for whole measurement. The higher the number of the spots the lower the measurement time. With a super pixel of $n \times n$ pixels and a scanning matrix of $N \times N$ pixels a number of images of at least N^2/n^2 has to be obtained at each z level. The idea of scanning is illustrated in Figure 4.17.

With $n = N$ the microscope would function as a conventional bright field system, without the possibility of depth discrimination. Usually the DMD pattern is moved in steps equal to the size of a super pixel. With objects that have a complicated surface structure smaller steps of 1 pixel is taken. When the

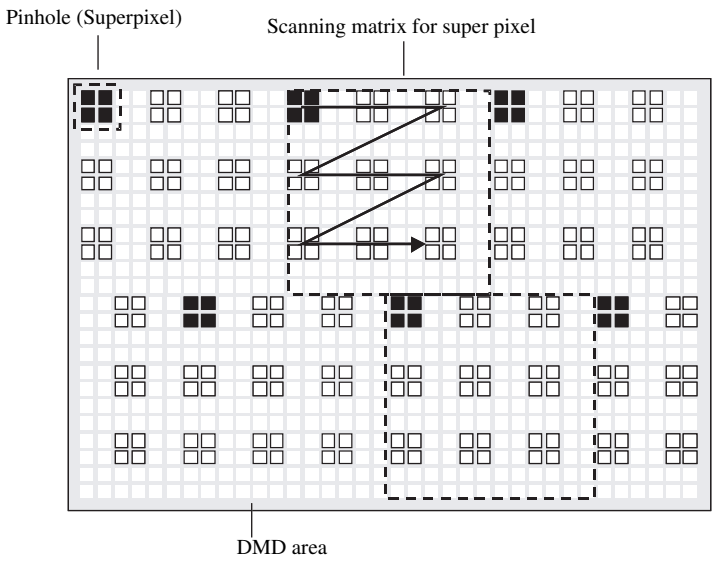

Figure 4.17: Lateral scanning idea

measurement time becomes more important than the lateral resolution, similar to semi-confocal idea described in Section 4.3 or similar the confocal microscope with microlens array described by Jordan [48] can be applied for measurements. In Section 4.6 some measurement results will be presented related with the semi-confocal microscope idea. Although it was not realized experimentally, by taking a super pixel as a line, consisting of one or more columns (line scanning), a shorter scanning time can be achieved. But is clear that the depth discrimination will be much worser than with the virtual pinhole application.

The N^2/n^2 images captured during lateral scanning must be stored for lateral use. By clipping these images for each roi the intensity profile is obtained. An other option to evaluate the captured images is used by Bitte [53] by obtaining the average intensity profile for each z level, the so called *source image* which is actually the idea of image processing in commercial devices. For each z level with the help of only one source image a 3D topography can be obtained [48]. The developed system's imaging approach is as follows. After the correspondence between the DMD pixels and the CCD pixels has been determined, an array of pinholes with a specified shape and size is produced on the DMD. According to the surface geometry at the image location, the intensity of the reflected signal

is recorded to the corresponding CCD pixel. Figure 4.18 shows the procedure for the example of a tilted object.

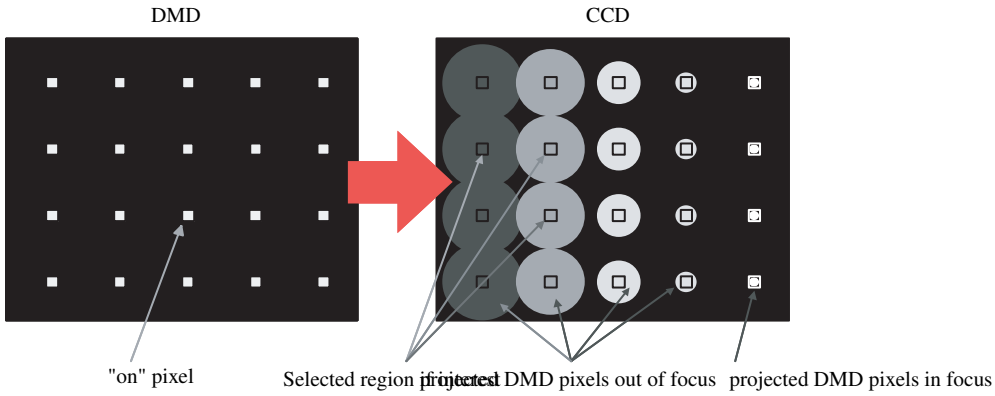

Figure 4.18: Measurement principle on a tilted object

The intensity in each considered CCD pixel depends on the displacement of the object surface from the confocal plane according to the depth response curve. Hence, by measuring the different intensities of all considered pixels on the CCD chip and finding its maximum while the specimen is moved through the confocal plane, information about the height profile of the object surface can be obtained. On the left side of Figure 4.18, pinhole patterns created on the DMD are illustrated and on the left side, the CCD images with roi are illustrated for the case that the object is tilted about the vertical axis. When the object is in focus the spots imaged on the CCD are small and imaged in the roi of the CCD but when the object is out of focus the spots are blurred and the spot diameter is getting bigger and the detected intensity becomes lower.

4.5.4 Axial scanning

In principle, z scanning can be done in different ways: by moving the microscope, the microscope objective or the object. In the developed set-up the microscope is mounted on a vertical slide (z tower) and the slide is used to bring the sample in rough focus. The fine z scanning is done with the help of a piezo-electric scanner (PIFOC) which is connected to the microscope objectives. The z scanner could make a step of minimum $10\,\mu\text{m}$ and each step takes $10\,\text{ms}$. Steps within the depth of focus and a stepping time of t_z seconds, and with N^2/n^2 positions in the

lateral scanning with a frame time of t_f the total scanning time is given by

$$T = z_n(t_z + \frac{N^2 \cdot t_f}{n^2}) \tag{4.4}$$

With $z_n = 10$ and $t_z = 10\,\text{ms}$, $100\,\text{ms}$ is needed for vertical scanning. The electronics that is used from the 3M projector has the capability to refresh the frame in $16\,\text{ms}$. For $N^2/n^2 = 100$ the lateral scanning time for each z level is $1600\,\text{ms}$ and the total scanning time is $16000\,\text{ms}$. By choosing a smaller scanning matrix $N^2/n^2 = 4$ the lateral scanning time can be reduced up to $640\,\text{ms}$. From this calculation it can be seen that the lateral scanning makes the largest contribution to the total scanning time. By using special control electronics [27] the frame time can be reduced to $0.1\,\text{ms}$. The lateral scanning time can then be reduced with a factor of 160; in this option the z scanner becomes critical and determiner of the measurement time.

4.5.5 Surface topography determination

From the images stored during both during lateral and vertical scanning, the surface topography can be determined. From the intensity curves that are obtained for each super pixel in the z scanning range the position information can be obtained in different ways. A few methods were considered during the software development.

- Gauss fit,
- Parabola fit,
- Adaptive curve fit,
- Direct maximum determination (without any fitting procedure).

Taking the highest measurement value (direct maximum determination) is clearly the fastest method; its axial measurement accuracy is limited by the z scanning step to about $\pm 10\,\mu\text{m}$. When a better accuracy is needed parabolic curve fitting was used in the center of the depth response curve. Although the Gaussian curve fitting method introduces a significant improvement in comparison with direct maximum determination because of its' iterative calculation method, it takes a

lot of time to create a 3D image of the scan specimen. Dependent on the signal to noise ratio the accuracy of the measurement can be a factor $2-3$ times better. This is also true for the center of gravity method which is used only in theoretical considerations in Section 2.5.

4.5.6 Software

Although software development was not one of the targets of this dissertation, to overcome the difficulties in the EU project it was decided to build an independent home made software. This software was realized with the significant contribution of two Ph.D. candidates at Precision Engineering, ir. M. Jansen and ir. M. Morel. Figure 4.19 illustrates the flow chart of the developed measurement software. The

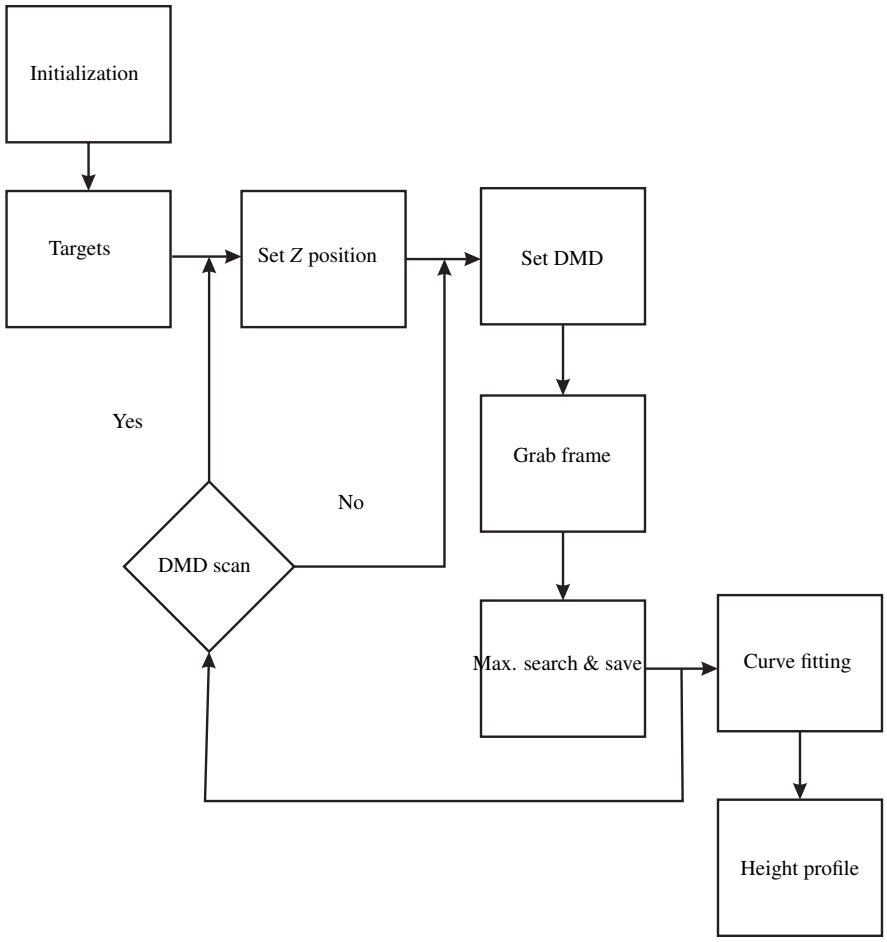

Figure 4.19: Measurement flow-chart

actions taken during the measurements are as follows:

Initialization: The system components are initialized and also the system parameters are entered. Super pixel size, scanning matrix size on the DMD are chosen, the scanning range is determined. Also the detection pinholes and roi are created on the CCD.

Targets: the scanning range and step are manually entered.

Set z level: after finishing the lateral scanning (x,y scanning on the DMD) the system moves in the z direction with the predefined step.

Set DMD: in order to make a full x,y scanning this procedure shifts the DMD patterns.

Grab frame: do the capturing for each super pixel after each lateral scanning, this procedure is repeated for each vertical z level.

Max. search & Save: is done after each capture command, actually this step is done for the security of the measurements. This step can be skipped or the captured image can easily be stored in a dynamic memory for future application. Basically, this step is the bottle neck of the developed system, but in the given technology conditions this is the only way to avoid a hardware crash problem.

DMD scan: is repeated until the vertical and the lateral scanning is completed.

Vertical movement: is repeated after each lateral scanning is completed and if there is another z level to scan.

Curve fitting: this is the critical part of the software. Using the stored CCD images for each super pixel and for all z levels, the maximum intensity value can be found. For this calculation alternative solutions are available such as direct determination, Gauss fitting, parabola fitting, similarity evaluation. During the curve fitting applications the intensity curves, that have insufficient quality, are omitted in the process.

Height profile: is created with the help of z information obtained from the maximum intensity determination during the measurement.

Because the developed software is designed to save each captured image, the average measurement time is approximately 10 min. but, as it is discussed in Section 4.5.4 the system has the capability of much faster scanning and

measurements. The developed software is capable to display the surface topography, either in a false color display or in a pseudo-3D display. Also 2D profiles can be extracted and surface parameters can be evaluated.

4.6 Verification measurements

In order to demonstrate the capabilities of the developed system some quantitative measurements of various samples are performed. These samples are selected in order to obtain the characteristic behavior of the developed system, such as lateral magnification (also known as optical gearing effect), lateral and vertical resolution, comparison with mechanical stylus instruments and to determine the practical limits of the developed system. For these verifications the following samples are used:

- Sine standard, for lateral magnification verification,
- Depth standard (step gauge) for vertical axis (z optical axis) verification,
- Groove standard,
- Roughness standard, to demonstrate the power of the developed system,
- Vicker indent,
- AFM standard, to show the matching between the theoretical and the practical confirmation.

Sine standard In order to determine the lateral magnification coefficients both in x and y direction, measurements with the laboratory sine standard, where the wavelength value is calibrated as 100 μm with mechanical stylus instruments, are done . The measurement is repeated in both perpendicular axis (x,y) by turning the standard 90°. Direct measurement result (without any data manipulation) of the system are given in Figure 4.20.

Measurements were done by using 2×2 pixels as super pixel size and with two pixels lateral step size. The roi on the CCD ware chosen as 4×4 pixels. The measurements are done with a 20× with 0.46 NA value microscope objective,

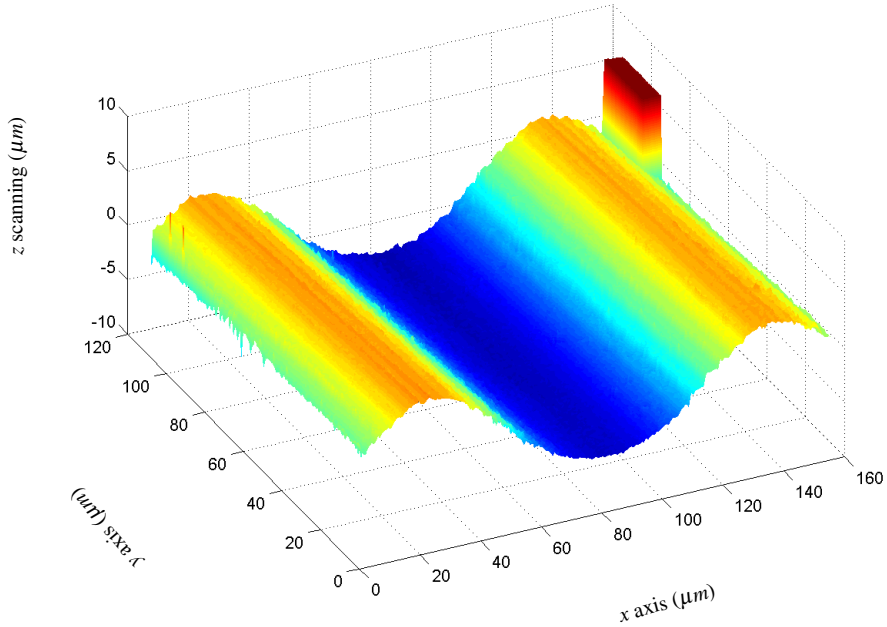

Figure 4.20: Measurement result of Sine standard

and the magnifications from the DMD to the object and from the object to the CCD is verified as 22.2× and 11.1×, respectively. The wavelength of the sine is measured as 100 μm and no differences in magnification are found between different orientations of the standard. That means that anamorphosis, a possible consequence of system misalignment, is not found.

In the profiles shown in Figure 4.21 some deviations from the sinusoidal form are visible. Repetition of the measurement resulted in the production of these deviations, so that these can not be attributed to noise. The stylus measurement of this standard resulted in $r_q = 3.15$ μm; with the developed system, which is an image forming system, the value was measured as $s_q = 3.17$ μm.

Step gauge standard In order to determine the vertical (depth) scanning calibration, the system was tested with a step gauge, that is the combination of two gauge blocks which have different heights. The measurement is done by using a 50× magnification microscope objective and the scanning is realized by 2×2 pixels as super pixel size and with the step of 2 pixels. The result of the

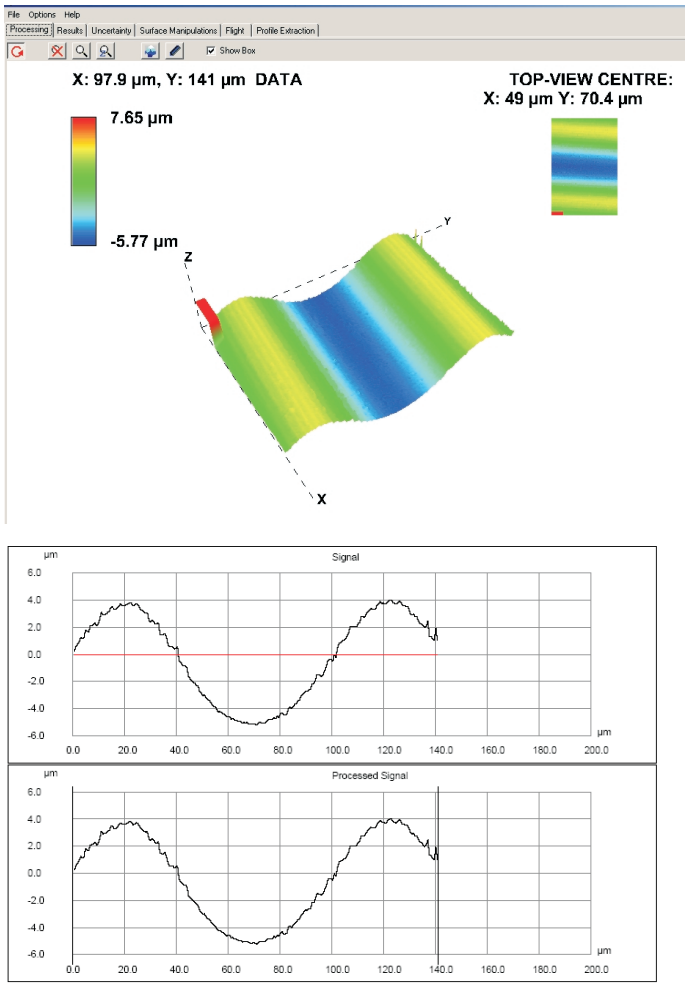

Figure 4.21: Measurement results of Sine standard

measurement is given in Figure 4.22. The step gauge standard is measured as 1.996 μm, see Figure 4.23, where the step gauge formerly calibrated by a stylus instrument as 2 μm.

Groove standard (glass) The groove measurement is carried out on a glass U groove and a metal V groove. The glass U groove consisted of smooth planes inside and outside the groove. The groove depth is given with a calibration certificate as 8.6 μm and it is measured with the developed system as 8.66 μm, see Figure 4.24 and Figure 4.25.

The edges of the groove are rather steep and it is well known that the edge response characteristic of optical systems are usually poor. This leads to the forming of artifacts in the measurement results. This effect can be easily seen

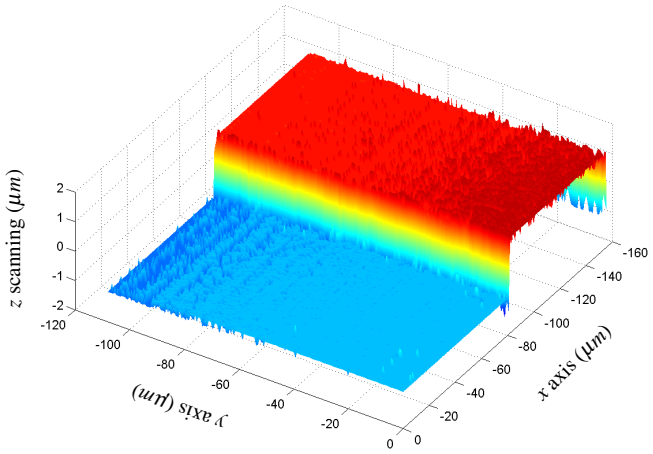

Figure 4.22: Measurement result of depth standard

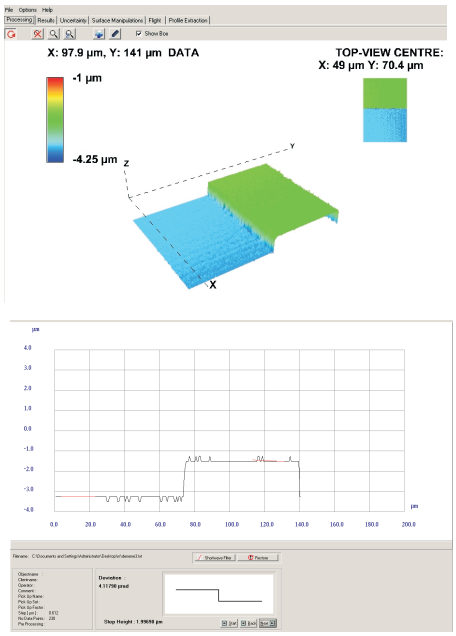

Figure 4.23: Evaluation of depth measurement result

from the Figures 4.24 and 4.25. Because there is not any detected intensity information from the curved edges, at these points the intensity is dropped to zero.

The measurement result on a metal V groove standard is shown in Figure 4.26. The actual waviness in the V groove is also detected during the measurement.

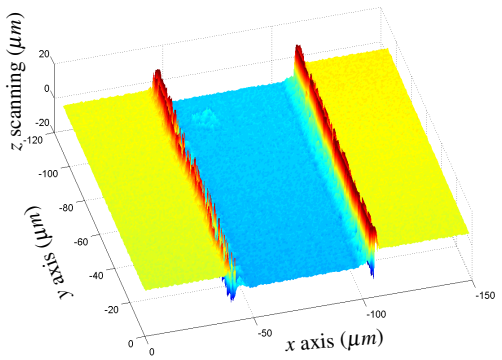

Figure 4.24: Measurement result of glass U groove standard

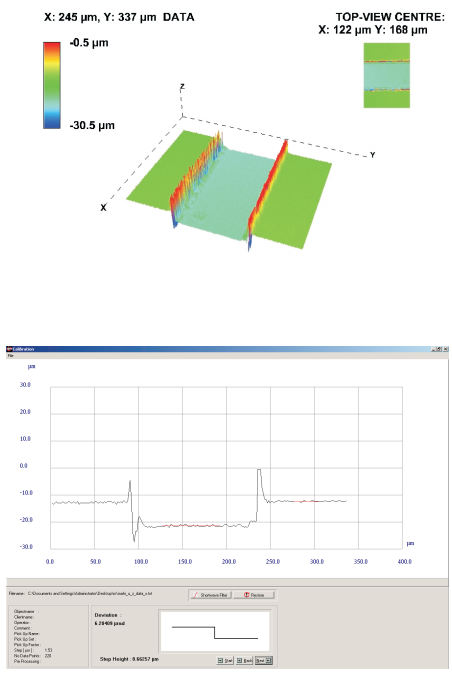

Figure 4.25: Cross-section of glass U groove standard

Some edge response effects, also known as overshoot, can be seen in this measurement too, see Figure 4.27.

Figure 4.27 shows the evaluation of the measurement.

Roughness standard The measurement of roughness is an essential part and the most difficult task in surface characterization. For this reason detailed measurements on laboratory roughness standard were done. The standard that

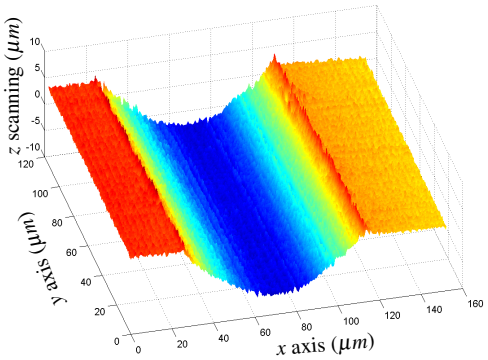

Figure 4.26: Measurement result of a metal V groove standard

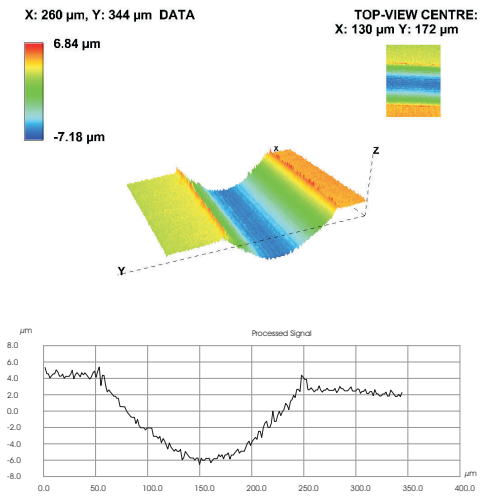

Figure 4.27: Evaluation of the metal groove standard

used during the measurements is calibrated by PTB [3] *Physikalisch Technische Bundesanstalt*, the sample is periodic and one-dimensionally rough, which means that the surface profile varies only in one direction. The standard shows periods of different roughness, with $s_{qmin} = 0.14\ \mu$m and $s_{qmax} = 0.23\ \mu$m. For both parts on the standard a highly detailed topographic measurement has been performed by using 100× magnification with NA value of 0.95. The 3D presentation of this measurement is shown in Figure 4.28.

The PTB standard allows the analysis of the axial and lateral resolution and the accuracy of profilometer systems. It can also be used to analyse the capability

[3] PTB is the primary metrology institute of Germany.

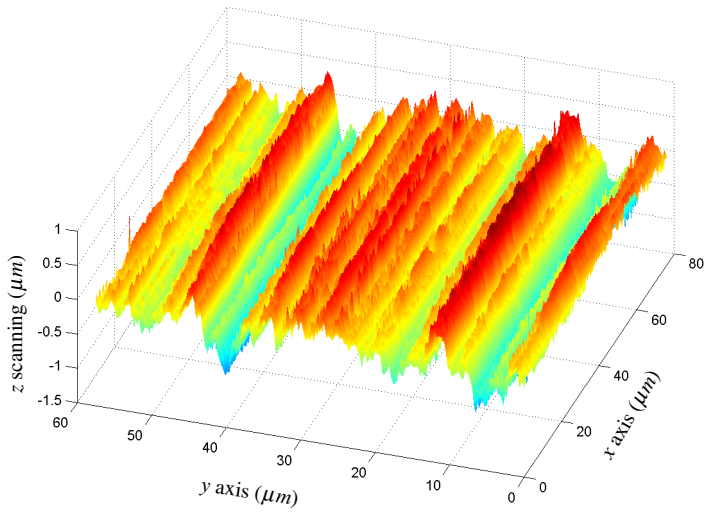

Figure 4.28: Measurement on a PTB-Halle roughness standard

of optical topometers to reproduce varying local surfaces slopes. This is an important item in the comparison of optical systems with tactile (mechanical stylus) systems for surface characterization. Tactile measurements have been carried out for comparison after the Microscan measurements were completed. These tactile measurements were carried out at TU/e Precision Engineering laboratory by using a mechanical stylus instrument with a tip radius of 2 μm.A display of the cross-section measurement result is given in Figure 4.29.

A comparison of the results of both series of measurements is given in Table 4.1.

Table 4.1: Comparison of mechanical stylus and Microscan. The results are the averages of the six repeated measurements.

	S_a		S_q	
	Rough	fine	Rough	fine
optical	0.197	0.118	0.232	0.139
stylus	0.193	0.118	0.225	0.140

In conclusion, the comparability of tactile and optical profilometry has been greatly obtained.

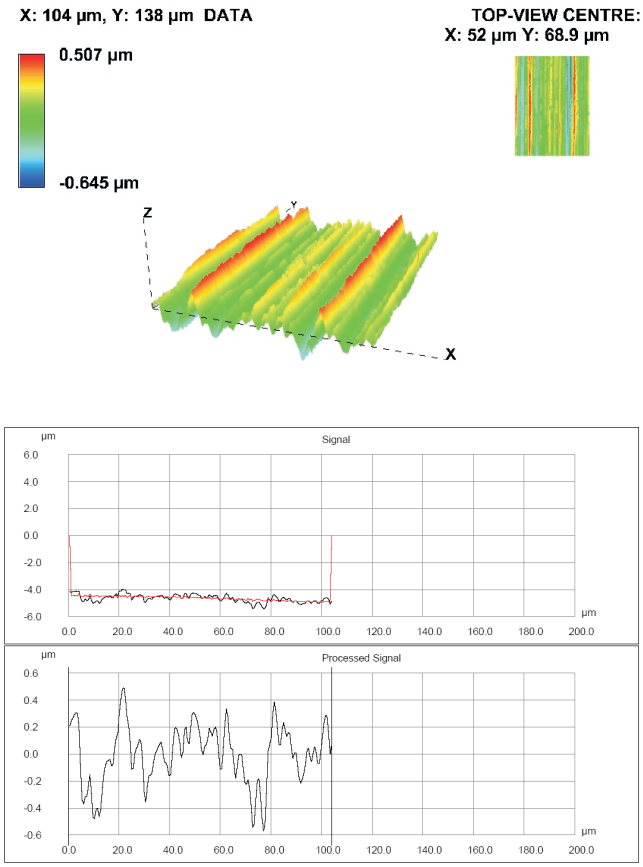

Figure 4.29: Evaluation of the roughness measurement result

Vicker's indent measurement For a Vicker's microhardness measurement a diamond pyramid tip is pressed into a specimen with a defined force. The depth and the diameter of the dent are functions of the hardness of the material. Figure 4.30 shows the 3D result of such a Vicker's indent measurement.

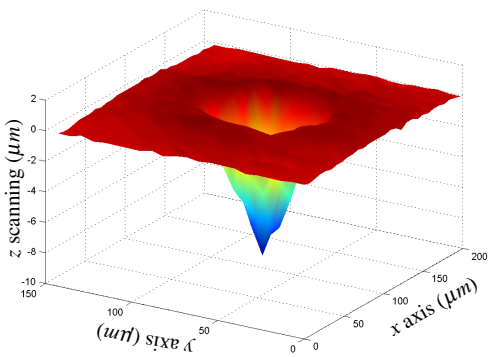

Figure 4.30: Measurement on a Vicker's indent

The measurement has been done with a 50× magnification with a NA= 0.95 value microscope objective. The depth of the dent is of the order of 9 μm. The dimensions of a typical Vicker's indent, 22° cone angle and 136° aperture angle, can easily be imaged with the developed system. The evaluation of the measurement is given in Figure 4.31.

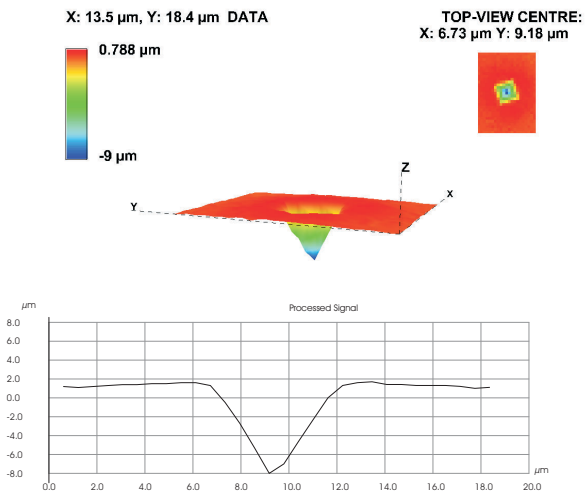

Figure 4.31: Evaluation of the measurement on a Vicker's indent

With the help of Microscan measurements not only the quantitative information but also the qualitative information can be obtained, such as material deformations during the indent process, which is quite important for the nanoscale indent applications.

AFM standard measurement This sample is a twodimensional grating with a period of 3 μm and it was used to check the lateral resolution of the developed system. The measurement result in Figure 4.32 shows the achieved limit of the developed system's lateral resolution.

The amplitude of the structures can not be determined accurately, see Figure 4.33. When a 20× microscope objective with 0.46 NA value is used, the Airy diameter is about equal to 1.5 μm, i.e. half of the grating period.

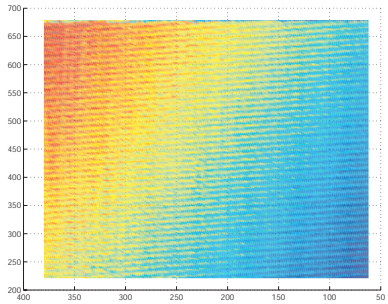

Figure 4.32: Measurement result of an AFM standard

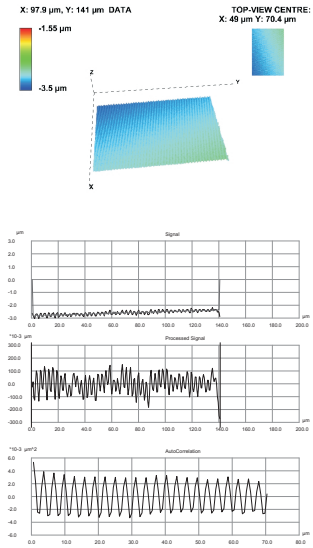

Figure 4.33: Evaluation of the AFM measurement data

4.6.1 Measurement without lateral scanning

For the samples for which lateral resolution is not an important issue, the topography measurement can be executed without lateral scanning. it can be easily realized just by skipping the lateral x, y scanning of the DMD unit in the measurement procedure. This approach shortens the measurement time considerably. With this procedure a sampled 3D topography is obtained. With the 10×10 pixels scanning matrix that was typically used in the experiments, the number of samples 4800 can be obtained on the object with 7.2 μm space between the object level. This mode of operation is identical to that of the semi-confocal microscope that is described in Section 4.3. Figure 4.34 shows a U groove measurement sampled without lateral scanning.

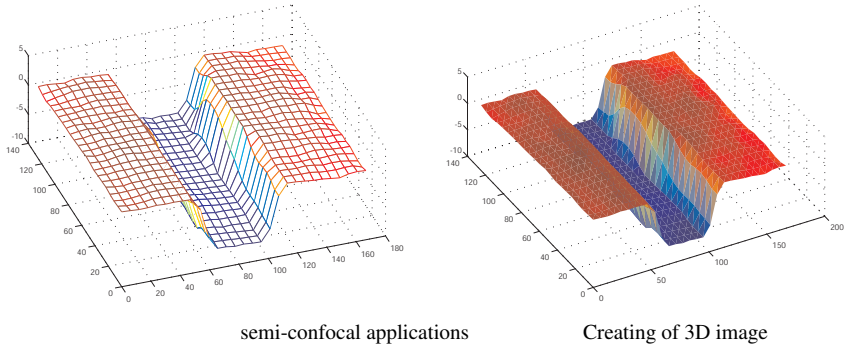

Figure 4.34: Semi-confocal measurement result of depth standard

4.7 Summary

From the measurement results discussed in the former sections, it can be concluded that the Microscan system in its present state can be used for the measurement of *form*, *waviness* and *roughness*. The axial resolution of the current set-up is estimated at 20 nm. The lateral resolution is better than 1.5 μm at a numerical aperture of 0.46. Slope angles more than 20° can be detected by the developed system. However, steep edges give rise to optical artifacts. By omitting the lateral scanning the measurement can be done in 20 sec.; a sampled topography is then obtained. The sampling frequency on the object can easily be adjusted by the matrix size on the DMD. A similar system has been described in Jordan's thesis [48], that uses a microlens array with the sampling distance on the object of 150 μm. It is clear that by the use of an improved mechanical construction the performance of the developed system will be improved significantly.

5. CONCLUSIONS and FUTURE WORK

5.1 Conclusions

The subject of optical microscopy is an extremely rich and diverse field and confocal microscopy is just one of its sub-groupes. The confocal imaging system shows great promise as a tool for range sensing, biomedical imaging, integrated circuit technology, precision engineering and metrology applications. Its main advantages over the ordinary imaging systems are its depth discrimination capability and also the improvement in transverse resolution, by about 30%. The depth discrimination capability allows the confocal imaging system to obtain 3D structures while the improvement in the axial and the transverse resolution permits it to image structures with more detail. This depth discrimination capability makes CSOMs valuable tool for both biology and engineering applications. The development of RSOM and its subsequent commercialization have made CSOM technology available to a wide range of researchers. The variety in techniques reflects the variety and diversity of samples.

This thesis has focused on the design and implementation of a new confocal imaging system and its engineering applications. A micromirror based confocal microscope (virtual pinhole application) has been introduced. Some applications of Microscan on engineering surfaces have also been presented. The details of the optical and mechanical design and the construction of a micromirror based confocal microscope have been discussed. A digital micromirror device as a lateral scanning device is used in the new developed confocal system. The DMD unit is used as a replacement of pinholes, raster scanning unit or scanning mirror of the existing confocal scanning devices. The system can be used not only as a confocal profiler with thousands pinholes but also with the lateral scanning option it can also be used as scanning confocal microscope. A CCD camera is used as detection pinhole in the developed system, where the direct intensity data were measured

and later used for the 3D surface mapping evaluation. During the measurements 600 μm FoV diameter for 20× magnification and 200 μm FoV diameter for 50× magnification with 20 nm axial resolution were achieved and it is concluded that with the improvement of the experimental set-up (with better illumination and better construction) even 10 nm can easily be achieved.

The strength of the system is its flexibility and potential improvement in the measurement speed. With the help of a fully computer controlled DMD unit and by adjusting the DMD pixel's, *on* and *off* time with the help of PWM specification of DMD units local illumination can be achieved. With the help of a local illumination it is possible to create an adaptive illumination on the object level in other words, an uniform illumination detection on the CCD side.

The main advantages of the developed system are:

- the pinhole size and the pinhole shape can be adjusted by the user,
- by controlling the each DMD mirror adaptive illumination on the object can be obtained,
- because of the optical design, stray light and false reflection problems are minimized,
- absence of rotating or tilting devices reduces the vibration problem in the developed system,
- the size and the weight of the DMD unit makes it possible to design a more compact microscope,
- with the help of an adequate control unit the measurement time can be reduced to msec. level,
- with the developing MEMS technology it is possible to develop and produce a cheaper system.

Finally the newly developed DMD based confocal microscope can be considered as the next generation optical measurement system because of its flexibility, robustness, smaller size and lower price.

In addition to the novel "virtual pinhole" implementation the following results are achieved.

In Chapter 2 the depth response and the lateral resolution of the developed system are examined. A new theory, which differs from former studies of Corle [4], Xiao [62] and Jordan [73], for the depth response curves is derived. The effect of aberrations on the depth response curves is examined. The important derived equations in this chapter are proved by the measurement in Chapter 4

In Chapter 3 the optical design of the developed system is introduced. First, it is focused on the geometrical basic matching in order to use all components efficiently. Second, after the aberrations problems occurred, because of the short focal distances, the second improved set is introduced. For both optical designs the system simulations are done and the system is improved.

In Chapter 4 the developed system is tested with the home made software after system is verified for its lateral and the vertical resolution, experiments are done on different engineering surfaces.

5.2 Future work

In this thesis only a few of the many possible sample types that are suitable for inspection with an optical microscope have been examined. For characterizing the performance of the micromirror based confocal microscope it is necessary to improve the range of test objects. Also for further investigations, in addition to engineering applications, the imaging of biological samples, fluorescence confocal microscopy, should be examined. For both developments it is necessary to improve the signal to noise ratio of the system.

Although mechanical design of the developed system is not critical it is still necessary to design and simulate the proper mechanical design for developed system. Early system model is derived and it is shown that the developed system is capable to achieve 10 nm vertical resolution.

Finally, it has been exciting to be involved in confocal microscopy together with the MEMS technology at this particular time. The cooperation between the

technologies will further improve the capabilities of future systems, such smart multi purposes microscope and maskless lithography applications.

REFERENCES

[1] **Taniguchi, N.**, 1974. On the Basic Concept of Nanotechnology, *Proceedings of the ICPE, Tokyo.*

[2] **Schwenke, H.**, 2002. Optical Methods for Dimensional Metrology in Production Engineering, *CIRP ANNALS, Manufacturing Technology*, **51**.

[3] **Velzel, C.**, 1997. Basis for Comparing the Performance of Surface Measuring Machines, *MB*, **1**.

[4] **Corle, T.R.**, 1996. Confocal scaning optical microscopy and related imaging systems, Academic Press, San Diego, USA, first edition edition.

[5] **Prime, F.P.W.S.o.M. and Manufacturing.**, 2002. An Introduction to MEMS (Micro-electro Mechanical Systems),Engineering, Loughborough University, PTECH.

[6] **Bhoyroo, E.**, 2003, Introduction to Microsystem Technology, *http://www.mma.org.uk.*

[7] **Kovacs, G.**, 1998. Micromachined Transducers Sourcebook, McGraw-Hill, New York, USA.

[8] **Madou, M.**, 1997. Fundamentals of Microfabrication, CRC Press, Boca Rotan, FL, USA.

[9] **Yoder, J.**, 1997. The Display Technology of the Future, *INFOCOMM.*

[10] **Taniguchi, N.**, 1983. Current Status in, and Future Trends, of Ultra Precision Machining and Ultra Fine Material Processing, *Proceedings of the ICPE, Tokyo.*

[11] **Taniguchi, N.**, 1996. NANOTECHNIOLOGY Integrated Processesing Systems for Ultra-Precisionn and Ultra-Fine Products, Oxford Science Publications, Oxford, UK.

[12] **Roukes, M.**, 2001. Nanoelectromechanical systems face the future, *PHYSICSWORLD*, **14/2**, 241–253.

[13] **ten Wolde, A.**, 1999. Nanotechnology, STT, The Hauge, 3th edition edition.

[14] **EUSPEN, H.L.E.G.**, 2002, The need for measurement and testing in nanotechnology, High Level Expert Group, *http://www.hyperion.ie/Nano.htm.*

[15] **Fleischer, D.A.**, 1988. Meeting the Challenge of Microelectronics, *RLE Currents, MIT publications*, **2/1**.

[16] **Whitehouse, D.J.**, 1994. Handbook of Surface Metrology, IOP Publishing Ltd., New York.

[17] **Stout, K.J.**, 2000. Three-Dimensional Surface Topography, Kogan Page Ltd., London.

[18] **Lonardo, P.M.**, 2002. Emerging Trends in Surface Metrology, *CIRP ANNALS, Manufacturing Technology*, **51**.

[19] **Thomas, T.R.**, 1999. Rough Surfaces, Imperial College Press, Londen, 2nd edition edition.

[20] **Evans, C.J. and Bryan, J.B.**, 1999. Structured, Textured or Engineered Surfaces, *CIRP ANNALS, Manufacturing Technology*, **48**.

[21] **Peklenik, J.**, 1967. Investigation of surface typology, *CIRP Annuals*, **15**, 381–385.

[22] **Stedman, M.**, 1987. Basis for Comparing the Performance of Surface Measuring Machines, *Precision Engineering*, **9**.

[23] **Blunt, L.**, 1994. A comprehensive study of 3D surface topography measuring instruments, *Proceedings of the 6th Nordic Symposium Tribology.*

[24] **Stout, K.J. and Sullivan, P.J.**, 1993. The Development of Methods for the Characterization of Roughness in Three Dimensions, Technical report, *Commission of the European Communities*, EUR 15178 EN, ISBN 0 7044 1313 2.

[25] **Stout, K.J. and Blunt, L.**, 1994. Applications of 3D topography bio-engineering, *Proceedings of the 6th International Conference on Metrology and Properties of Engineering Surfaces*, 11–12.

[26] **CPSMA, C.o.P.S.M. and Applications**, 1998. Harnessing Light: Optical Science and Engineering for the 21st Century, National Academy Press, Washington D.C.

[27] **Hofling, R. and Ahl, E.**, 2004. ALP: Universal DMD controller for metrology and testing, *Proc. SPIE.*

[28] **Whitehouse, D.J.**, 2002. Surfaces and their measurements, Hermens Penton Science, London.

[29] **Simmonds, W.H.**, 1995. Optical Non-Contact Techniques for Engineering Surface, European Communities.

[30] **Mathia, T.**, **Zahouani, H. and Rousseau, J.**, 1994. Functional significance of different techniques for surface morphology measurements, Technical report, *Workshop on Surface Characterization and Microhardness measurements, European Commision*, DG XII 200 rue de la Loi, B-1049 BE.

[31] **GFM**, 1999. Optical Measurement Coding Analysation *Product Catalog*, GF Messtechnik GmbH, Aken.

[32] **Kooijman, C. and Horyon, J.**, 1993. Lemons,R. A. and C. F. Quate, *Proc. SPIE conf. on Factory Automation*, **2026**, 136–140.

[33] **Huser, D.**, **Pfeifer, T.**, **Scharsich, P. and Trapet, E.**, 1994. A survey of the errors of optical coordinate measuring probes, Ultraprecision in manufacturing engineering, *Ultraprecision in Manufacturing Engineering*, 11–14.

[34] **Creath, K.**, 1988. Phase measurements interferometry technique, *Progress in Optics*, **26**, 349–393.

[35] **Beyer, H. and Riesenburg, H.**, 1988. Handbuch der Mikroskopie, VEB Verlag Technik, Berlin.

[36] **J. Jordan, R.B. and Valentin, J.**, 2001. Quality assurance of HARMS and MOEMS surface structures using confocal white light microscopy. In: Lithographic and micromachining techniques for optical component fabrication, *Proceedings of the SPIE (International Society for Optical Engineering) Conference*, San Diego, CA, July 29–30, 51–58.

[37] **Minsky, M.**, 1961. Microscopy Apparatus, *U.S. Patent 3.013.467*, dated, December 1961.

[38] **Wilson, T.**, 1990. Confocal Microscopy, Academic Press, first edition edition.

[39] **Wilson, T.**, 1998. Theory and practice of confocal scanning microscopy, Academic Press, London, first edition edition.

[40] **Pfeifer, T. and Dussler, G.**, 2000. Confocal laser scanning microscope for microsurface characterisation and micrometrology, *X. International Colloquium on Surfaces*.

[41] **Kagerer, B.**, **Brodmann, R. and Valentin, J.**, 2002. 3D confocal microscopy for surface analysis of micro-structured materials, *Germany*, **4773**, 52–62.

[42] **Velzel, C.**, 2003. Dipols and Superresolution, *SPIE Proceedings*, **5477**, 151–163.

[43] **Pohl, A.W.**, 1991. Advances in Optical and Electron Microscopy, Academic Press.

[44] **Thomas, T.R.**, 1982. Rough Surfaces, Longmans Ed., New York.

[45] **Mathia, T.**, **Zahouani, H.**, **Rousseau, J. and Bosse, J.C.L.**, 1995. Functional Significance of Different Techniques for Surface Morphology Measurements, *Int. J. Mach. Tools Manufact.*, **35/2**, 195–202.

[46] **Stedman, M.**, 1981. Metrological evaluation of grazing incidence mirrors. High Resolution Soft X-ray Optics, *Proceedings SPIE*, **2-8**, 316–322.

[47] **Stedman, M.**, 1987. The Metrology of X-ray Optical Components: Mapping the limits of measuring Instruments, *Rutherford Appleton Laboratory (RAL) Report, Workshop on Advanced Technology Reflectors for Space Instrumentation.*

[48] **Jordan, J.**, 1998. Highly accurate non-contact characterization of engineering surfaces using confocal microscopy, *Measurement Science Technology*, **9**, 1142–1151.

[49] **Brodmann, R. and Webber, M.**, 2004. Applications and limits of optical metrology by the confocal multi-pinhole-technique, *XI. International Colloqium on Surfaces*.

[50] **Dudley, D.**, **Duncan, W. and Slaughter, J.**, 2003. Emerging Digital Micromirror Device (DMD) Applications, *Proc. SPIE*, **4985**, 14 – 25.

[51] **Tiziani, H.**, 1994. Confocal microscopy and projected fringes for surface characterisation, Technical report, *Proceedings on Surface Characterisation and Microhardness Measurements*, BCR information European Commission Report EUR 15707 EN.

[52] **Tiftikci, K.A.**, 2001. MICROSCAN, Design and Development of a Fast Optical 3D-Scanner with Programmable Digital Micromirror Device (DMD), TU Eindhoven, Eindhoven, post master thesis edition.

[53] **Bitte, F.**, 2002. Ein spiegel matrix basiertes optisches 3D messsystem fur die mikrostruktureprufung, Ph.D. thesis, RWTH Aachen.

[54] **Velzel, C.**, 2000. *Personal contact*.

[55] **Young, J. and Roberts, F.**, 1951. A flying spot microscope, *Nature*, **167**, 231.

[56] **Minsky, M.**, 1961. Microscopy Apparatus, *U.S. Patent 3.013.467*, dated, December 1961.

[57] **Minsky, M.**, 1988. Memoir on Inventing the Confocal Scanning Microscope, *Scanning*, **22**, 128–138.

[58] **Davidovits, P.**, 1969. Scanning Laser Microscope, *Nature*, **223**, 831–843.

[59] **Wilson, T. and Sheppard, C.**, 1984. Theory and practice of confocal scanning optical microscopy, Academic Press, London, first edition edition.

[60] **Lemons, A.**, 1974. . Acoustic microscope-scanning version, *Applied Phys. Letters*, **24(2)**, 163–165.

[61] **Petran, M.M.**, **Hadravsky, M. and Edger, D.**, 1968. Tandem-scanning reflected light microscope, *Journal of Opt. Soc. America*, **58**, 661–664.

[62] **Xiao, G.**, 1990. Confocal optical imaging systems and their applications in microscopy and range sensing, Ph.D. thesis, Stanford University.

[63] **Corle, T.R.**, 1989. Studies in confocal scanning optical microscopy, Ph.D. thesis, Stanford University.

[64] **Wilson, T.**, 1980. Imaging Properties and Applications of Scanning Optical Microscope, *Applied Physics*, **22**, 119–128.

[65] **Corle, T.R.**, 1986. Depth response of confocal optical microscopes, *Optical Letters*, **11**, 770–772.

[66] **Born, M. and Wolf, E.**, 1999. Principles of optics, Cambridge University Press, The Edinburg Building, Cambridge, UK, 7th edition.

[67] **Hecht, E.**, 2002. Hecht optics, Addison Wesley Longman, fourth edition.

[68] **Bradbury, S.**, 1984. An introduction to the optical microscope, Oxford University press, Walton street, Oxford,, 1st edition.

[69] **Cox, I.J. and Sheppard, C.R.J.**, 1986. Information capacity and resolution in an optical system, *j.Opt. Soc. Amer.*, **3**, 1152–1158.

[70] **Inoue, S. and Spring, K.**, 1997. Video Microscopy, Springer, New York, 2nd edition.

[71] **Xiao, G.G. and Kino, G.S.**, 1987. A real-time confocal scanning microscope, *SPIE Proc.Scanning Imaging Technology*, **609**, 107–113.

[72] **Webb, R.H.**, 1996. Confocal optical microscopy, *Repts. Prog.Phys.*, **59**, 427–471.

[73] **Jordan, J.H.**, 1996. Optische Mikrotopometrie und Raugheitmessung an technische Oberflachen, Ph.D. thesis, Institut fur Technise Optik der Universitat Stuttgart.

[74] **Hornbeck, L.J.**, 1997. Digital Light Processing™for High-Brightness, High-Resolution Applications, *Proceedings on Electronic Imaging, Projection Displays III, Co-Sponsored by IS&T and SPIE.*

[75] **Cha, S.**, **Lin, P.C.**, **Zin, L. and Fainman, Y.**, 1999. 3D profilometry using a dynamically configurable confocal microscope, *Proc. SPIE*, **3640**, 246 – 253.

[76] **Florence, J. and Yoder, L.**, 1995. Display System Architectures for Digital Micromirror Device (DMD) Based Projectors, *Proc. SPIE*, **2650**, 193 – 208.

[77] **Gove, R.J.**, 1994. DMD Display Systems: The Impact of an All-Digital Display, *Society for Information Display International Symposium.*

[78] **Dunn, C. and Hofling, R.**, 2007. Properties of the DMD digital micromirror device for new emerging applications in optical engineering, *Invited Paper, Proc. SPIE on Optical Measurement Systems for Industrial Inspection V*, **6616**.

[79] **Tiftikci, K.A. and Bitte, F.**, 2001, Microscan,EU Craft Project, SMT4-CT98-5525, Final Report.

[80] **Hecht, E.**, 1998. Hecht optics, Addison Wesley, third edition edition.

[81] **Broome, B.G.**, 1992. Microscope objectives and their evolution to optical disk objectives in lens design, *SPIE Optical Engineering*, **41**, 325–348.

[82] **Chang, C. and Shieh, H.**, 2000. Design of illumination and projection optics for projectors with single digital micromirror devices, *Applied Optics*, **39**, 3202–3208.

CURRICULUM VITAE

Karun Alper Tiftikci was born in Ankara in 1968, in 1990 he received his bachelor degree in mechanical engineering from Istanbul Technical University and in 1994 he received his Msc. degree in Robotics from the same university. At the same periods between 1990 - 1998 he worked at National Research Center - National Metrology Institute (UME) in Dimensional Measurement Laboratory as a researcher and as a head of laboratory. Between 1998 -2004 he worked at Eindhoven Technical University as research assistant and he received his post master degree in Mechatronics in 2001. In 2004 he joined the Applied Laser Technology as a optical design expert and since 2005 he is working at ASML as a lead optical designer.